BIOFUNCTIONALIZATION AND SURFACE STUDIES OF SEMICONDUCTOR

MATERIALS FOR SENSING DEVICE FABRICATION

By Yan Cao

A dissertation submitted to the

Graduate School – Rutgers, Newark, The State University of New Jersey

in partial fulfillment of requirements

for the degree of

Doctor of Philosophy

Graduate Program in Chemistry

Written under the direction of

Professor Elena Galoppini

and approved by

_____

_____

_____

_____

Newark, New Jersey
December 2014

Abstract of the Dissertation

Biofunctionalization and Surface Studies of Semiconductor Materials for

Sensing Device Fabrication

By Yan Cao

Dissertation Advisor:

Professor Elena Galoppini

This thesis describes the development and study of innovative approaches for stepwise functionalization of semiconductor surfaces. The methods developed in this thesis were applied to improve the selectivity and sensitivity of sensor devices. The research projects involved in this thesis encompass material synthesis, biochemical functionalization, interfacial analysis, and nano-device development. Inorganic semiconductor-based sensor devices, including ZnO and MgZnO nanostructured surfaces, and organic semiconductor (rubrene single crystals) were involved in these studies.

1) For inorganic nanomaterial-based sensor devices, we studied the effect of the surface morphology on the capabilities of the nano-sensors. The surfaces studied were

inorganic ZnO nano-structured semiconductors of three morphologies: nanorod, rough, and planar. These morphology effect studies were carried out by functionalization of ZnO surfaces with a linker possessing a terminal alkylthiol for coupling to single-stranded DNA. The resulting ssDNA-functionalized films were then hybridized with complementary ssDNA tagged with fluorescein. In a selectivity control experiment, no hybridization occurred upon treatment with non-complementary DNA. The ZnO films' surface functionalization, characterized by FT-IR-ATR and fluorescence spectroscopy and detected on the nano-QCM, was successful on nanorod and rough surfaces but was barely detectable on the planar surface.

The copper-free click reaction was successfully explored as a surface functionalization methodology for ZnO and MgZnO nanorod films. 11-Azidodecanoic acid was bound to ZnO and MgZnO nanorod films through the carboxylic acid moiety, leaving an azide group available for Cu-free click reaction with alkynes. The azide-functionalized layer was used to immobilize various molecules, either a fluorescent probe, for example pyrene, or a small bioactive molecule, for example biotin or folic acid, capped with an alkyne. The immobilization of pyrene on the surface was probed by fluorescence spectroscopy, and immobilization of biotin was confirmed by binding with streptavidin-fluorescein isothiocyanate. The functionalization of ZnO and MgZnO films was monitored by FT-IR-ATR, steady-state fluorescence emission, fluorescence microscopy, and FESEM.

Additionally, in a side development of the step-wise functionalization of inorganic semiconductor surfaces, this thesis proposed a pyrene-cucurbit[8]uril host-guest system to control binding orientation on nanostructured ZrO_2 and TiO_2 semiconductor surfaces.

The fluorescence emission spectra were mainly used to study the binding orientation on surfaces. With encapsulation of pyrene-based chromphore into CB8 to form a guest@host complex, the sharp blue-shifted monomer peak was presented in emission spectra and it helped to suppress the formation of excimer.

2) For organic semiconductor material, rubrene single crystal surface was functionalized with a trichlorosilane or diazonium salt as an anchor group, leaving an azide functional group for further Click Chemistry to immobilize various molecules. The modification to the rubrene surface was monitored by conductivity changes and Hall measurements.

Acknowledgements

I would like to express my sincerest appreciation to my advisor, Dr. Elena Galoppini, for the gift of her time, assistance, and guidance. My appreciation also extends to everyone in our group, both past and present members: Dr. Olena Taratula, Dr. Yongyi Zhang, Dr. Alfred Lee, Dr. Marina Kaiser, Dr. Hao Tang, Keyur Chitre, Agnieszka Klimczak, Hao Fan, Yuan Chen and Xiuyuan Ma.

I would like to thank my committee members, Prof. Richard Mendelsohn, Prof. Huixin He of Rutgers University, Newark and Prof. Yicheng Lu of Rutgers University, New Brunswick for their effort and time in reading and correcting my thesis.

I wish to also thank the faculty members of the Department of Chemistry, Rutgers University for their guidance, excellent teaching and research advice, and also the staff of both the Department of Chemistry and Rutgers University, especially Judy Slocum and Monika Dabrowski, for their helpfulness.

Table of Contents

Lists of Figures

List of Schemes

xvii

Lists of Tables

Lists of Abbreviations

1:1	a host guest complex composed of one guest and one host
CB[8]	cucurbit[8]uril
CB[n]	cucurbit[n]uril
MOCVD	metal-organic chemical vapor deposition
QCM	quartz crystal microbalance
ZnO-N	zinc oxide nanorod films
ZnO-R	zinc oxide rough surface films
ZnO-P	zinc oxide planar surface films
DTT	dithiothreitol
DMSO	dimethyl sulfoxide
TBAF	tetrabutylammonium fluoride
TMS	trimethylsilyl
equiv.	equivalents
ESI-MS	electrospray ionization mass spectrometry
CuAAC	Copper-Catalyzed Azide-Alkyne Cycloaddition
Hz	Hertz
IR	infrared
J	coupling constant in Hz
K	complexation constant

m/z	mass-to-charge ratio
MALDI-TOF	Matrix Assisted Laser Desorption Ionization- Time Of Flight
MO_n	metal oxide nanoparticle
MS	mass spectroscopy
NMR	nuclear magnetic resonance
ppm	parts per million
UV-Vis	Ultraviolet–visible spectroscopy
δ	chemical shift in ppm
$\Delta\delta$	induced shift change in ppm
λ_{max}	wavelength of maximum absorbance
λ_{ex}	excitation wavelength
…….	The sentences and paragraphs were slightly modified from papers of which I am a co-author

Objectives

The design of the interface between molecules and semiconductor surfaces is fundamentally interesting and important for the development of biosensors. The overall goal of this thesis is to design and develop innovative surface functionalization methodologies for a new generation of biosensors with high sensitivity and selectivity through scientific understanding and control of the interfacial chemistry.

In particular, highly ordered ZnO and MgZnO nanostructures have attracted increasing attention due to their multifunctional properties and controllable morphology during growth processes. Furthermore, ZnO and MgZnO are bio-compatible, and are therefore ideal platforms for biosensing applications. There are several approaches to achieve the goal of development of ZnO and MgZnO nanostructured biosensors: (i) Improvement of the sensitivity of nanostructured biosensors through controlled morphologies of the semiconductor nanomaterials. (ii) Design and development of innovative step-wise functionalization methods to modify the sensing surfaces with specific functional groups for the enhancement of biosensor's selectivity. (iii) Study of the photophysical properties of the nanostructures and the molecular linkers by using probe chromophores to achieve controllable interface chemistry. (iv) Development and study of sensor devices.

Recently, organic semiconductors, rubrene single crystals, were found to have promising applications in sensors. These organic semiconductors have high performance and low cost. To optimize organic semiconductors as sensing materials and to develop new device concepts, effective ways to functionalize surfaces and to tune interfacial properties are needed. This thesis proposes to achieve this goal through development of

versatile, stepwise methodologies to functionalize the surfaces of rubrene single crystal surfaces via click chemistry and modular components (H-L-A groups).

After establishing the specific objectives of this thesis, the introduction of step-wise functionalization of semiconductor surfaces is presented in Chapter A. The studies of morphology effects on ZnO-based QCM biosensors to optimize DNA immobilization are discussed in Chapter B. Chapter C focuses on the development of the functionalization of ZnO and MgZnO nanorod films with copper-free click chemistry. A description of the experimental results is also presented on the biofunctionalization protocol for ZnO and MgZnO with biotin and folic acid. Chapter D proposes a host-guest system through use of pyrene-based chromophores as a guest and Cucurbit[8]uril as a host for controlling the orientation of surface binding on nanostructured inorganic semiconductor surfaces. Chapter E presents rubrene single crystals as novel organic semiconductor materials. A description of the characterization of modified rubrene single crystals and specific methods is discussed in Chapter E.

Chapter A

General Introduction

Step-wise Functionalization of Semiconductor Surfaces

The overall goal of this thesis is to design and develop innovative surface functionalization technologies for a new generation of biosensors with high sensitivity and selectivity and achieve a molecular level understanding and control of the interfacial chemistry.   In biosensor application, the choice of the strategy for immobilization biomolecules on sensing surfaces is extremely important. The most commonly used immobilization techniques are physical adsorption, covalent binding and specific binding, as illustrated in Scheme A 1.   Physical adsorption was successfully employed for immobilization of a wide range of biological elements directly onto sensor devices through a combination of Van der Waals and hydrophobic forces, hydrogen bonds, and ionic forces. Lu and co-workers have reported DNA immobilization on nanostructured ZnO biosensors through direct physical adsorption, as illustrated in Figure A 1.[1] The biotin-modified single-strand DNA was immobilized on the sensor surfaces through high affinity between biotin and avidin.   This direct physical adsorption is very simple; however, the employed forces can be weak and the biomolecules attached by this method may be released. Castner and co-workers have studied the absorption of globular IgG molecules.[2] The IgG molecules are Y-shaped molecules, which present three different possible orientations on the sensing surfaces and the orientation of F_{ab} regions has a great impact on its activity.
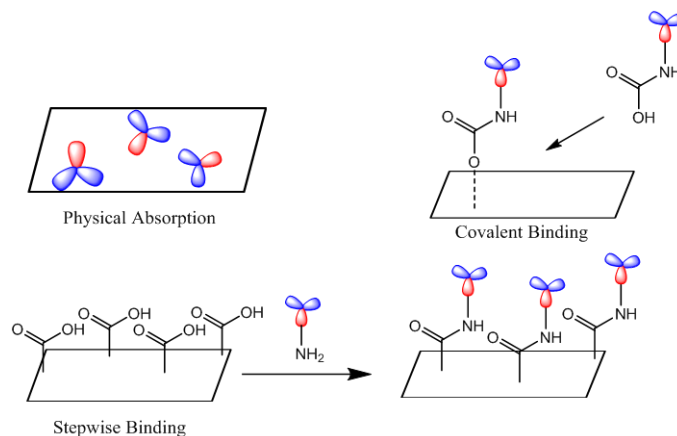
Scheme A 1 Three Strategies of Immobilization Biomolecules
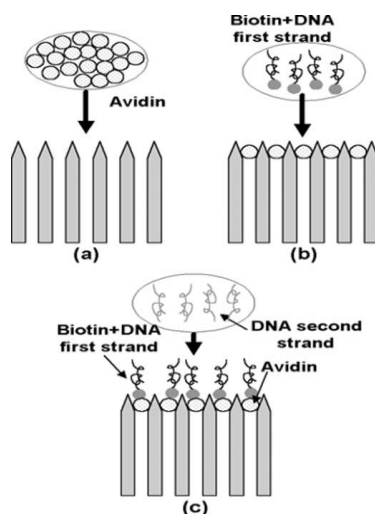
Figure A 1. Schematic representation of the DNA hybridization process (taken from reference 1).

Modification of biomolecules with a reactive group, for example, an amino acid group, has allowed binding to sensing surfaces. Compared with physical adsorption, the covalent binding method improves uniformity, density, and the strength of binding of the biomolecules. In addition, covalent binding may decrease instability, diffusion, and aggregation. However, covalent binding with large or bulky molecules can often result in

low surface coverage due to steric effects. In the case of step-wise functionalization, molecules carrying two different functional groups are bound. One functional group acts as an anchoring group to be attached to the sensing surface while leaving a second functional group available for further immobilization of molecules such as DNA and protein. Stepwise functionalization introduces a variety of functional groups for specific binding and usually forms structurally well-defined monolayers. In a recent example, Holmes and co-workers reported functionalization of Si surfaces with alkene, alkyne, and halide functional groups for studying palladium-catalyzed coupling reactions on surfaces (Figure A 2).[3] Szunerits and co-workers have reported step-wise functionalization of hydrogen terminated silicon with alkynyl-modified glycans through the click reaction (Figure A 3).[4] The resulting glycan modified surfaces could further detect proteins such as lectins. This method avoids introducing the steric effect of binding bulky biomolecules and improves the surface coverage.
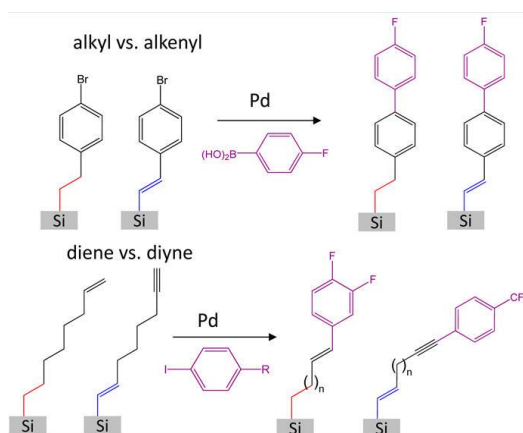
Figure A 2 Palladium-catalyzed coupling reactions for the functionalization of Si surfaces.(taken from reference 3)
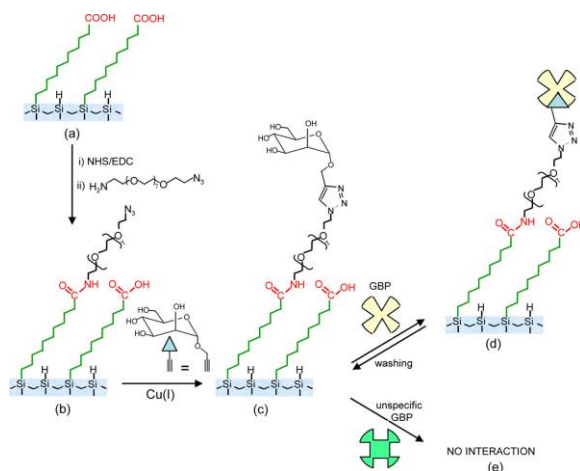
Figure A 3 Chemically modified silicon surfaces featuring decyl chains with terminal carboxy functions. (taken from reference 4)

Galoppini and coworkers previously developed well-controlled interfacial chemistry via a bifunctional linker for step-wise functionalization of ZnO nanostructured surfaces.[5] This functionalization strategy, illustrated in Scheme A 2, was useful for the immobilization of biomolecules. It involved the attachment of a bifunctional linker to the surface through one anchoring group and leaving a second reactive group available on the end to attach the biomolecule or chromophore. In this thesis, we extended this functionalization strategy from inorganic semiconductors, ZnO and MgZnO, to an organic semiconductor, rubrene single crystals. In the following section, more details about development of this functionalization on various surfaces will be discussed.
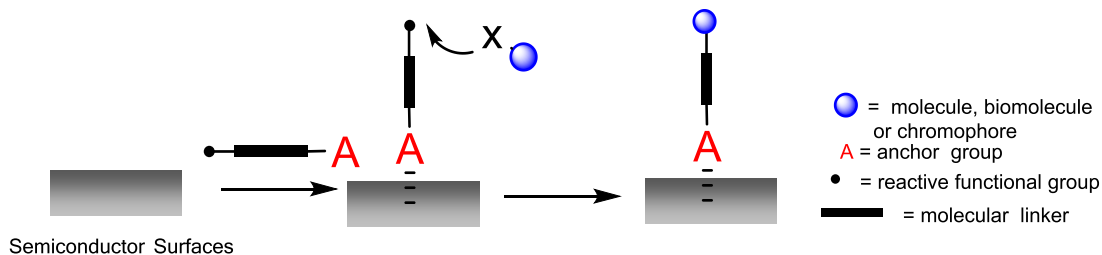
Scheme A 2 Functionalization strategy.

(i)   ***Anchoring Groups:***

Anchoring groups are needed to form the specific binding to the surface. A number of different anchoring groups, including carboxylic acid groups (COOH), phosphonic acid groups ($PO(OH)_2$) and silane groups ($SiCl_3$ and $SiOMe_3$), were previously demonstrated to be good anchoring group for functionalization of metal oxide surfaces.[6] Cheng and coworkers have developed surface functionalization of zinc oxide by carboxyalkylphosphoric acid self-assembled monolayers to immobilize IgG protein (Figure A 4 (I)).[7] Ronning and co-workers have reported on the biofunctionalization of zinc oxide for the attachment of DNA as target molecules by using trimethoxysilane as an anchor group (Figure A 4(II)).[8]

(I)   (II)

Figure A 4 Surface functionalization of zinc oxide by (I) carboxyalkyphosphoric acid as anchor group (taken from reference 7). (II) trimethoxysilane as anchor group (taken from reference 8).

We probed various anchor groups for functionalization of nanostructured ZnO surfaces: -COOH, -COOMe, $-P(O)(OH)_2$, $-SiOR_3$. We observed that the phosphonic acid group was not successful to bind to ZnO surfaces and the surfaces were visibly etched,

although the phosphonic acid group binds more strongly to metal oxide surfaces compared with carboxylic acid groups.[9] The phosphonic acid group is too acidic (pK_a approximately 2) and nanostructured ZnO surfaces are readily etched in acidic conditions, typically at pH < 4.[5] Silane groups including trichloro- or trimethoxy bonds are labile and more demanding from the synthetic point of view because of their extreme moisture sensitivity. Results obtained by our group suggest that COOH forms strong covalent bonds without etching the surfaces through control of binding time and concentration of binding solutions by forming carboxylate-type bonds. Three binding modes were investigated by Persson and coworkers, as listed in Figure A 5. The unidentate and bridging bonds are energetically most stable.[10]
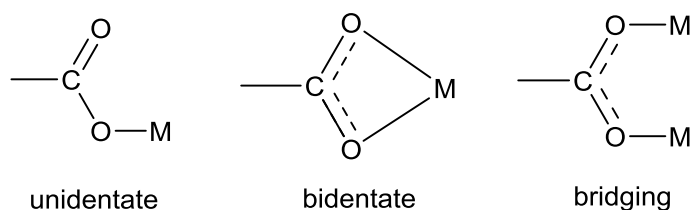
Figure A 5 Binding Modes of carboxylic acid group to ZnO

Anchor groups commonly used for metal oxide surfaces used as inorganic semiconductors do not functionalize organic semiconductors such as carbon nanotubes and graphene. Instead of carboxylic acid groups, phosphoric acid groups, and silane groups, as discussed above, aryl diazonium salts were specifically developed for functionalization of organic semiconductors.[11] Pinson and co-workers first described the reaction mechanism for the modification of carbon electrodes by aryl diazonium salts in 1992.[12] The interest in using aryl diazonium salts arises due to their ease of preparation, rapid reduction, large choice of reactive functional groups, and strong aryl-surface

covalent bonding.[13] The general chemical structure of aryl diazonium salts is shown in Scheme A 3, where R provides a general position for introducing halogens, amines, hydroxyls, or even azides into an aromatic ring to form a wide range of function, with A$^-$ as the counter anion.[14]
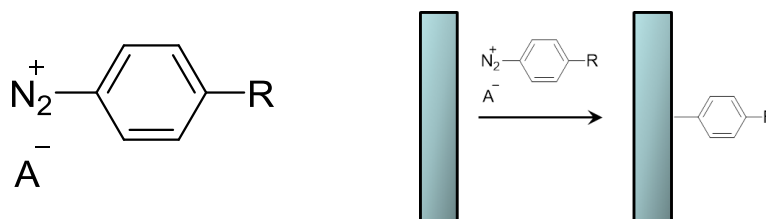
Scheme A 3 General chemical structure of aryl diazonium salts, A$^-$=BF$_3$, BF$_4$……

The application of aryl diazonium salts on carbon or graphene has been extensively studied. For example, diazonium salts have been studied in conjugation with protein chemistry: Gooding and co-workers have functionalized glassy carbon electrodes by reductive adsorption of the respective aryl diazonium salts for probing protein electrochemistry, as illustrated in Figure A 6.[15] This functionalization was employed to provide the ability to resist nonspecific adsorption of protein.
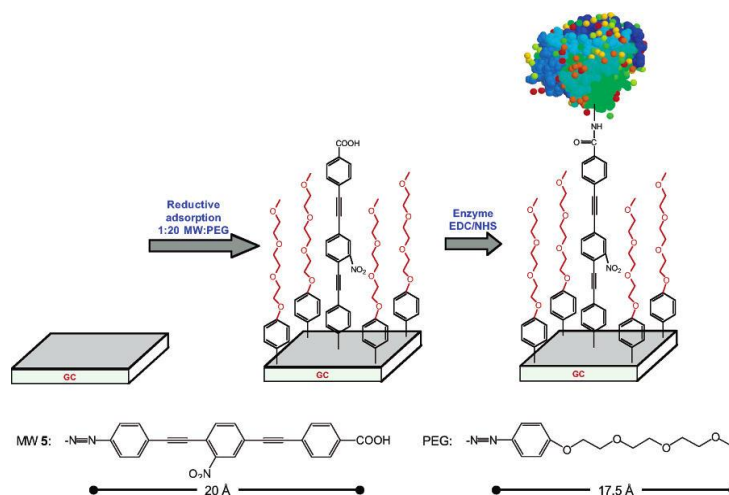
Figure A 6 Schematic of the glassy carbon interface for protein electrochemistry and the structure of aryl diazonium salts (taken from reference 15)

There are several synthetic challenges involved with the introduction of diazonium salts as anchor groups into desired targets. Diazonium halides are dangerously explosive and are immediately reacted without isolation once prepared. Diazonium salts with weakly coordinating anions, however, are quite stable. In fact, the tetrafluoroborates, such as commercially available 4-bromobenzene diazonium tetrafluoroborate and 4-nitrobenzene diazonium tetrafluoroborate can be stored almost indefinitely at room temperature and decompose gently when heated. For these reasons they are the reagent of choice for surface modification studied by several research groups.[16,17] Moreover, customized tetrafluoroborate diazonium salts have been synthesized with desired functional groups at low temperature. In particular, Limoges and co-workers synthesized azide modified diazonium salts to functionalize carbon electrodes through click chemistry.[18] As mentioned previously, organic semiconductors, including carbon electrodes, polymers, carbon nanotubes, and metal surfaces, are used for binding with diazonium salts.[19] Graphene drew our attention because it is an atomically thin, two-dimensional allotrope of carbon with exceptionally high carrier mobilities, thermal conductivity, and mechanical strength.[20] The application of diazonium salts to graphene is not unprecedented. Choi and his group reported using 4-bromobenzene diazonium tetrafluoroborate to functionalize graphene surfaces,[17] while Strano and co-workers synthesized 4-propargyloxybenzenediazonium tetrafluoroborate in order to study a subsequent attachment by click chemistry of short chain polyethylene glycol with a terminal carboxylic end group (PEG-COOH).[21]

Commonly, the diazonium salts bind experimentally under milder reactions, such as in aqueous solutions at room temperature. Tour and Strano's group studied the

mechanism of the diazonium salts' reaction with graphene surfaces. The proposed pathway follows a free radical mechanism, as illustrated in Figure A 7.[22] A spontaneous electron transfer from the surface of the graphane/graphene substrate to the diazonium salt generates an aryl radical on loss of N_2 and a graphane/graphene radical cation. A proton is eliminated from the graphane/graphene to form HBF_4 and a graphane/graphene radical. Within a common solvent shell, the free aryl radicals attack the surface near the sp^3 C-H bond sites to form the new covalent sp^3 C-C bonds.
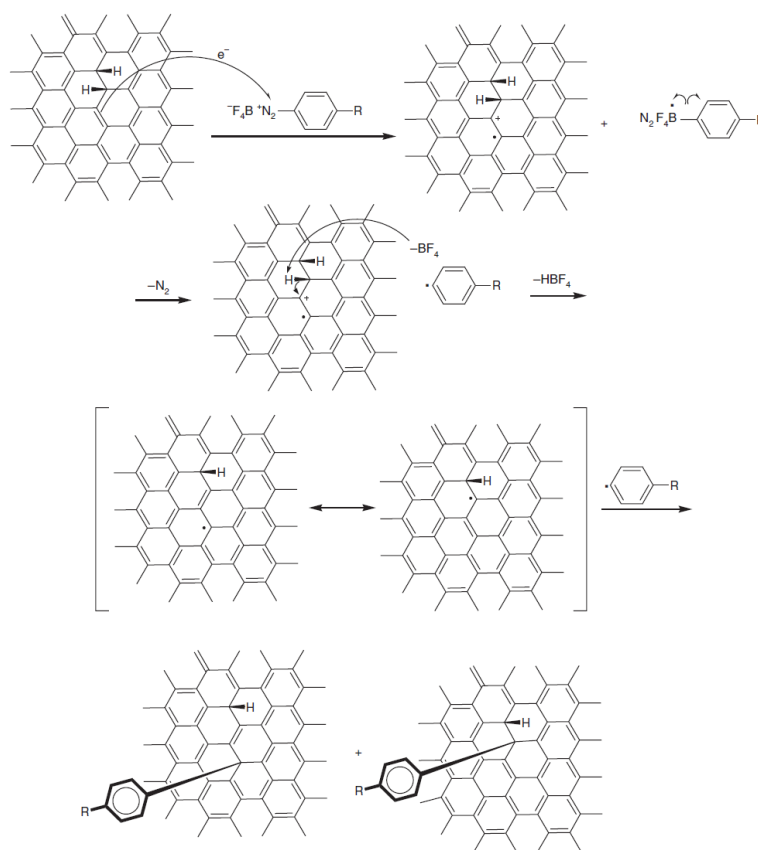
Figure A 7 Proposed mechanism for the diazonium reaction with hydrogenated graphene (taken from reference 22).

(ii) ***The Linker Units***

Long saturated aliphatic chains were selected to be the linker unit. This long chain likely packs closely to form an ordered layer. Moreover, it provides improved control over the distance of chromophore molecules on the surfaces, which can prevent quenching and allow fluorescence imaging.[23]

(iii) ***Reactive end group***

Previously in our group, we developed two routes to functionalize ZnO nanostructured films to immobilize DNA, as shown in Figure A 8. In route A, the surface functionalized with pyridyl disulfide as the end reactive functional group was reacted with a thiol-modified single strand DNA. In route B, the N-hydroxysuccinimide-ester end group was reacted with amino-modified DNA. In this thesis, we expanded the reactions at the interface beyond nucleophilic subsititutions. Click chemistry is the main focus in this thesis for functionalization of ZnO surfaces, as described in Chapter C.
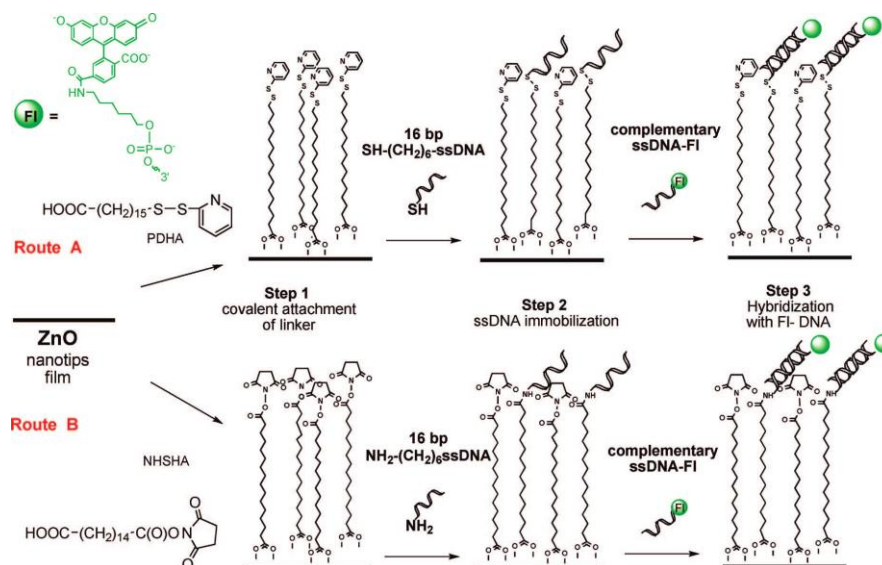
Figure A 8 ZnO nanotips surface modification Route A: thiol-disulfide exchange reaction and Route B: NHS-Ester hydrolysis (taken from reference 23)

In this thesis we will show that by the design and development of bifunctional linkers, as discussed above, we have applied a stepwise functionalization strategy using ZnO/MgZnO as inorganic semiconductor surfaces and rubrene single crystals as organic semiconductor surfaces.

References

(1)   Zheng, Z.; Emanetoglu, N. W.; Saraf, G.; Chen, Y.; Pan, W.; Jian, Z.; Yicheng, L.; Jingqiu, C.; Mirochnitchenko, O.; Inouye, M. *Ultrasonics, Ferroelectrics and Frequency Control, IEEE Transactions on* **2006**, *53*, 786.

(2)   Baugh, L.; Weidner, T.; Baio, J. E.; Nguyen, P.-C. T.; Gamble, L. J.; Stayton, P. S.; Castner, D. G. *Langmuir : the ACS journal of surfaces and colloids* **2010**, *26*, 16434.

(3)   Collins, G.; O'Dwyer, C.; Morris, M.; Holmes, J. D. *Langmuir : the ACS journal of surfaces and colloids* **2013**, *29*, 11950.

(4)   Gouget-Laemmel, A. C.; Yang, J.; Lodhi, M. A.; Siriwardena, A.; Aureau, D.; Boukherroub, R.; Chazalviel, J. N.; Ozanam, F.; Szunerits, S. *The Journal of Physical Chemistry C* **2013**, *117*, 368.

(5)   Taratula, O.; Galoppini, E.; Wang, D.; Chu, D.; Zhang, Z.; Chen, H.; Saraf, G.; Lu, Y. *The Journal of Physical Chemistry B* **2006**, *110*, 6506.

(6)   Galoppini, E. *Coordination Chemistry Reviews* **2004**, *248*, 1283.

(7)   Zhang, B.; Kong, T.; Xu, W.; Su, R.; Gao, Y.; Cheng, G. *Langmuir : the ACS journal of surfaces and colloids* **2010**, *26*, 4514.

(8)   Niepelt, R.; Schroder, U.; Sommerfeld, J.; Slowik, I.; Rudolph, B.; Moller, R.; Seise, B.; Csaki, A.; Fritzsche, W.; Ronning, C. *Nanoscale Research Letters* **2011**, *6*, 511.

(9)   Nilsing, M.; Lunell, S.; Persson, P.; Ojamäe, L. *Surface Science* **2005**, *582*, 49.

(10)   Persson, P.; Ojamäe, L. *Chemical Physics Letters* **2000**, *321*, 302.

(11)   Pinson, J.; Podvorica, F. *Chemical Society reviews* **2005**, *34*, 429.

(12)   Delamar, M.; Hitmi, R.; Pinson, J.; Saveant, J. M. *Journal of the American Chemical Society* **1992**, *114*, 5883.

(13)   Jiang, D.-e.; Sumpter, B. G.; Dai, S. *Journal of the American Chemical Society* **2006**, *128*, 6030.

(14)   Bahr, J. L.; Yang, J.; Kosynkin, D. V.; Bronikowski, M. J.; Smalley, R. E.; Tour, J. M. *Journal of the American Chemical Society* **2001**, *123*, 6536.

(15)   Liu; Gooding, J. J. *Langmuir : the ACS journal of surfaces and colloids* **2006**, *22*, 7421.

(16)   Wang, C.; Cao, Q.; Ozel, T.; Gaur, A.; Rogers, J. A.; Shim, M. *Journal of the American Chemical Society* **2005**, *127*, 11460.

(17)   Lim, H.; Lee, J. S.; Shin, H.-J.; Shin, H. S.; Choi, H. C. *Langmuir : the ACS journal of surfaces and colloids* **2010**, *26*, 12278.

(18)   Evrard, D.; Lambert, F.; Policar, C.; Balland, V.; Limoges, B. *Chemistry – A European Journal* **2008**, *14*, 9286.

(19)   Mahouche-Chergui, S.; Gam-Derouich, S.; Mangeney, C.; Chehimi, M. M. *Chemical Society reviews* **2011**, *40*, 4143.

(20)   Paulus, G. L. C.; Wang, Q. H.; Strano, M. S. *Accounts of Chemical Research* **2013**, *46*, 160.

(21)   Jin, Z.; McNicholas, T. P.; Shih, C.-J.; Wang, Q. H.; Paulus, G. L. C.; Hilmer, A. J.; Shimizu, S.; Strano, M. S. *Chemistry of Materials* **2011**, *23*, 3362.

(22)   Sun, Z.; Pint, C. L.; Marcano, D. C.; Zhang, C.; Yao, J.; Ruan, G.; Yan, Z.; Zhu, Y.; Hauge, R. H.; Tour, J. M. *Nature Communications* **2011**, *2*, 559.

(23)   Taratula, O.; Galoppini, E.; Mendelsohn, R.; Reyes, P. I.; Zhang, Z.; Duan, Z.; Zhong, J.; Lu, Y. *Langmuir : the ACS journal of surfaces and colloids* **2009**, *25*, 2107.

Chapter B

Biofunctionalization of Nanostructured ZnO and Morphology Effects

B.1 Background

B.1.1 Biosensors

What is a biosensor?

According to a recent IUPAC document,[2] a biosensor is defined as an analytical device, designed for the detection of an analyte, and comprising a biological recognition element and a physical-chemical transducer (Scheme B 1). The history of biosensors started in the year of 1962 with the development of enzyme electrodes by the scentist Leland C. Clark.[3] In 1977, Rechnitz and coworkers immobilized living microorganisms at the surface of an ammonia gas-sensing electrode.[4] Since then, research communities from various fields including Engineering, Physics, Chemistry, Material Science, and Biology have come together to develop more sophisticated, reliable, and pratical biosensing devices. Biosensors can have a variety of applications. The major application so far is clinical diagnosis, such as commercially available biosensors for glucose, cholesterol, or lactate.[5] Moreover, biosensor technology has tremendous potential in other fields of application, including food control such as food processing, safety, and quality control; environmental screening such as pollution monitoring; or chemical analysis. According to Transparency Market Research, the global biosensor market is expected to reach $18.9 billion in 2018. The growth in the scientific research field of biosensors also has been phenomenal. In 2012, there were about four and a half thousand peer-reviewed papers published pertaining to biosensors, representing more than 10% of all papers ever published on the subject.[6] Despite the large number of published papers,

the goals of this research in the field of biosensors focus on the design and development of sophisticated, high-throughput specialist machines or portable devices for use by non-specialists with high sensitivity and selectivity for rapid, accurate, and convenient measurement of complex biological interactions and components.
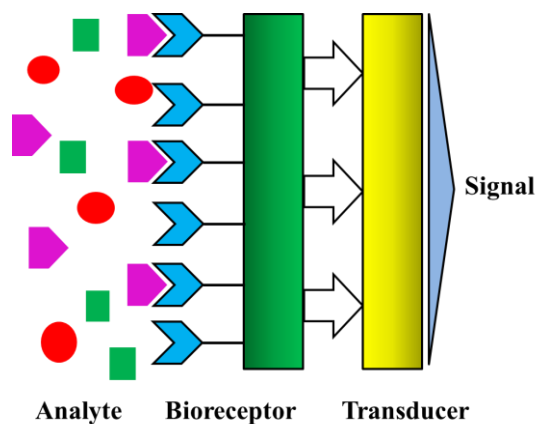
Scheme B 1 Basic components of a biosensor

As illustrated in Scheme B 1, the basic components of biosensors are bioreceptors as a bio-element and transducers as a sensor-element. The bioreceptor is designed to interact with the specific analyte to produce a measurable signal by the transducer. High selectivity for the analyte in the presence of a matrix of other chemical and biological components is a key requirement for the bioreceptor. The bioreceptor could be an enzyme, antibody, living cell, or nucleic acid. The transducer is an analytical tool to provide an output signal which has a given relationship to the input quantity.[7] Most common types of transducers used in biosensors are electrochemical, electrical, optical, piezoelectric, and thermal detection.[8] The bioreceptor and transducer can be coupled together in two main possible ways: physical adsorption and covalent bonding.

DNA Biosensors

As mentioned before, there is a variety of biological recognition elements used for the design of bioreceptors, including nucleic acids, antibodies, enzymes, etc. The focus of this thesis is the development of biosensors based on DNA as a bioreceptor. It can gain sensitivity and selectivity from the very strong base pair affinity between complementary sections of lined-up nucleotide strands.[9] The general DNA biosensor contains single-stranded DNA molecules with known sequences of bases, referred to here as a probe, which is synthesized and subsequently labeled with a fluorescent label. Then, the labeled probe will hybridize to its complementary sequence on the target molecules.[10] Many functional groups such as thiols, disulfides, amines, and biomolecules such as biotin are used to modify a DNA strand to allow immobilization to the transducer surfaces, resulting in highly ordered bioreceptor layers.[11] A long flexible spacer (hydrocarbon linkers) can be added to provide sufficient access to surfaces.[12] The electrochemical signals are easily measured by the transducer since the change of DNA structure resulting from the hybridization step causes the change of electrochemically detectable DNA properties. The DNA biosensors are especially suitable candidates for the rapid and inexpensive diagnosis of genetic diseases, and the detection of pathogenic biological species of clinical interest.[13] Much research has been done in DNA biosensors, both academic as well as industrial. Motorola Life Sciences Inc. has developed electrochemical detection by using eSensor DNA chips for detecting various diseases.[14] This device proceeded with a sandwich hybridization assay. Three critical components (capture probe, target and signaling probe) were present in the device, as illustrated in Scheme B 2. The capture probe was immobilized on the Au electrode and hybridized with the target DNA. The signaling probe was tagged with a ferrocene which

was served to label the target upon hybridization. Tamiya and co-workers have developed a localized surface plasmon resonance (LSPR) based DNA biosensor.[15] This device was based on a gold-capped nanoparticle layer substrate immobilized with DNA probe to recognize the target DNA related to tumor necrosis factor. The immobilization of target DNA was achieved through a multi-step functionalization, as illustrated in Scheme B 3.
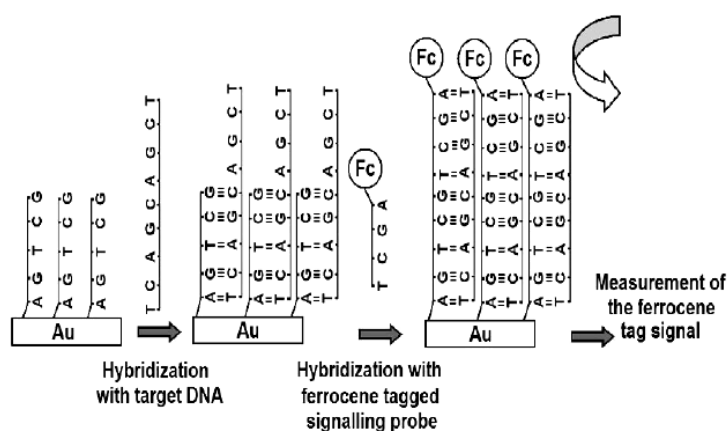
Scheme B 2 Electrochemical detection protocol of eSensor[TM] DNA chips. (taken from reference 14)
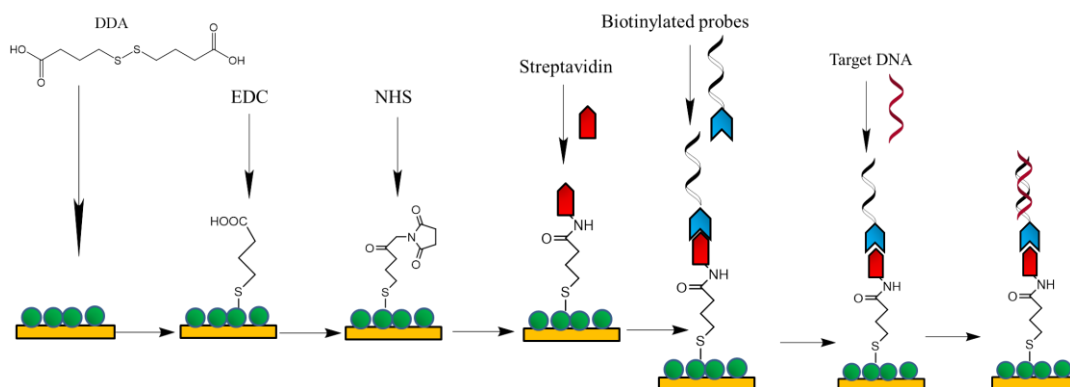
Scheme B 3 Immobilization of probe oligonucleotides on LSPR-based biosensors

B.1.2 ZnO and MgZnO Nanostructured Materials for Biosensing Applications

Zinc oxide (ZnO) is a wide bandgap ($E_g \sim 3.3eV$ at r.t.) semiconductor that has attracted tremendous interest in the past decade for advanced electronics, optical devices, and renewable energy applications.[16, 17, 18] In particular, nanostructured ZnO could provide a suitable platform for development of high performance sensors[19, 20, 21] or biosensors[22, 23, 24, 25, 26] as demonstrated by the exponential growth of publications in this area.[27] A unique advantage of ZnO, when compared to other wide band gap semiconductors, is that it forms highly anisotropic nanocrystals, such as nanorods for instance, because of the propensity for ZnO crystals to grow along the *c*-axis direction of the hexagonal wurtzite structure. However, the sensitivity to pH conditions is a crucial limitation for using nanostructured ZnO. ZnO is amphoteric and reacts with bases and acid to form zincate salts.[28, 29] For instance, pH conditions must be controlled (4<pH<9) to avoid etching of the ZnO nanostructured layers.[30] Yicheng Lu's group developed MOCVD methods to prepare $Mg_xZn_{1-x}O$ as alternative nanomaterial for biosensing applications due to its increased resistance to acids and bases when compared with ZnO.[31] Alloying ZnO with MgO forms the ternary compound $Mg_xZn_{1-x}O$, which allows tuning of the direct band gap of ZnO from ~3.3eV to ~4.0eV, as the composition of MgO is increased.[32] A wider band gap can make the nanomaterial useful for sensing in the UV region. This section reviews the material preparation technologies and materials properties which have an important relevance to biosensor functionality.

(i) Multifunctional and Biocompatible

ZnO and $Mg_xZn_{1-x}O$ are biocompatible, multifunctional materials that can be integrated with microelectronic components,[33] and are particularly attractive for development of transducers for miniaturized biosensors. Through proper doping and alloying, ZnO and $Mg_xZn_{1-x}O$ possess useful physical properties such as transparency and conductivity,[34] piezoelectricity,[35] or ferromagneticity,[36] allowing them to be used for various types of sensors. ZnO and its ternary alloy, $Mg_xZn_{1-x}O$ is considered to be nontoxic and biocompatible. They have been used in many applications in daily life, such as drug carriers and cosmetics. Zn and Mg are important elements for neurotransmitter production and enzyme function.[37]

(ii) Controllable and Reversible Surface Wettability

The surface wettability of ZnO nanomaterials can be controlled by switching between super-hydrophilic and super-hydrophobic states. In particular, making the sensing area superhydrophilic significantly decreases the analyzed liquid consumption while dramatically enhances the sensitivity of the biosensors.[1] Lu and other groups have demonstrated that the hydrophilic state is attained by exposing the surface under UV radiation; the hydrophobic state by oxygen annealing, as illustrated in Figure B 1.[1] Wettability is characterized by the contact angle (CA), which is the angle between the solid nanomaterial and liquid sample surfaces. If the liquid wets the solid surface, the value of the CA is $0^o < \theta < 90^o$. If the liquid does not wet the surface, the value of the CA is $90^o < \theta < 180^o$.[1]
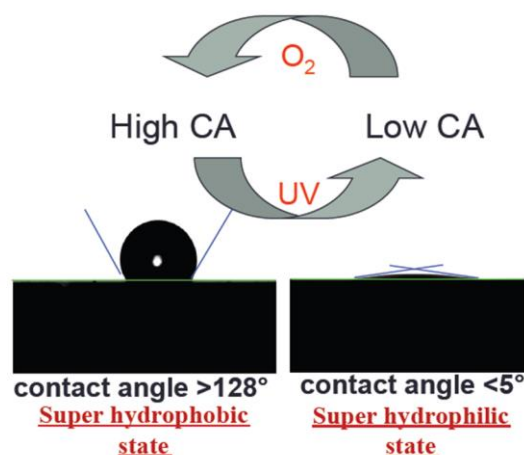
Figure B 1 Reversible surface hydrophobicity or hydrophilicity (taken from reference 1)

(iii)   *Flexible Growth Methods*

Numerous low-temperature growth methods with excellent morphology control are available. ZnO films can be grown or patterned in microarrays on a variety of substrates, including sapphire, ITO, silicon, gold, flexible polymeric materials, or directly onto sensors. Tipathi and co-workers have reported the synthesis of ZnO nanoparticles by the physical vapor condensation method[38] in addition to a hydrothermal method via dispersion in the solution.[39] Solanki and co-workers have reported nanostructured ZnO thin films fabricated on ITO by a sol-gel technique.[40] Lu's group employs metal-organic chemical vapor deposition (MOCVD) to grow high quality epitaxial ZnO and its nanostructures at relatively low temperatures.[41] In particular, these vertically aligned "nanotips" can be grown at 400 °C. The interface is atomically sharp, as evaluated by FESEM (Figure B 2a). The distribution of nanotips was found to be dense and uniform, as showed in FESEM (Figure B 2b).
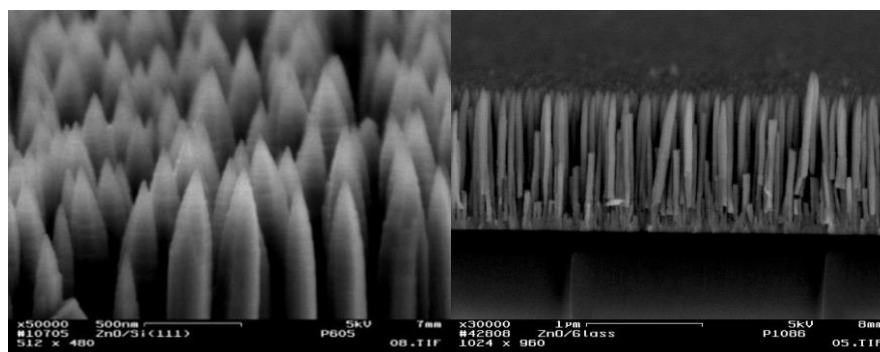
Figure B 2 FESEM image of (a) ZnO grown on Si substrate. (b) ZnO nanotips grown on glass substrate. (taken from reference 30)

(iv) *Functionalizability for Selective Detection:*

A key step towards the realization of biosensors having nanostructured ZnO as the sensing area is to tune the surface chemistry in order to achieve high sensitivity and selectivity.[31] The direct functionalization of nanostructured ZnO materials with biomolecules has been reported.[22] However, the direct functionalization does not allow sequential reactions on the surface and does not ensure a good control over the binding of the biomolecules. The step-wise functionalization could improve the surface coverage by avoiding the steric effect of bulky biomolecules, such as proteins, DNA or enzymes.[42] Non-covalent bond like physisorption could lead to the formation of a disordered layer of biomolecules.

B.1.3 ZnO$_{nano}$-QCM Biosensors

The type of sensor used in this study is the quartz crystal microbalance (QCM), a bulk acoustic wave device (Scheme B 4 (a)). A typical QCM device consists of a piezoelectric AT-cut quartz crystal sandwiched between a pair of metal electrodes. Quartz crystal as a piezoelectric material, when properly cut, has an oscillation at specific

frequency. This frequency is very sensitive to the mass of the crystal.[43] With an increase of the mass loading due to binding of molecules, the oscillation frequency of the crystal changes and this change is measured and used to determine the additional mass loading on the crystal.[44] Depending upon the thickness of the quartz layer, QCM devices can operate in the range of several MHz to tens of MHz.[45] There is a high interest in the biosensor applications of QCM devices due to its high mass sensitivity (sub-nanogram levels).[46] For instance, Zhang and co-workers have functionalized QCM biosensors based on gold nanoparticles with DNA probes for *bacillus anthracis* detection.[47] Zhou and co-workers have reported different methods for immobilization of DNA probes on QCM electrodes by chemical bonding or electrostatic adsorption.[48]

(a)

(b)
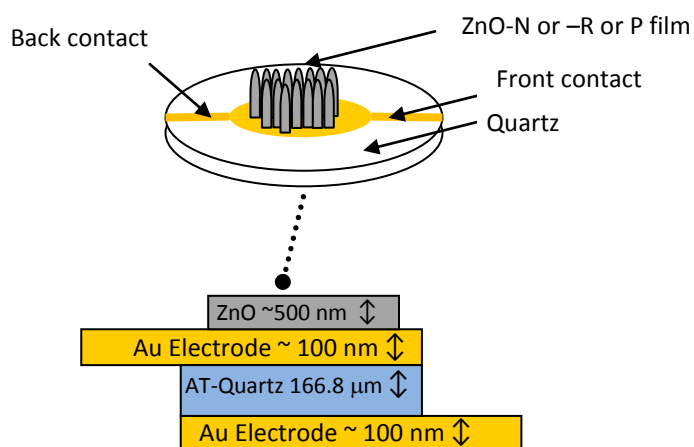
Scheme B 4 (a) Quartz Crystal Microbalance Device (b) Schematic of a ZnO-nanoQCM device, top view and cross section of the multilayer structure.

Lu and co-workers have reported a nano-QCM biosensor constructed by growing nanostructured ZnO directly on the sensing area of a conventional QCM, as illustrated in Scheme B 4 (b). Nanostructured ZnO QCM devices are simple in design and fabrication and work in both liquid and gas phase. ZnO-based sensors have exhibited high sensitivity to various chemicals including CH_4, CO, H_2O and biomolecules including DNA and proteins.[49,30] The mass loading on the QCM sensing area was determined directly from the shift in its resonant frequency and its mass sensitivity, S is given by the equation 1, where Δf is the resonant frequency shift due to mass loading, f_0 is the resonant frequency of the QCM, Δm is the mass loading, and A is the area of the quartz layer.[45]

$$S = (\Delta f/f_0)(A/\Delta m) \quad \text{eq (1)}$$

Sauerbrey's model is the most common model used to calculate the QCM's mass loading.[50] However, for measuring the frequency shift in the liquid phase, Sauerbrey's model is not accurate. A number of factors such as interfacial liquid properties, thin film viscoelasticity, and mechanisms of acoustic coupling impact on QCM oscillation behavior.[51] The viscous damping could cause large frequency shifts leading to instability of QCM.[44] Hence, Lu and co-workers have used the multilayer transmission line (MTL) model for simulation of QCM's mass loading in liquid phase.[45] This model was demonstrated in a ZnO nanostructure-based QCM device that selectively detects DNA immobilization and hybridization where the DNA mass loading was calculated.[45]

In this thesis, we focused on development of ZnO_{nano}-QCM biosensors with high sensitivity and selectivity by studying the morphology effect of ZnO nanostructured surfaces.

B.2 Results and Discussion*

*The three-step functionalization of ZnO is illustrated in Scheme B 5.[30] In Step A bifunctional linker 16-(2-pyridyldithiol)-hexadecanoic acid (PDHA) was bound to ZnO through the COOH group, leaving available for further functionalization a thiol group, protected as a 2-pyridyl disulfide, on the opposite end of the long saturated aliphatic chain. Step B involved a disulfide exchange with a thiol-substituted single stranded DNA (SH-ssDNA), which was obtained by *in situ* reduction of the commercially available ssDNA-S-S-ssDNA by treatment with DTT resin in in PBS buffer to form the free thiol. The resulting ZnO films, with ssDNA immobilized on the surface, were treated in Step C and Step D with complementary or non-complementary ssDNA (ssDNA-Fl and ssDNA'-F, respectively) which was tagged with fluorescein for imaging the films after the hybridization step. The entire sequence was conducted on ZnO Films grown on glass as well as grown on a nanostructured ZnO quartz crystal microbalances (nano-QCM).[45]

---

*IMPORTANT NOTE: The sentences and paragraphs within this section of the thesis were slightly modified from papers of which I am a co-author.
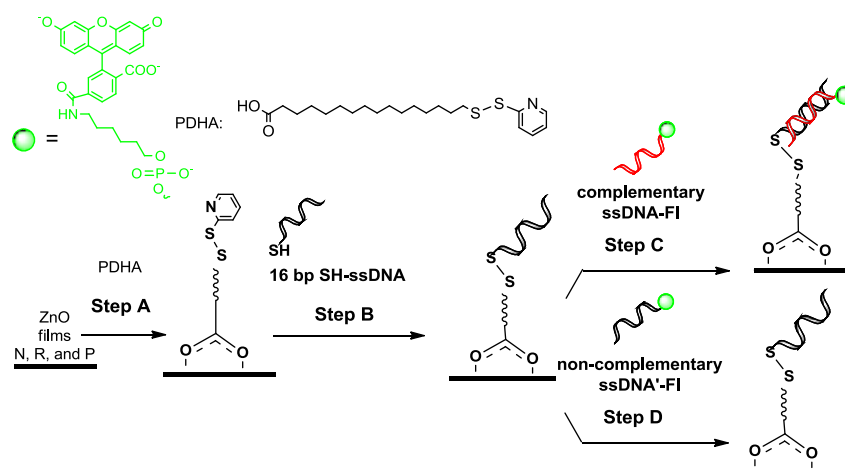
Scheme B 5 Functionalization sequence of ZnO Films-N, -R and -P.

In this work we address two open questions about this methodology: selectivity and sensitivity. First, we wanted to determine whether the functionalization method is applicable to other morphologies of ZnO and how the sensors properties change depending on the morphology of the ZnO layer. Three three different surface morphologies (i.e., nanorod layers (ZnO films-N), rough surface films (ZnO films-R), and planar surface films (ZnO films-P) were studied. As Field emission scanning electron microscope (FESEM) images shown in Figure B 3. Films-N consisted of columnar, perpendicularly aligned, ZnO nanorods about 0.5 μm long and 40 nm in diameter. Films-R exhibited a rough surface and Films-P had a mostly planar surface. In all cases, the films were about 0.5 μm thick. We anticipated that sensors prepared from nanorod films, the morphology with larger surface area, will result in higher sensitivity. Second, we wanted to probe whether the functionalization scheme, in this case the hybridization of immobilized DNA, is selective.
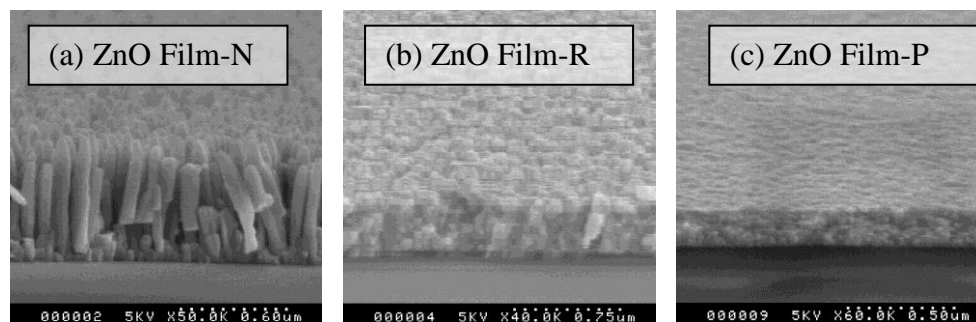
Figure B 3 FESEM images of 0.5 μm-thick MOCVD-grown ZnO films on glass with three different morphologies: (a) Films-N (Nanorods), scale bar: 0.6 μm. (b) Films-R (Rough), scale bar 0.75 μm. (c) Films-P (Planar), and scale bar 0.5 μm.

B.2.1 Droplet Binding Method

Each step of the functionalization process was performed on the ZnO Films-N, -R and –P in a sealed petri dish to avoid evaporation at room temperature. The commonly used method to bind molecules to metal oxide films involves immersion of the films in solutions. Here we used a method in which the solution with the reagent is deposited as droplets, henceforth the droplet method.[52] This method allowed depositing the binding solutions onto the ZnO sensor area without full immersion of the entire sensor. The films were stored for days in the dark without apparent change.

The droplet method is used to prepare a simple DNA combing method for biochemical analysis. The droplet method consisted in slowly adding the binding solution from the center of the ZnO nanorods films, drop by drop, to cover the whole surface of the film as illustrated in Figure B 4. The binding of the ZnO nanorods films was conducted at room temperature for the indicated time in a sealed petri dish to avoid solvent evaporation. The films were stable to be stored for days in desiccator and in the dark.
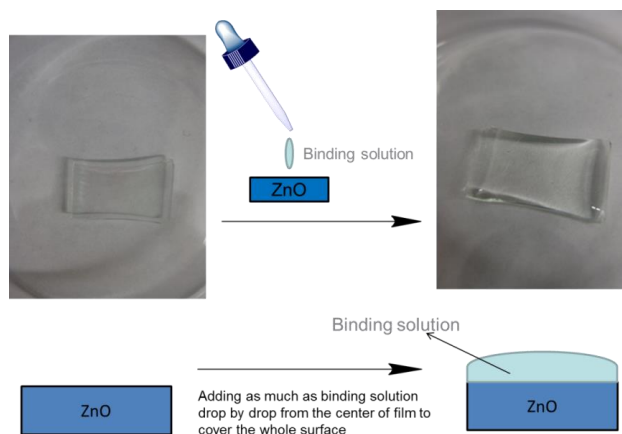
Figure B 4 Schematic illustration of the droplet method

Additionally, we observed that the droplet method results in enhanced binding on ZnO Films N and R (Figure B 5 and Figure B 6), compared to full immersion in a solution. Possible explanations of this result include a capillarity effect, reduced etching of the acid-sensitive ZnO nanorods surface, or possibly an effect of the nanostructure's surface tension, or a combination of these effects.
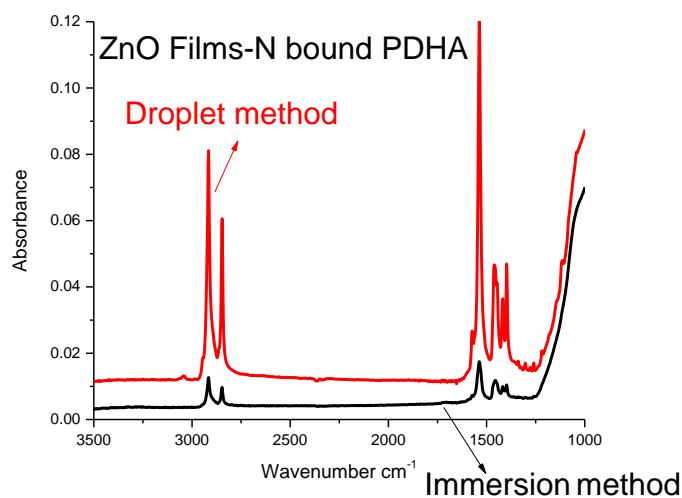
Figure B 5 FT-IR-ATR of ZnO Film-N after step A functionalized by droplet method with 2 mM PDHA solution in 1-butanol/ethanol 2/1 for 12-15h (top, red line) and immersion in a 2 mM PDHA solution in 1-butanol/ethanol 2/1 (bottom, black line) for 12-h
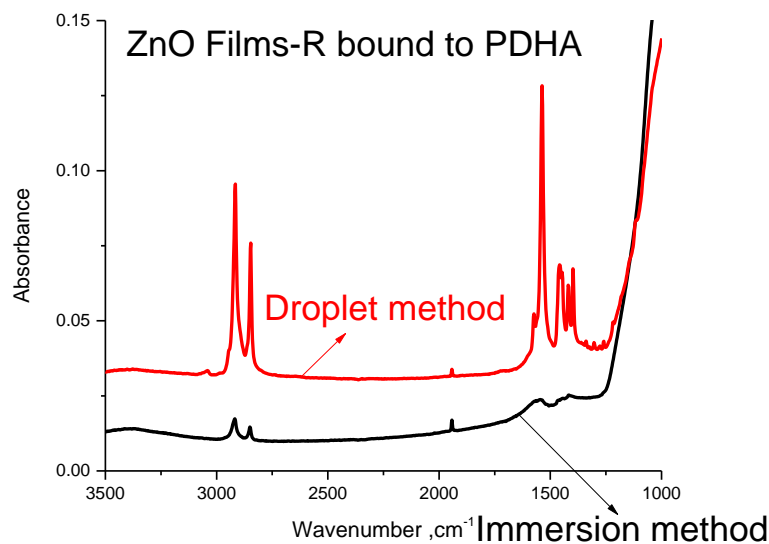
Figure B 6 FT-IR-ATR of ZnO Film-R spotted with 2 mM PDHA solution in 1-butanol/ethanol 2/1 for 12-15h (top, red line), immersed in a 2 mM PDHA solution in 1-butanol/ethanol 2/1 (bottom, black solid line) for 12-15 h.

B.2.2 Step-wise Functionalization

The functionalization sequence was monitored by FT-IR-ATR on ZnO Films-N, -R, and –P. The FT-IR-ATR showed similar results for three different morphologies. Hence, we showed FT-IR-ATR results collected from step-wise functionalization of ZnO Films-N as an example here. In step A, binding of the COOH group resulted in spectral changes in the carbonyl region, Figure B 7. The characteristic carbonyl asymmetric stretch (ν_{as}(C=O)) band of the free acid at 1706 cm^{-1}, which is present in the spectrum of neat PDHA, was replaced by bands assigned to the carboxylate asymmetric stretch, ν_{as}(O⋯C⋯O), at 1540 cm^{-1} and at 1400 cm^{-1}. The C-O stretch band at 1250 cm^{-1} disappeared upon binding and the C-H stretch bands of the long saturated alkyl chain were visible in the region below 3000 cm^{-1} in the bound films. Overall, the observed

spectral changes were indicative of PDHA binding on ZnO nanorod films through the COOH group and were consistent with our previous observations.[30]
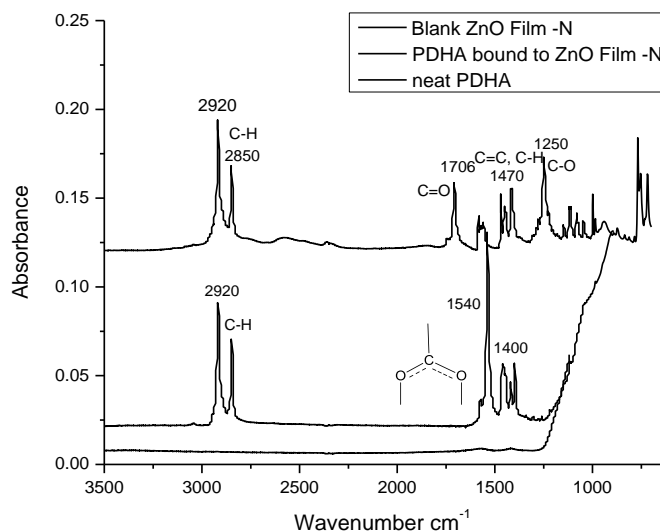
Figure B 7 FT-IR-ATR of blank ZnO Film-N (bottom line); PDHA bound to ZnO Film N after step A (middle line); neat PDHA powder (top line).

Step B and C are more difficult to monitor by FT-IR-ATR, because bands characteristic of the phosphate groups of DNA (~1100 cm^{-1})[53] are in part obscured by the bands of the ZnO substrate (Figure B 8). The broad bands in the 1100 cm^{-1} region appear intensified after the hybridization step with ssDNA-F1 (Step C), as shown in the FT-IR-ATR spectra in Figure B 8, using the 1540cm^{-1} band as an internal reference, and a shoulder appears in the 1600 cm^{-1} region. Other bands that can be assigned to DNA[53] were observed in the 1600 cm^{-1} region (arrow). Similar spectral changes were observed for all three morphologies, but very weak spectra were observed for the planar morphology films (ZnO Films-P), as illustrated by Figure B 9 and Figure B 10. The effect of strong background absorption observed from the ZnO substrate increased for ZnO Films-P compared with other morphologies (Figure B 11). The possible explanation

for this result could be related to better surface contact with substrates during FT-IR-ATR measurements.
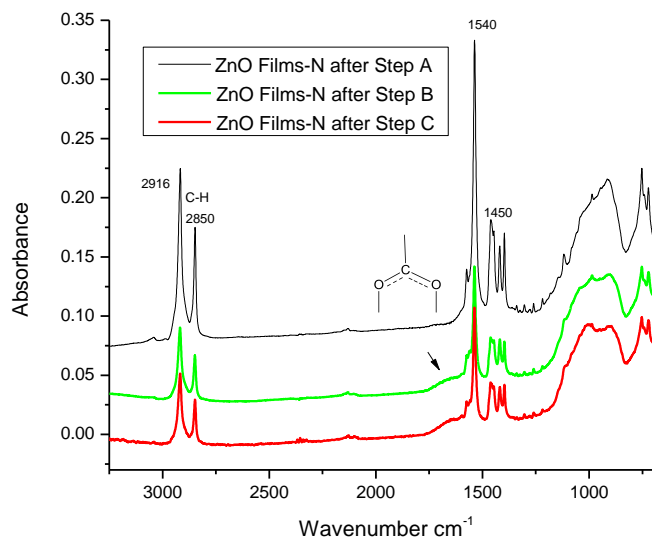
Figure B 8 FT-IR-ATR spectra of ZnO Film-N bound to PDHA (top, black line), following immobilization of SH-DNA (middle, green line), and following hybridization with complementary F1-ssDNA (bottom, red line).
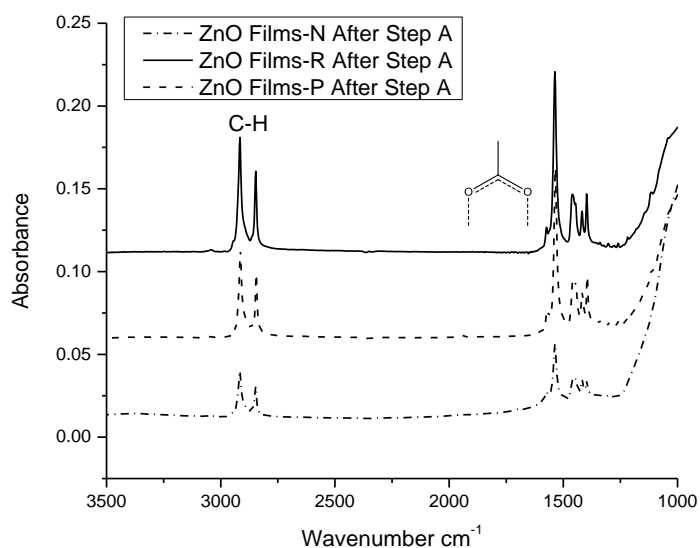
Figure B 9 FT-IR-ATR of ZnO Films after Step A: Film-N (top solid line), Film-R (middle dashed line), and Film-P (bottom dotted line).
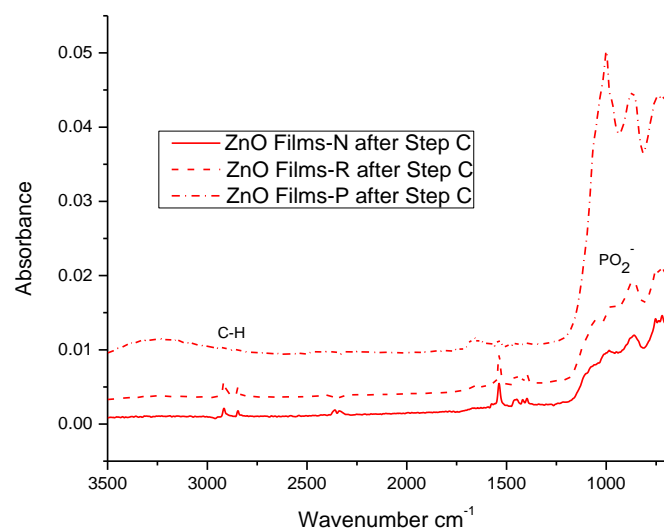
Figure B 10 FT-IR-ATR spectra of films after the hybridization step C: ZnO Film N (bottom, solid line); ZnO Film R(middle dashed line); ZnO Film P (top dotted line).
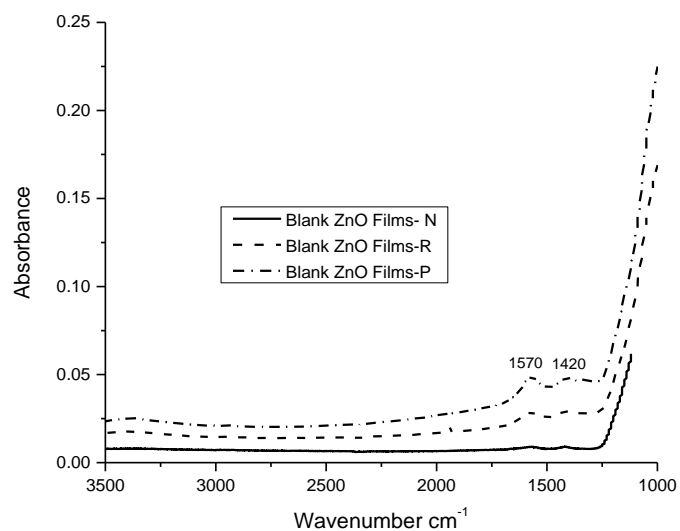
Figure B 11 FT-IR-ATR spectra of blank films: ZnO Film N (bottom solid line); ZnO Film R(middle dashed line); ZnO Film P (top dotted line).

In summary, the quality of FT-IR-ATR spectra was satisfactory only for films with higher surface area, and only to monitor the first step. The low surface area and, possibly,

the inability to obtain a good surface contact, do not allow the use of FT-IR-ATR as an effective method to monitor the DNA binding and hybridization steps.

All three types of ZnO films, after the hybridization step with ssDNA-Fl were studied by monitoring the fluorescence of the 56-FAM fluorescein (F1) tag (λ_{ex} = 495 nm) which exhibits an intense band centered at 520 nm, Figure B 12. A comparison between the free ssDNA-Fl in PBS buffer solution and the fluorescence spectrum of the immobilized and hybridized DNA-Fl on ZnO Films N and R, show the spectrum broadens upon binding, probably a result of the distribution of different arrangements of the adsorbed fluorophore and surface heterogeneity. The weak fluorescence in Films P may be indicative of low surface coverage, consistent with the previous results,[30] and/or the formation of a disordered layer where the Fl unit comes in proximity of ZnO and fluorescence is quenched.
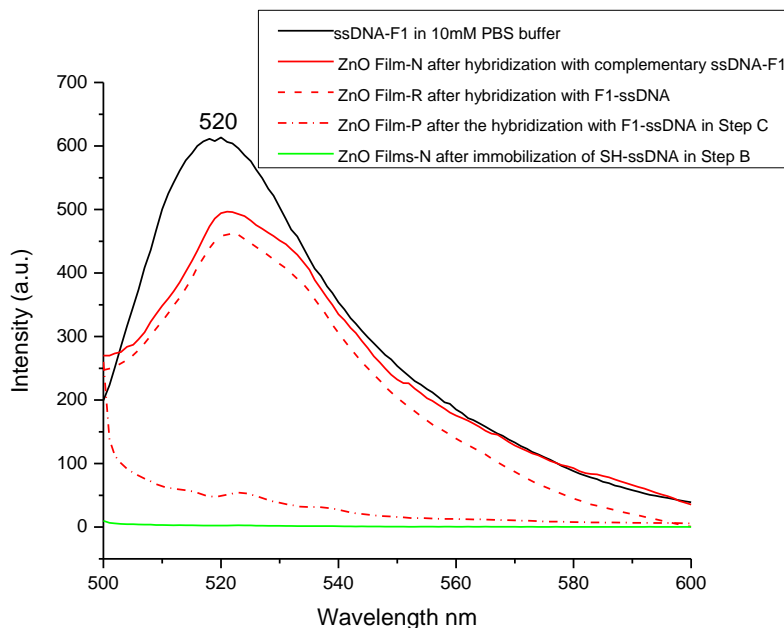
Figure B 12 Fluorescence spectra of ssDNA-Fl in 10 mM PBS buffer (black solid line); ZnO Films-N after hybridization with complementary ssDNA-Fl (red solid line); ZnO Films-R after hybridization with F1-ssDNA (red dash line); ZnO Films-P after the hybridization with Fl-ssDNA (red dotted line) in Step C; ZnO Films-N after immobilization of SH-ssDNA (green solid line) (λ_{ex}= 495 nm).

B.2.3 Selectivity of the Hybridization Process

To determine the selectivity of the method, we probed whether only complementary ssDNA would hybridize with the DNA functionalized ZnO layer. Non-complementary 5'-fluorescein-modified DNA (5'-/56-FAM/ATGCTTCGATGCAACG-3', ssDNA-Fl') was used in Step D, instead of complementary ssDNA-Fl. Step D with ssDNA-Fl' was monitored by fluorescence spectroscopy and fluorescence microscopy, Figure B 13. The ZnO N films did not fluoresce after treatment with non-complementary DNA (Figure B 13, middle line and inset), indicating that the hybridization step on the functionalized films is selective, and a necessary requirement for biosensor applications.
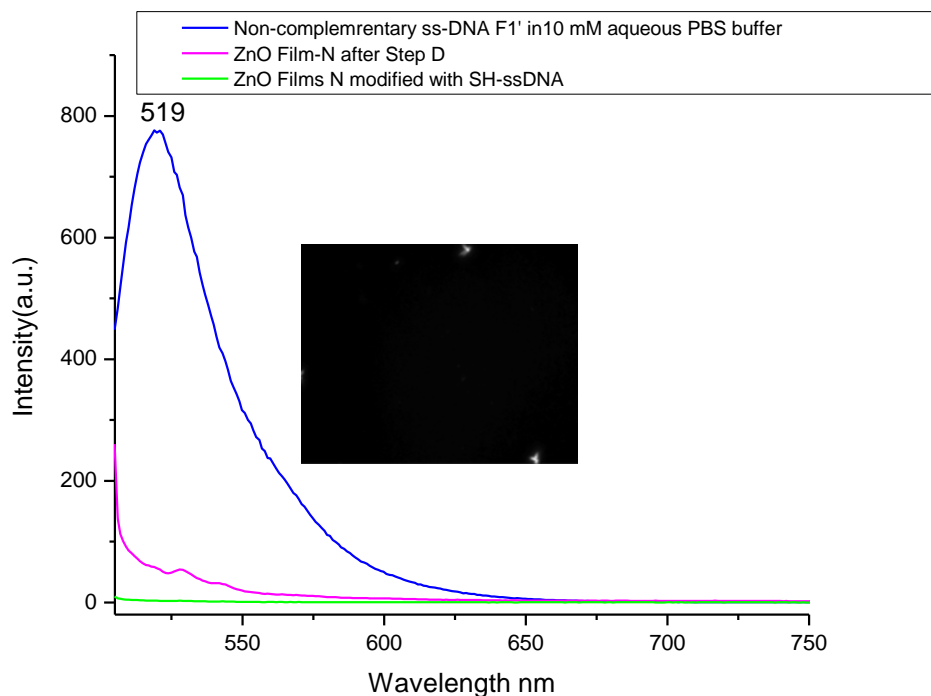
Figure B 13 Fluorescence spectra of non-complementary ssDNA-Fl' in 10 mM PBS buffer (top line); ZnO Films N modified with SH-ssDNA (bottom line); ZnO Films-N after Step D, the treatment with ssDNA'-Fl (middle line). ***Inset:*** Fluorescence microscopy image of the ZnO Films-N after reaction with ssDNA'-Fl, Step D.

B.2.4 Morphology effects on ZnO-based QCM Sensors

The result of this section would not have been possible without the extended work of our collaborators at Rutgers University-New Brunswick, especially Dr. Pavel Ivanoff Reyes and Dr. Yicheng Lu.

The same functionalization procedures were made on three ZnO-modified QCM sensors shown schematically in Scheme B 5. Three ZnO-modified QCM sensors were prepared with the ZnO Films-N, -R, and –P on the sensing area. The impedance spectra of the sensors were measured using a HP8753D Network Analyzer after every chemical step outlined in Scheme B 4. The frequency shifts of the impedance spectra due to mass loading on the ZnO-coated sensing area were recorded after Steps A, B and C for Films N, R and P, and the impedance spectra are reported in Figure B 14.

QCM with ZnO Film-R Sensing Surface

QCM with ZnO Film-P Sensing Surface
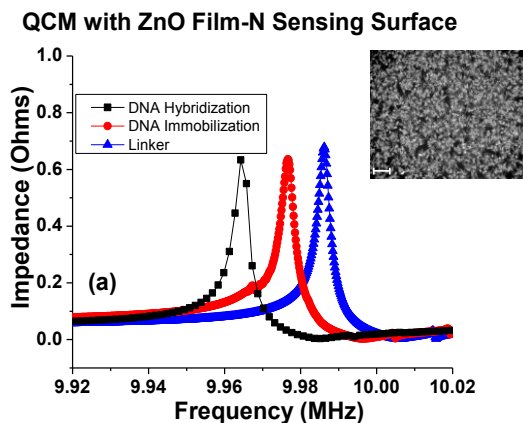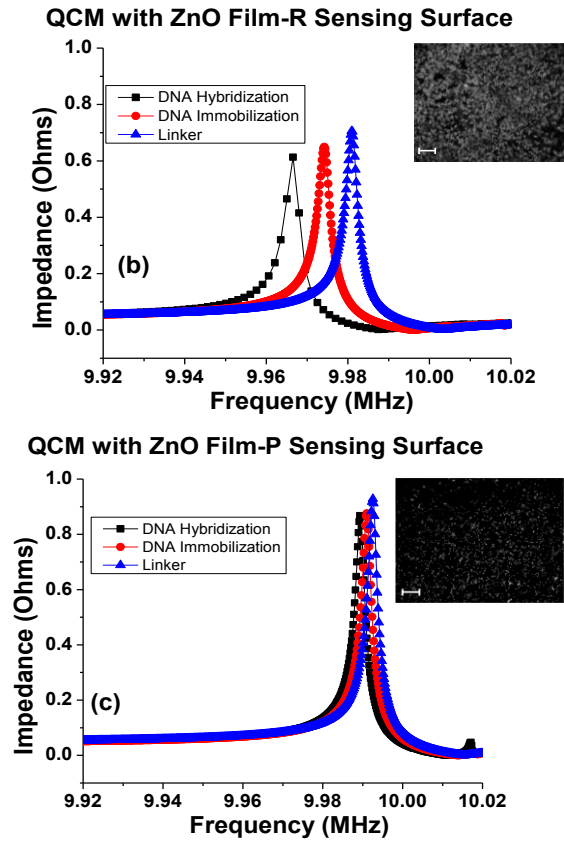
Figure B 14 Impedance spectrum ($Z(\omega)$) after Step A (black squares), Step B (red circles), Step C (blue triangles) on the ZnO-modified QCM with sensing area of *(a)* ZnO Film-N (top) *(b)* ZnO Film-R *(c)* ZnO Film-P. The inset for each plot is the fluorescence microscope image of the sensing area of the QCM device after Step C confirming binding on the ZnO nanostructures (Bar is 100 μm).

Table B 1 summarizes the frequency shifts for each chemical step for the ZnO-modified QCM sensors of different sensing area morphologies. The data indicate that the sensor with the ZnO Film-N yields the highest sensitivity as evidenced by the largest frequency shifts due to mass loading (> 10 times compared to ZnO Film-P surface). This 10-fold increase in frequency shift directly implies the increase in sensitivity of the QCM device as its sensitivity is directly proportional to frequency shift and is given by $S_f = k\Delta f/f_o$, where S_f is the sensitivity of the device, k is a constant proportional to the effective surface area available for sensing, Δf is the frequency shift, and f_o is the

operating frequency of the device. The enhanced sensitivity can be attributed to the larger effective surface sensing area provided by the ZnO Film-N morphology, compared to the other surfaces.*

Table B 1. Frequency Shifts and Mass Detection

	Δf (kHz) Step B	Δf (kHz) Step C	Δm (ng) Step B	Δm (ng) Step C
ZnO Film-P	1.523	1.675	20.17	22.19
ZnO Film-R	7.037	7.431	93.23	98.45
ZnO Film-N	13.49	11.06	178.8	146.5

B.3 Experimental Section*

General.

16-Mercapto-hexadecanoic acid, 2,2'-Dithiodipyridine, dithiothreitol (DTT) immobilized on polyacrylamide resin (Reductacryl from Calbiochem), ethanol 200 proof, and 1-butanol were used as received. Freshly prepared 10 mM aqueous phosphate saline buffer (PBS) pH = 7.4 from Sigma was used.[30] The 16 bases 5'-thiol-modifiedDNA 5'-/5 ThioMC6-D/GTGTTAGCCTCAAGTG-3' (SH-ssDNA), complementary 5'-dye (fluorescein)-modified DNA 5'-/56-FAM/CACTTGAGGCTAACAC-3' (FI-ssDNA) and non-complementary 5'-dye (fluorescein)-modified DNA 5'-/56-FAM/ATGCTTCGATGCAACG-3' were purchased from Integrated DNA Technologies. Membrane syringe filters, Anotop 10 Sterile 0.02 µm were purchased from Whatman, and PTFE 0.2 µm were purchased from Gelman. Single attenuated reflectance infrared (FTIR-ATR) spectra were performed on Thermo Electron Corporation Nicolet 6700 FT-

IR (ZnSe Crystal, number of spectra averaged 128, resolution 4 cm^{-1}). Fluorescence emission spectra on a VARIAN CARY-Eclipse. The films were placed diagonally at a 45° angle in a 1 cm cuvette in air while recording the fluorescence emission spectra. Reflection type fluorescence images were collected with an Axiovert 200 M confocal fluorescence microscope (Carl Zeiss, Gottingen, Germany) with a 510 nm filter and 480 nm excitation.

B.3.1 Synthesis

16-(2-Pyridyldithiol) hexadecanoic acid (PDHA).[54]   16-Mercapto-hexadecanoic acid (100 mg, 0.35 mmol) in ethanol (5 ml) was added dropwise to a solution of 2, 2'-dipyridyl disulfide (155 mg, 0.7 mmol) in ethanol (5 ml) and acetic acid (0.1 ml). The resulting yellow solution was stirred at room temperature overnight under nitrogen atmosphere, and then concentrated *in vacuo* to give yellow oil. The crude oil was purified by column chromatography (silica gel), eluting with hexane/ethyl acetate (4/1). The solvent was evaporated *in vacuo* to afford a cloudy liquid; then cooled in an ice bath to form white solid. Compound PDHA was obtained as a white solid. Yield: 100 mg (70%). ^{1}H (CDCl$_3$): δ8.51 (s, 1 H); 7.81 (d, 1 H); 7.72 (t, 1 H); 7.15 (s, 1 H); 2.81 (t, 2 H); 2.35 (t, 2 H); 1.66 (m, 4 H); 1.25-1.38 (m, 22H) ppm. ^{13}C (CDCl$_3$): 179.08, 160.30, 147.54, 138.82, 120.97, 120.75, 39.20, 33.97, 29.60, 29.54, 29.51, 29.49, 29.41, 29.38, 29.20, 29.11, 29.04, 28.95, 28.51, 28.44, 24.71ppm.

B.3.2 ZnO Preparation

The growth of ZnO Films and QCM sensors was conducted by our collaborators at Rutgers University-New Brunswick, especially Dr. Pavel Ivanoff Reyes and Dr. Yicheng Lu.

ZnO Films Growth. Metal organic chemical vapor deposition (MOCVD) growth methods were used for the growth of ZnO films from diethylzinc and oxygen, used as the metalorganic Zn source and oxidizer, respectively, on glass with three different morphologies using procedures described previously.[55] The morphology was controlled by varying the growth temperature: ZnO Films-P were grown at ~ 250 $^{\circ}$C, Films-R were grown at ~ 330 $^{\circ}$C, and the nanorods required a relatively high growth temperature (> 400 $^{\circ}$C). In the nano-QCM, the ZnO-covered sensing area was exposed to UV light to make it super-hydrophilic.[1]

ZnO-Modified QCM Sensor. We utilized a ZnO-modified quartz crystal microbalance (QCM) sensor to verify the morphology dependent chemical binding on ZnO. The sensor consists of a standard QCM with a piezoelectric AT-cut quartz layer which is sandwiched between two 100 nm gold electrodes. The quartz substrates have a diameter of 1.37 cm and the sensing area is 0.2047 cm^2. The sensing area (top electrode) of the QCM device consists of ZnO nanostructured arrays grown directly on the top electrode using metal organic chemical vapor deposition (MOCVD), Scheme B 4. We prepared three sensors corresponding to the similar ZnO morphologies.

B.3.3 Functionalization of ZnO Nanostructured Surfaces with DNA

The functionalization was Step A: linker binding, Step B: ssDNA immobilization, Step C: complementary ssDNA hybridization (fluorescent tagged), and Step D: noncomplementary ssDNA (fluorescent dye tagged).

Step A. The films were bound in 2 mM 16-(2-pyridyldithiol)hexadecanoic acid (PDHA) solution in 1-butanol/ethanol 2:1 for 12-15 h. The film was thoroughly rinsed with neat solvent and dried under gentle nitrogen flow.

Reduction of ssDNA-S-S-ssDNA. Commercially available ssDNA with a thiol in protected form was reduced by dithiothreitol ($[-CH(OH)CH_2SH]_2$, DTT) resin at room temperature to form the free SH group immediately prior to use. A ratio of 1 mg DNA per 50 mg DTT resin was used to ensure complete reduction. DTT resin (~ 17 mg) was added to 25 μM ssDNA-S-S-ssDNA in 10 mM phosphate buffer saline solution (PBS, pH = 7.4), which was filtered through a 0.2 μm polytetrafluoroethylene (PTFE) filter. The solution was stirred for 30 min at room temperature and then filtered through a 0.02 μm Anotop 10 Sterile filter to remove the DTT resin.

Step B. Freshly prepared 25 μM SH-ssDNA in PBS buffer was added on the ZnO films (droplet method) for 4h at room temperature. The films were rinsed with PBS buffer and dried under gentle nitrogen flow.

Step C and Step D. *Hybridization with ssDNA-Fl.* Complementary or non-complementary ssDNA-Fl (25 μM) in 10 mM PBS buffer was added (droplet method) on

the DNA-modified ZnO films for 1.5h at room temperature. The films were carefully rinsed with PBS buffer and dried under gentle nitrogen flow.*

B.4 Conclusion

Advanced applications of nanostructured ZnO sensors with enhanced sensitivity and selectivity require careful surface engineering. Here we probed the morphology effect of nanostructures ZnO films on a stepwise surface functionalization methodology that allows to selectively hybridizing DNA on the films. Three morphologies of ZnO nanorod film with comparable thickness (~500 nm) were studied: nanorods (Films-N), rough surface (Films-R), and planar films (Films-P). FT-IR-ATR spectra and fluorescence emission studies indicated that the ZnO nanorod films with larger surface area (i.e. R or N) are needed for the immobilization and detection of biomolecules. Additionally, a control experiment with non-complementary DNA tagged with fluorescein proved that the methodology is highly selective for the detection biomolecules, in this case ssDNA. The methodology was applied to ZnO-modified QCM sensors with ZnO nanorods (Films-N), rough surface (Films-R), and planar films (Films-P) on the sensing area. The measurements indicate that the sensor with the ZnO nanorods film provide the largest frequency shifts (> 10 time greater than the planar morphology) due to mass-loading.

In summary, we have demonstrated that the selectivity of nanostructured ZnO sensors is achieved through surface engineering, via chemical modification of the films, while sensitivity is achieved through the morphology control of nanostructured ZnO.

B.5 References

(1)   Zhang, Z.; Chen, H.; Zhong, J.; Saraf, G.; Lu, Y. *J Electron Mater* **2007**, *36*, 895.

(2)   Thévenot, D. R.; Toth, K.; Durst, R. A.; Wilson, G. S. *Biosensors and Bioelectronics* **2001**, *16*, 121.

(3)   Clark, L. C.; Lyons, C. *Annals of the New York Academy of Sciences* **1962**, *102*, 29.

(4)   Rechnitz, G. A.; Kobos, R. K.; Riechel, S. J.; Gebauer, C. R. *Analytica Chimica Acta* **1977**, *94*, 357.

(5)   D'Orazio, P. *Clinica Chimica Acta* **2003**, *334*, 41.

(6)   Turner, A. P. F. *Chemical Society reviews* **2013**, *42*, 3184.

(7)   McNaught AD, Wilkinson A (1997) IUPAC. Compendium of Chemical Terminology, 2nd ed. (the "Gold Book"). Blackwell Scientific Publications, Oxford.

(8)   Mohanty, S. P.; Kougianos, E. *Potentials, IEEE* **2006**, *25*, 35.

(9)   Borgmann, S.; Schulte, A.; Neugebauer, S.; Schuhmann, W. In *Advances in Electrochemical Science and Engineering*; Wiley-VCH Verlag GmbH & Co. KGaA: 2011, p 1.

(10)   Monošík, R.; Streďanský, M.; Šturdík, E. *Acta Chimica Slovaca* **2012**, *5*.

(11)   Stadtherr, K.; Wolf, H.; Lindner, P. *Analytical Chemistry* **2005**, *77*, 3437.

(12)   Labuda, J.; Brett, A. M. O.; Evtugyn, G.; Fojta, M.; Mascini, M.; Ozsoz, M.; Palchetti, I.; Paleček, E.; Wang, J. *Pure and Applied Chemistry* **2010**, *82*.

(13)   Wang, J. *Journal of Pharmaceutical and Biomedical Analysis* **1999**, *19*, 47.

(14)   Kerman, K.; Kobayashi, M.; Tamiya, E. *Measurement Science and Technology* **2004**, *15*, R1.

(15)   Endo, T.; Kerman, K.; Nagatani, N.; Takamura, Y.; Tamiya, E. *Analytical Chemistry* **2005**, *77*, 6976.

(16)   Morkoc, H.; Ozgur, U. Bandgap Engineering. Zinc Oxide: Fundamentals, Materials and Device Technology; Wiley-VCH: Wein-heim, Germany, 2009.

(17)   Lu, Y.; Zhong, J. Zinc Oxide-Based Nanostructures. In Semiconductor Nanostructures for Optoelectronic Application; Steiner, T., Ed.; Artech House: Boston, 2004; Chapter 6, pp 187-228.

(18)   Özgür, Ü.; Alivov, Y. I.; Liu, C.; Teke, A.; Reshchikov, M. A.; Doğan, S.; Avrutin, V.; Cho, S.-J.; Morkoç, H. *Journal of Applied Physics* **2005**, *98*.

(19)   Mai, L.; Kim, D.-H.; Yim, M.; Yoon, G. *Microwave and Optical Technology Letters* **2004**, *42*, 505.

(20)   Zheng, Z.; Hanhong, C.; Jian, Z.; Ying, C.; Yicheng, L. In *International Frequency Control Symposium and Exposition, 2006 IEEE* 2006, p 545.

(21)   Gabl, R.; Green, E.; Schreiter, M.; Feucht, H. D.; Zeininger, H.; Primig, R.; Pitzer, D.; Eckstein, G.; Wersing, W. In *Sensors, 2003. Proceedings of IEEE* 2003; Vol. 2, p 1184.

(22)   Dorfman, A.; Kumar, N.; Hahm, J.-i. *Langmuir : the ACS journal of surfaces and colloids* **2006**, *22*, 4890.

(23) Kumar, N.; Dorfman, A.; Hahm, J.-i. *Nanotechnology* **2006**, *17*, 2875.

(24) Zhao, J.; Wu, L.; Zhi, J. *Journal of Materials Chemistry* **2008**, *18*, 2459.

(25) Kumar, A.; Mortensen, N. P.; Mukherjee, P. P.; Retterer, S. T.; Doktycz, M. J. *Applied Physics Letters* **2011**, *98*, 253701.

(26) Usman Ali, S. M.; Alvi, N. H.; Ibupoto, Z.; Nur, O.; Willander, M.; Danielsson, B. *Sensors and Actuators B: Chemical* **2011**, *152*, 241.

(27) For instance, in 2007 there were 400 publications, compared to just a handful in 2002, devoted exclusively to 1D ZnO nanocrystals: Wang, Z. L. A New Nanomaterial Family for Nanotechnology. ACS Nano 2008, 2, 1987-1992. Splendid one-dimensional nanostructures of zinc oxide.

(28) Keis, K.; Bauer, C.; Boschloo, G.; Hagfeldt, A.; Westermark, K.; Rensmo, H.; Siegbahn, H. *Journal of Photochemistry and Photobiology A: Chemistry* **2002**, *148*, 57.

(29) Maki, H.; Ikoma, T.; Sakaguchi, I.; Ohashi, N.; Haneda, H.; Tanaka, J.; Ichinose, N. *Thin Solid Films* **2002**, *411*, 91.

(30) Taratula, O.; Galoppini, E.; Mendelsohn, R.; Reyes, P. I.; Zhang, Z.; Duan, Z.; Zhong, J.; Lu, Y. *Langmuir : the ACS journal of surfaces and colloids* **2009**, *25*, 2107.

(31) Taratula, O.; Galoppini, E.; Wang, D.; Chu, D.; Zhang, Z.; Chen, H.; Saraf, G.; Lu, Y. *The Journal of Physical Chemistry B* **2006**, *110*, 6506.

(32) Muthukumar, S.; Zhong, J.; Chen, Y.; Lu, Y.; Siegrist, T. *Applied Physics Letters* **2003**, *82*, 742.

(33) Calzolari, A.; Ruini, A.; Catellani, A. *Journal of the American Chemical Society* **2011**, *133*, 5893.

(34) Srikant, V.; Sergo, V.; Clarke, D. R. *Journal of the American Ceramic Society* **1995**, *78*, 1935.

(35) Onodera, A.; Tamaki, N.; Jin, K.; Yamashita, H. *Japanese Journal of Applied Physics* **1997**, *36*, 6008.

(36) Prellier, W.; Fouchet, A.; Mercey, B.; Simon, C.; Raveau, B. *Applied Physics Letters* **2003**, *82*, 3490.

(37) Miller, B. G.; Traut, T. W.; Wolfenden *Journal of the American Chemical Society* **1998**, *120*, 2666.

(38) Moballegh, A.; Shahverdi, H. R.; Aghababazadeh, R.; Mirhabibi, A. R. *Surface Science* **2007**, *601*, 2850.

(39) Li, Y.-F.; Liu, Z.-M.; Liu, Y.-L.; Yang, Y.-H.; Shen, G.-L.; Yu, R.-Q. *Analytical Biochemistry* **2006**, *349*, 33.

(40) Solanki, P. R.; Kaushik, A.; Ansari, A. A.; Malhotra, B. D. *Applied Physics Letters* **2009**, *94*.

(41) U.S. Patenent No. 6, 979, 489. " Zinc Oxide Nanotip and Fabricating Method Thereof." Y.Lu, S. Muthukumar, N. W. Emanetoglu, Dec. 27, 2005

(42) Gouget-Laemmel, A. C.; Yang, J.; Lodhi, M. A.; Siriwardena, A.; Aureau, D.; Boukherroub, R.; Chazalviel, J. N.; Ozanam, F.; Szunerits, S. *The Journal of Physical Chemistry C* **2012**, *117*, 368.

(43) Spetz, A. 2006, Chemical Sensor Technologies, Tutorial 2006

(44) Vo-Dinh, T.; Cullum, B. *Fresenius J Anal Chem* **2000**, *366*, 540.

(45)   Reyes, P. I.; Zheng, Z.; Hanhong, C.; Duan, Z.; Jian, Z.; Saraf, G.; Yicheng, L.; Taratula, O.; Galoppini, E.; Boustany, N. N. *Sensors Journal, IEEE* **2009**, *9*, 1302.

(46)   Ghindilis, A. L.; Atanasov, P.; Wilkins, M.; Wilkins, E. *Biosensors and Bioelectronics* **1998**, *13*, 113.

(47)   Hao, R.-Z.; Song, H.-B.; Zuo, G.-M.; Yang, R.-F.; Wei, H.-P.; Wang, D.-B.; Cui, Z.-Q.; Zhang, Z.; Cheng, Z.-X.; Zhang, X.-E. *Biosensors and Bioelectronics* **2011**, *26*, 3398.

(48)   Zhou, X. C.; Huang, L. Q.; Li, S. F. Y. *Biosensors and Bioelectronics* **2001**, *16*, 85.

(49)   Sadek, A. Z.; Wlodarski, W.; Li, Y. X.; Yu, W.; Li, X.; Yu, X.; Kalantar-zadeh, K. *Thin Solid Films* **2007**, *515*, 8705.

(50)   Sauerbrey, G. *Z. Physik* **1959**, *155*, 206.

(51)   Caruso, F.; Serizawa, T.; Furlong, D. N.; Okahata, Y. *Langmuir : the ACS journal of surfaces and colloids* **1995**, *11*, 1546.

(52)   Mao, Y.; Daniel, L. N.; Whittaker, N.; Saffiotti, U. *Environmental health perspectives* **1994**, *102 Suppl 10*, 165.

(53)   Stepanyugin, A. V.; Samijlenko, S. P.; Martynenko, O. I.; Hovorun, D. M. *Spectrochimica Acta Part A: Molecular and Biomolecular Spectroscopy* **2005**, *61*, 2267.

(54)   Tokutake, N.; Miyake, Y.; Regen, S. L. *Langmuir : the ACS journal of surfaces and colloids* **1999**, *16*, 81.

(55)   Muthukumar, S.; Gorla, C. R.; Emanetoglu, N. W.; Liang, S.; Lu, Y. *Journal of Crystal Growth* **2001**, *225*, 197.

Chapter C

Biofunctionalization of ZnO/MgZnO Nanotips Films by Click Chemistry

C.1 Background

C.1.1 Click Chemistry

As described in Chapter B.1.1, immobilization of biorecognition elements on sensor surfaces is a key requirement to develop biosensor devices with high selectivity and sensitivity. In order to ensure that all of the biomolecules are oriented in such a way that their binding sites are exposed to the sample solution, a uniform alignment onto the surface should be achieved. Step-wise functionalization methods as site-specific immobilization techniques have therefore been developed in the past few years. Such approaches usually require modification of the target molecules and sensing surfaces with functional groups that can react with the biorecognition element. In previous studies, we have developed step-wise surface functionalization involving displacement of a dithiane and a succinimide ester by thiol-DNA for ZnO biosensors.[1] Recently, we expanded the reactions at the interface beyond the nucleophilic substitutions to Click Chemistry which has been successfully used on a variety of surfaces including silicon, silica, gold[2, 3, 4] and more recently, on metal oxide nanoparticles.[5]

In his landmark review published in 2001, Sharpless and coworkers first used the term "Click Chemistry" as a "set of powerful, highly reliable, and selective reactions for the rapid synthesis of useful new compounds and combinatorial libraries".[6] Click Chemistry is not limited to a specific type of reaction, but the premier example of click reaction[7] is the azide-alkyne Huisgen cycloaddition of an azide and a terminal alkyne to form 1,2,3-triazole, first reported by Rolf Huisgen[8] and shown in Scheme C 1. The Click Chemistry should meet the following criteria to provide a useful strategy for uniform,

high-density surface immobilization of molecules in a covalent selective fashion: (i) quantitative conversion under mild conditions (insensitive to solvent and room temperature), (ii) no reaction byproducts (which might accumulate at the interface and retard or stop the surface reaction), (iii) compatibility with different functional groups (azide and terminal alkynes are exceptionally stable and can be introduced in a wide range of macromolecules), (iv) triazole formation is irreversible.[9]
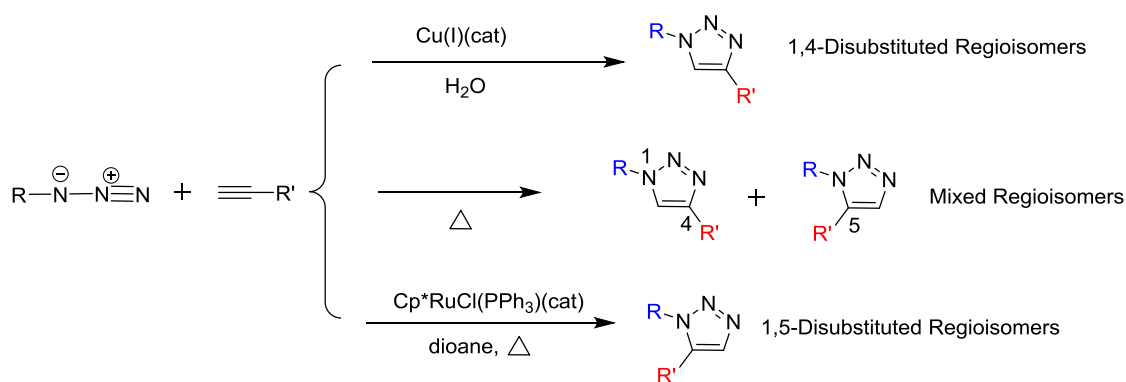
Scheme C 1 Methods of 1,2,3-triazole synthesis by click chemistry

Among the azide-alkyne cycloaddition reactions, the Copper-Catalyzed Azide-Alkyne Cycloaddition (CuAAC) is one of the most widely employed click reactions to date (Scheme C 1). This reaction is regioselective, forming only 1,4-substituted products. Fokin and Sharpless have studied the exclusive regioselectivity of the copper-catalyzed process and proposed the reaction mechanism as illustrated in Scheme C 2.[10] This proposed mechanism[10] begins with the coordination of the alkyne **1** to the copper species, followed with the conversion of the alkyne to the acetylide **2**. Then the azide replaces one of the ligands and coordinates to the copper atom to form intermediate **3**. After that, the nitrogen of the azide in **3** attacks the carbon of the acetylide and form the unusual six-membered copper(III) metallacycle **4** and finally release the triazole product. Moreover,

it proceeds with high yields and is several orders of magnitude faster than the uncatalyzed reaction.[10] The active Cu(I) catalyst can be generated from Cu(I) salts or Cu(II) salts using sodium ascorbate as the reducing agent. Addition of a slight excess of sodium ascorbate, as a reducing agent, prevents the formation of oxidative homo coupling products.
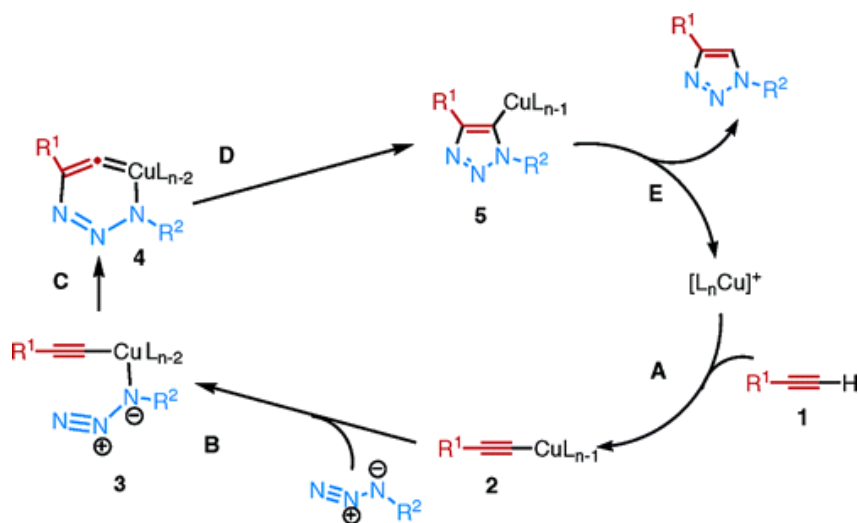
Scheme C 2 Proposed Reaction Mechanism (taken from reference 10)

However, copper is believed to be cytotoxic and therefore the application for biomolecules is limited.[11] For click reactions to be used in bioorthogonal reactions (that is, reactions can occur inside of living systems without interfering with native biochemical processes).[12] Copper-free azide-alkyne cycloaddition (Scheme C 1) has been first developed by Carolyn Bertozzi.[13] The alkyne group activated by electron-withdrawing substituents enables catalyst-free azide-alkyne coupling in high yields at moderate temperatures both in solution[14] and on surfaces.[15, 16] Although this reaction produces a regioisomeric mixture of triazoles, the lack of regioselectivity is not a major concern for its applications in bioorthogonal chemistry.

A search for alternative catalysts revealed that pentamethylcyclopentadienyl ruthenium chloride [Cp*RuCl] complexes are able to catalyze the cycloaddition of azides to terminal alkynes regioselectively leading to 1,5-disubstituted 1,2,3-triazoles (RuAAC, Scheme C 1).[17] In addition, RuAAC can also be used with internal alkynes, providing fully substituted 1,2,3-triazoles, which contrasts with CuAAC.

C.1.2 Click Chemistry on Surfaces

Ever since Click Chemistry was first introduced by Sharpless in 2001, it has turned into a highly productive area of research with exponential growth over the past few years. By 2008, more than 600 papers and more than 10,000 citations were associated with term "Click Chemistry".[18] The application of Click Chemistry toward material science, polymer chemistry and biotechnology has been an extraordinary success story. In this thesis, we focus on Click Chemistry used to fabricate alkyne and azide functionalized surfaces while also highlighting the application of click reactions for site-specific surface reactions. Most coupling reactions available for surface functionalization are limited by incomplete conversions, nonspecificity, harsh reaction conditions, and side reactions. In this respect, click reaction has provided an excellent alternative due to the mild reaction conditions, high conversions, and selectivity.[4, 19] This reaction can be run with either azides or alkynes on surfaces (Scheme C 3), however the azide-modified surfaces offer the advantage of the azide's characteristic spectroscopic features. A strong asymmetric stretch at 2100 cm^{-1} is observed in the infrared spectrum and a 2:1 doublet is observed in the nitrogen high resolution X-ray photoelectron spectrum.[20] The former spectroscopic

method is especially convenient for our group and allows for spectroscopic observation of the disappearance of the azide group as a method to monitor the reaction.
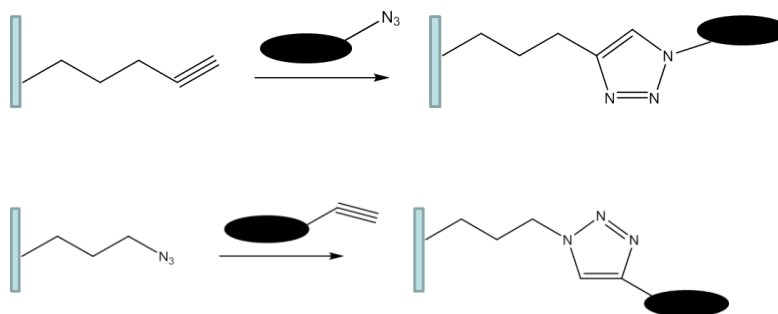
Scheme C 3 Azide or alkyne functionalized surfaces for click reaction

Click reactions for functionalization of a variety of surfaces were reported by different research groups. Hamers and coworkers have demonstrated the use of the Cu(I)-catalyzed azide-alkyne cycloadditon reactions to form electrochemically and photoelectrochemically active molecular interfaces on SnO_2 nanoparticle thin films, as illustrated in Figure C 1(a).[21] The results showed that the short linker provides a high density azide-functionalized surface that can be coupled with redox and photoactive molecular structures.[21] Schubert and coworkers have reported an approach that utilizes the click reaction to click a coumarin 343 derivative as a fluorescent dye molecule on nanostructured surfaces for read out of sensors (Figure C 1 (b)).[22] Chaikof and coworkers have demonstrated the applicability of azide-alkyne cycloaddition reactions for the highly reactive immobilization of a diverse series of biomolecules, including biotin, carbohydrates, and proteins onto an alkyne-terminated PEGylated surfaces (Figure C 1(c)).[23] This surface reaction proceeded to completion at low temperature and in water to immobilize biomolecules without formation of side products. Yogo and his group

have reported a method to synthesize folic acid-functionalized Fe_3O_4 nanoparticles without the loss of the α-carboxylic acid group of folic acid (FA) by applying Click Chemistry (Figure C 1 (d)).[24,25]
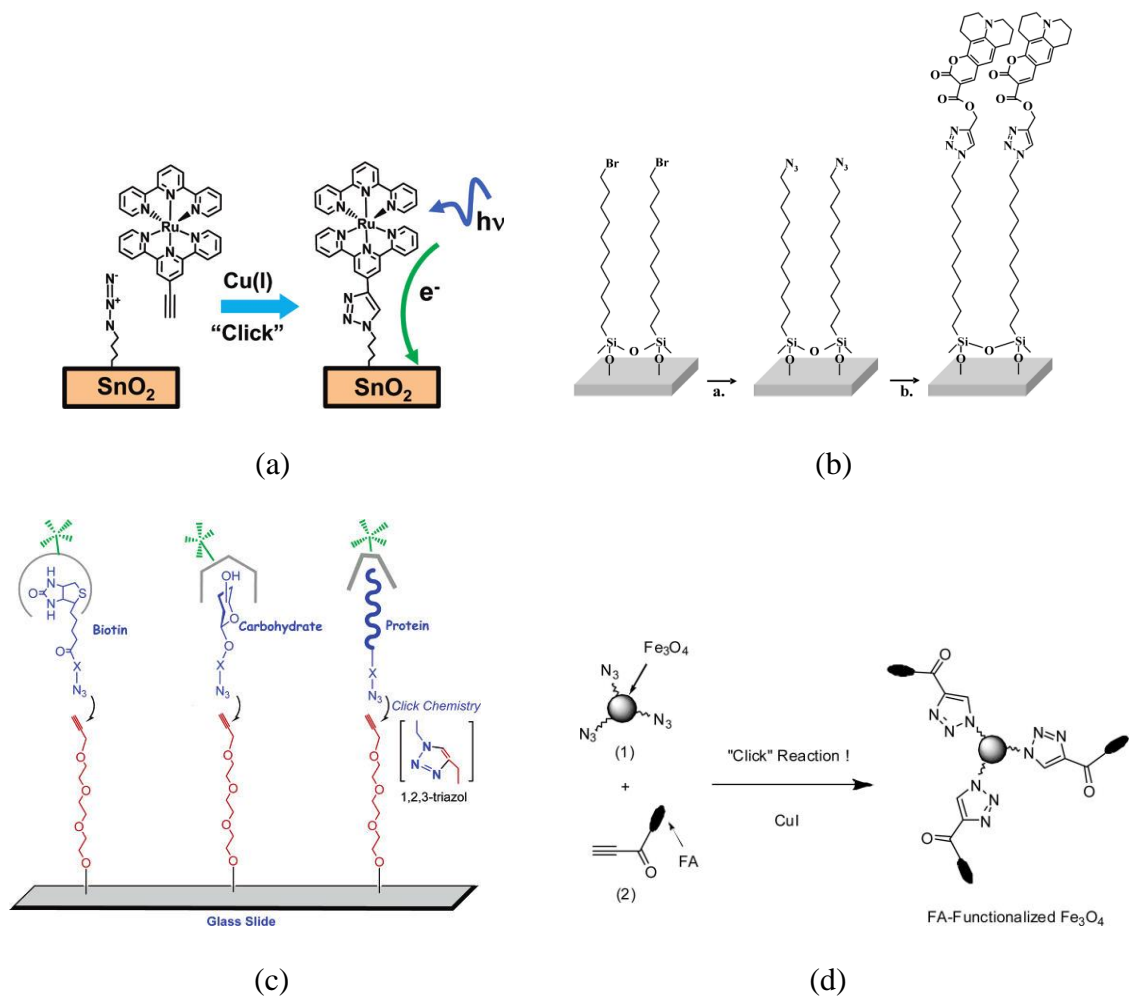
Figure C 1 A schematic representation of (a) a ruthenium terpyridyl complex with azide modified SnO_2 surfaces (taken from reference 21). (b) coumarin derivative with nanostructured surfaces(taken from reference 22). (c) azide-alkyne cycloadditions of azide-derivatized biomolecules (taken from reference 23). (d) FA-functionalized magnetite NPs via click reaction (taken from reference 24).

Laurence Motte and coworkers have compared the well-known carbodiimide chemistry and Click Chemistry for the elaboration of a "nanoplatform" by grafting of a

fluorophore rhodamine and the targeting peptide, as illustrated in Figure C 2. They have demonstrated that click reactions are more efficient for the nanoparticle functionalization than the carbodiimide coupling.[26]
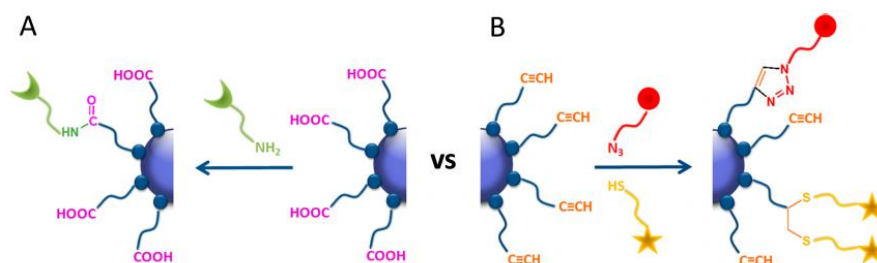
Figure C 2 A schematic representation of Carbodiimide (A) vs Click Chemistry (B) (taken from reference 26).

A disadvantage of click reactions on surfaces mentioned above is the use of Copper (I) as catalysis. Copper (I) is cytotoxic, copper salts can react with oxygen to generate reactive oxygen species, and aqueous copper (I) can disproportionate into copper (II) and copper (0).[4] Copper-free click chemistry was applied as an attractive alternative method for surface modification. Copper-free click chemistry on surfaces avoids not only the cytotoxic properties of copper but also prevents the deposition of traces of metal.[27] The absence of Cu(I), however, results in lack of regioselectivity so it is used when the regioselectivity is not a major concern. Copper-free click chemistry is not well explored on surface studies, and only few researcher groups have investigated it. Hoffman and coworkers developed a two-step process based on copper-free click chemistry to functionalize the silicon nanowires with specific organic substituents (Figure C 3).[28]
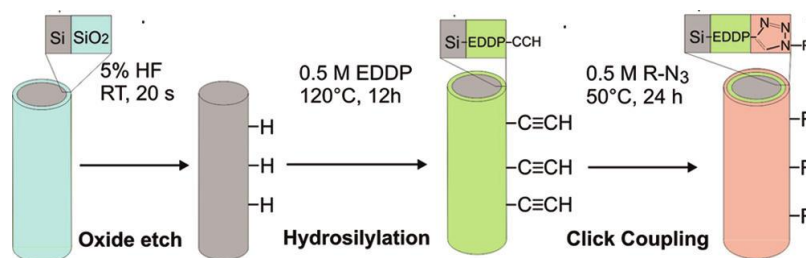
Figure C 3 Surface functionalization of silicon nanowires with an electron-deficient alkyne 1,2-ethanediol dipropiolate followed by alkyne-azide click coupling with an azidoalkane (taken from reference 28).

In our case the absence of copper deposits was important, as we were planning to employ this method to develop ZnO/MgZnO biosensors where contamination by copper could react with biomolecules and also form deposits on the detector active area, leading to errors of detection.[29] The contamination of the films by copper species was observed in our earlier experiments, as the films surface exhibited an unevenly distributed orange-metallic deposit that could not be washed by organic solvents or water. We are uncertain about the nature of the copper species that contaminate the films; however, our observations are consistent with those reported in literature where the presence of metallic copper as a byproduct of the click reaction conducted on surfaces has been reported.[28,30,31] Although the Cu-free cycloaddition may produce a mixture of triazole regioisomers, this is not a concern in our case, as the reaction is used only as a functionalization method.

C.2 Results and Discussion[*]

*Physical adsorption or direct binding of molecules or biomolecules on a surface involves simple molecules, but results in steric hindrance, aggregation, lack of specificity, poor orientation, and low stability and, ultimately, compromised properties. Hence, there is the necessity to develop a well-controlled interfacial chemistry. The strategy we previously reported involved building first a "functional" layer that can then react with other molecules on ZnO nanostructured surfaces.[29,32] This approach, involving the displacement of a bound dithiane or a succinimide ester by a nucleophile, has been used for the development of biosensors.[33]

In this chapter, we extended this approach to functionalization of ZnO and MgZnO nanostructured surfaces through Copper-free click chemistry. Three terminal acetylenic derivatives, 1-ethynylpyrene, alkynated biotin and alkynyl folic acid (Scheme C 4), were used to react with the N_3-functionalized ZnO and MgZnO nanorods surface. 1-ethynylpyrene was employed for characterization purposes, as it is a highly emissive fluorophore and an excimer probe. Biotin was selected as a small molecule that has high binding affinity for protein streptavidin, a classical molecule-protein interaction often selected in proof-of-concept recognition methods. In this case, for characterization purposes, we used a fluorescent tagged streptavidin, streptavidin-FITC, with a strong emission centered at 520 nm (λ_{exc} = 495 nm). Alkynyl folic acid was chosen to react with the N_3-functionalizaed MgZnO nanorods surface. Folic acid (FA) is water-soluble

---

[*] IMPORTANT NOTE: The sentences or paragraphs within asterisks in this thesis were slightly modified from papers of which I am a co-author.

vitamin B₉. FA has a high affinity for folate receptors (FRs), which are overexpressed in various types of human tumors but usually are absent in most normal tissues.[34] FA has a number of advantages as a tumor-targeting ligand: (i) easy availability; (ii) low cost; (iii) applicability over a wide range of tumors, including ovarian, breast, lung and laryngeal; (iv) potential for repeatable administration due to its small size.[24] The α-carboxyl group is essential for high-affinity binding to FRs on human tumors; therefore the α-carboxyl group should not be modified or substituted. Folic acid has pH value from 0 to 7 according to different concentration which could etch the ZnO nanostructured layers.[35] Hence, we proposed MgZnO as alternative nanomaterials since MgZnO nanorods has increased resistance to acids and bases.
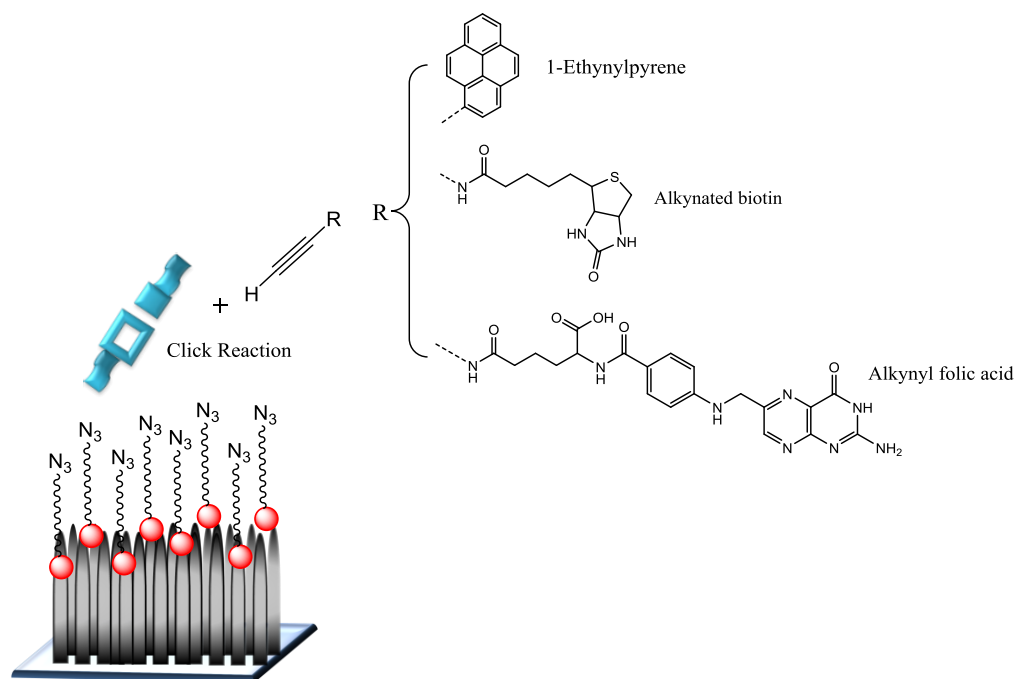
Scheme C 4 Copper-free click chemistry on ZnO/ MgZnO nanostructured surfaces

C.2.1 Nanomaterial Synthesis

The Growth of ZnO and MgZnO Films would not have been possible without our collaborators at Rutgers University-New Brunswick, Dr. Pavel Ivanoff Reyes and Prof. Yicheng Lu.

ZnO Films Growth: Nanostructured ZnO films were grown on glass substrates using the metal organic chemical vapor deposition (MOCVD) technology. Diethylzinc and oxygen were used as the metalorganic Zn source and oxidizer, respectively. The as-grown films show the "nanorod" arrays aligned perpendicularly to the growth plane. Each ZnO nanorod is about 0.5 µm long and 40 nm in diameter, in Figure C 4.*
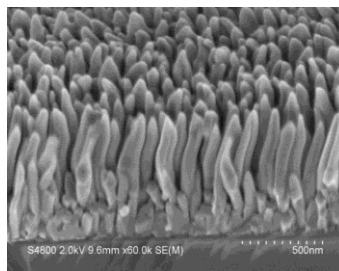
Figure C 4 FESEM image of a 0.5 µm-thick MOCVD-grown ZnO nanorod film on glass

MgZnO Films Growth: Nanostructured ZnO films were grown on glass substrates using the metal organic chemical vapor deposition (MOCVD) technology. Diethylzinc and bis(methylcyclopentadienyl) magnesium were used as the metalorganic Zn and Mg source respectively. Oxygen was used as oxidizer. Each MgZnO nanorod is about 0.5 µm long. A field emission scanning electron microscope (FESEM) image for the nanostructured MgZnO film is shown in Figure C 5.
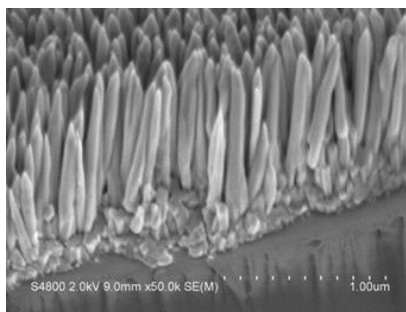
Figure C 5 FESEM image of a 0.5 µm-thick MOCVD-grown MgZnO nanorod film on glass

C.2.2 Biofunctionalization of ZnO with alkynylpyrene

*The functionalization procedure for 1-ethynylpyrene is illustrated in Scheme C 5. The 11-azidodecanoic acid, **6**, was anchored to the MOCVD-grown ZnO nanorod films surface through the –COOH group, (Scheme C 5, Step A), leaving the N_3 group available for click reaction with the alkyne moiety. In Step B, 1-ethynylpyrene, **3**, was reacted with the azido-modified ZnO nanorod films. In a control experiment, compound **5** was directly bound to a ZnO nanorod film, Scheme C 5, to yield a functionalized layer identical to that obtained by the stepwise method.
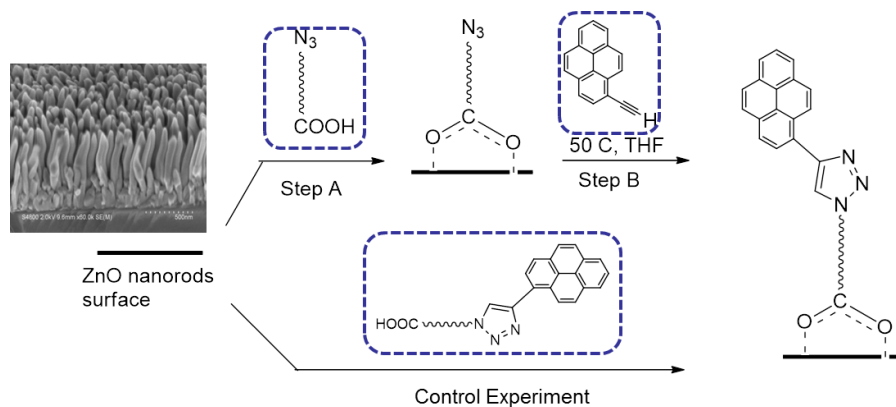
Scheme C 5 Functionalization of ZnO nanorod films with pyrene by Cu-free click reaction and direct binding of pyrene derivative **5**.

Synthesis.

The synthesis of 11-azidodecanoic acid **6** (Scheme C 6) was achieved through azide substitution of bromine.[23] 1-Ethynylpyrene **3** was synthesized through Sonogashira coupling reaction with trimethylsilylacetylene followed by deprotection with TBAF.[36] For a control experiment, 11-(4-(Pyren-1-yl)-1H-1,2,3-triazole-1-yl) undecanoic acid **5** was prepared through a multi-step synthesis as shown in Scheme C 6. The first step is a Fisher esterification of 11-bromoundecanoic acid **1** to increase the solubility of the molecules. The resulting ester was reacted with sodium azide to afford **2**.[37,38] Click reaction with Cu(I) afforded ester **4**.[39] The active Cu(I) catalyst was generated from Cu(II) salts using sodium ascorbate as the reducing agent. Addition of a slight excess of sodium ascorbate prevents the formation of oxidative homo coupling products. The completion of the click reaction was monitored by FTIR-ATR, as illustrated in Figure C 6. The disappearance of the azide band ($\upsilon_{as}(N_3)$) in the 2120 cm^{-1} region indicates completion of reaction. The final step is hydrolysis of the ester group to form carboxylic acid as anchor group for functionalization of nanostructured ZnO surfaces.[40] The absorption and fluorescence emission spectra of compound **5** are shown in Figure C 7.
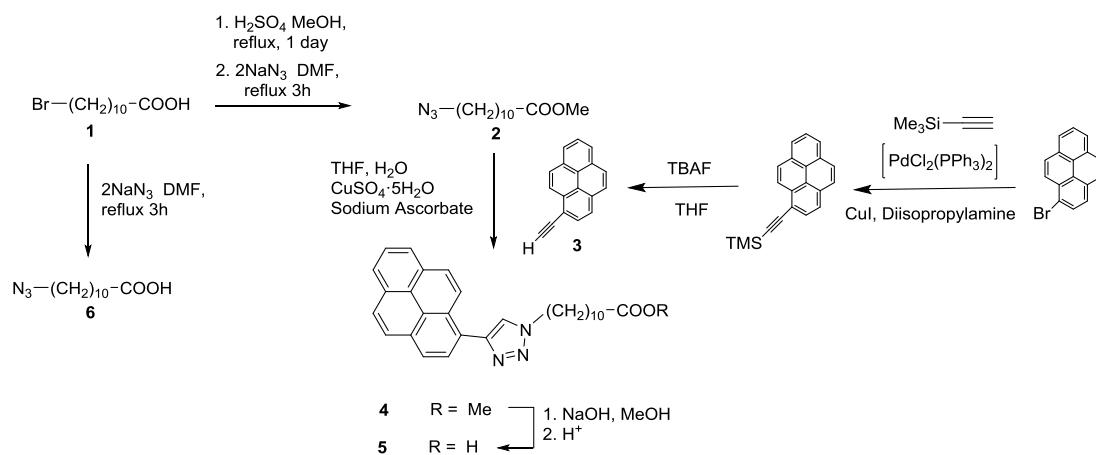
Scheme C Synthesis of azido- (**6**) and pyrenyl-substituted (**5**)
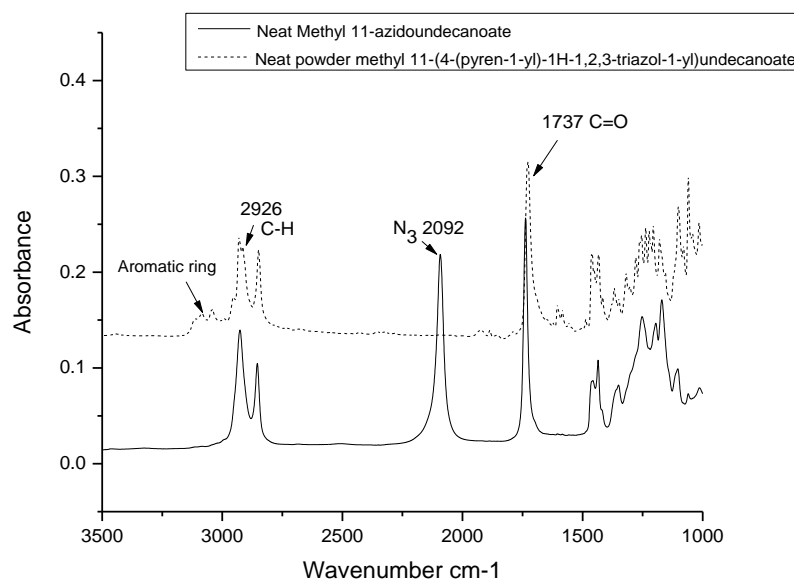
Figure C 6 FTIR-ATR of Click Chemistry bifunctional linkers.
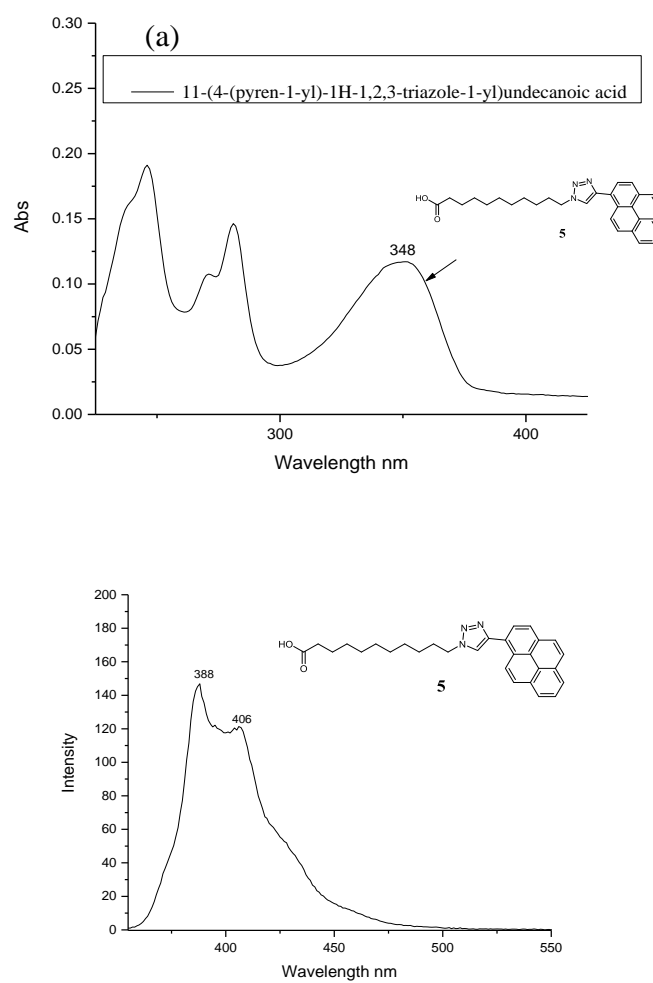
Figure C 7 (a) UV adsorption spectrum of compound **5**. (b) Fluorescence emission spectrum of 5, λ$_{ex}$=348nm

Step A formation of bifunctional linker on ZnO nanorod surface. The 11-azidodecanoic acid bifunctional linker **6** was bound to ZnO nanorod films by using the droplet method which was previously described.[29] Binding of the –COOH group on ZnO nanorod surface resulted in spectral changes in the carbonyl region of FTIR-ATR spectrum of **6**, as shown in Figure C 8(a). The carbonyl asymmetric stretch (ν_{as}(C=O)) band of the free acid at 1703 cm^{-1} was replaced by bands assigned to the carboxylate asymmetric stretch, ν_{as}(O$\cdots$C$\cdots$O), at 1540 cm^{-1} and at 1460 cm^{-1}, and the broad OH stretch of the COOH group centered at 3500 cm^{-1} disappeared. The C-H stretch bands of the long saturated alkyl chain were visible in the region below 3000 cm^{-1} in the bound films. Overall, the observed spectral changes were indicative of the 11-azidodecanoic acid linker binding on ZnO nanorod films through the COOH group. The low intensity of the IR spectra of the films was expected, as the result of low surface area of the 500 nm-thin ZnO films and it was consistent with our previous observations for this type of film.[29]

Step B Cu-free click reaction of 1-ethynylpyrene. The azido-functionalized ZnO layer (abbreviated **6**/ZnO) was reacted with 1-ethynylpyrene as a fluorescent probe unit to test whether small chromophoric groups or other larger molecules can be added by click chemistry. Typically Cu(I) is used as a catalyst in click reactions, that can be carried out at room temperature. However, we found that, in a variety of conditions, copper species easily reduced to Cu(0) and deposited on the surface of the films, forming an insolubler layer. Hence, the click reaction was performed in the absence of copper by immersing the azide group modified ZnO films in a small volume of 1-ethynylpyrene solution (3 ml of a 45 mM DMF solution), and heating to 50 $^{\circ}$C. The progress of the

reaction was monitored by FTIR-ATR, following the disappearance of the azide band ($\nu_{as}(N_3)$) in the 2120 cm^{-1} region in the spectra of the films, and observing the appearance of a weak band at 3035 cm^{-1} and bands in the ~1600 cm^{-1} region, which we assigned to the C-H and C=C stretch of the pyrene ring, respectively, Figure C 8b.
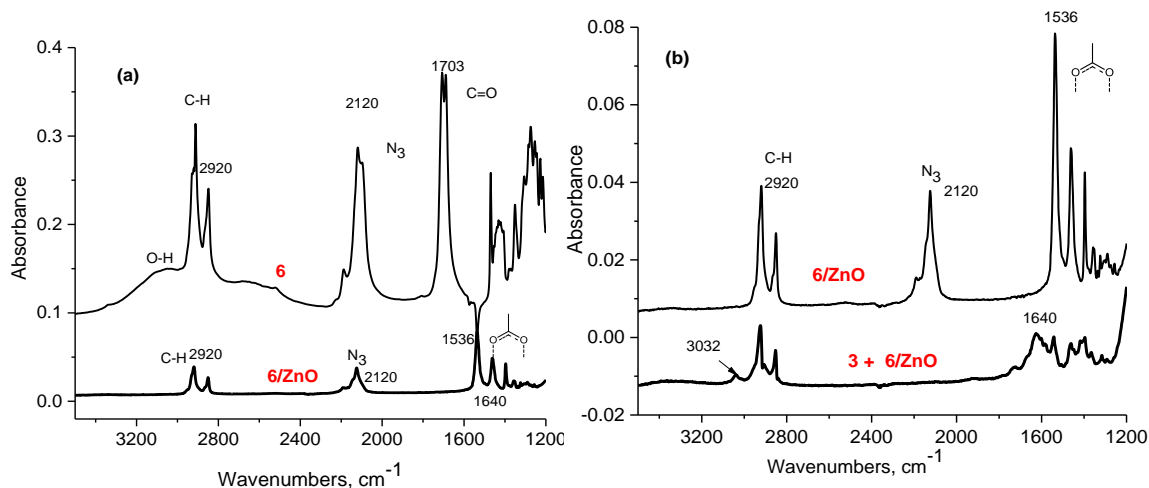
Figure C 8 FTIR-ATR spectra of (a) 11-azidodecanoic acid (**6**) (top) and bound to ZnO, **6**/ZnO (bottom). (b) **6/**ZnO before (top) and after (bottom) click reaction with 1-ethynylpyrene.

The disappearance of the azide band indicates completion of reaction, and may also give an insight on the surface packing of the azide-capped linker on the surface of the films. The cross section of the azidodecanoic acid should be close to the cross section of an alkyl carboxylic acids, about 0.2 nm^2, and is much smaller than the cross-section of a pyrene. The fact that no residual azide was observed after the click reaction with 1-ethynylpyrene, suggests that the azide-capped linkers do not form a tight monolayer.

The click reaction with **3** was also monitored by fluorescence emission ($\lambda_{ex} = 348$ nm). The fluorescence spectrum of the ZnO nanorod surface after click reaction with 1-ethynylpyrene is shown in Figure C 9. The intensity of the emission spectrum for blank ZnO following excitation at 348 nm, however was negligible compared to the emission of

the bound pyrene. The two emission peaks centered at 386 and 475 nm in Figure C 9 were assigned to pyrene monomer and pyrene excimer emission bands, respectively. The predominance of the excimer emission band suggests that the pyrene units come in close contact (<3.5 Å) on the ZnO nanorod surface. This proximity, however, taken together with the complete disappearance of the azide band (see above), may not be necessarily indicative of a regular (straight–up) or compact packing on the surface. As previously reported, pyrene excimer and close contacts could be the result of a disordered layer, where the pyrene moieties come in close proximity.[41] The fact that excimer emission was not, at least fully, quenched, may be due to the presence of a long saturated linker separating the emissive unit from the semiconductor surface, whereas the overlap between the pyrene emission and ZnO band edge may also, in part, explain the small monomer emission.
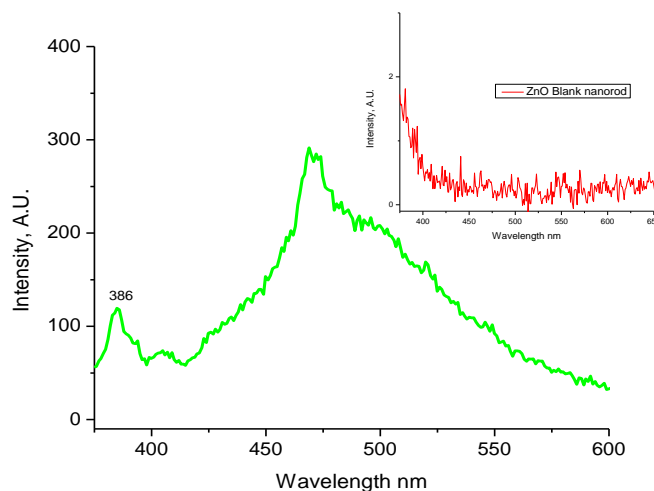
Figure C 9 Fluorescence emission spectrum of **6**/ZnO nanorods after click reaction with 1-ethynylpyrene, $\lambda_{ex} = 348$ nm. *Inset:* emission of the blank ZnO nanorod films, following excitation at 348 nm.

To determine whether the azide-substituted linker is necessary for the binding of the pyrene on ZnO nanorod surface, and that the pyrene is not simply physisorbed, fluorescence was measured after Step A and after Step B in a control experiment as indicated in Scheme C 5. Shown in Figure C 10 (b) and (d) are the fluorescence microscopy images of the films. It was found that only the azide-modified ZnO film that was reacted with 1-ethynyl pyrene shows the fluorescence. The fluorescence microscopy image in Figure C 10 (c), however reveals a non-uniform binding of the linker to the ZnO nanorods, whereas our previous work on ZnO films coated with fluorescent biomolecules yielded uniform layers.[29] The inhomogeneity is larger than the 100-micron scale. FESEM, which was used to probe the integrity of the ZnO nanorod layer after the functionalization reactions, as discussed below, does not provide information about the coverage of the nanorods, which could be heterogeneous at the nanoscale. In addition, we have observed photobleaching during the fluorescence microscopy measurements and we think that this may in part contribute to the poor quality of the images. In summary, we think that the highly inhomogeneous emission intensity distribution may be occurring at nano and microscale, and could be the result of a combination of inhomogenous binding and photobleaching.

One concern that needed to be addressed was the possibility that the ZnO layer was etched during the multi-step functionalization sequence. Etching of ZnO to zincate salts by bases and acids, including carboxylic acid derivatives, is often observed.[42] The FESEM image in Figure C 10 (a) of the ZnO nanorod on glass substrate after the entire functionalization and click reaction procedure (Steps A-B) shows an intact ZnO layer, indicating that the click reaction sequence does not result in observable etching of ZnO.
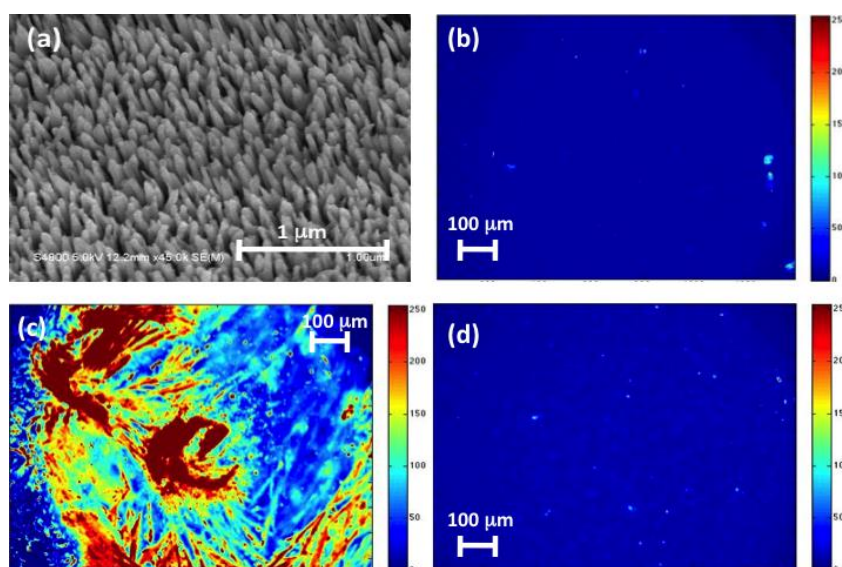
Figure C 10 (a) FESEM of the ZnO nanorod film after Steps A-C. Fluorescence microscopy image of a ZnO nanorods film (b) after Step A (**6**/ZnO) (c) after Step B (click reaction of **3** with **6**/ZnO) and (d) image of a ZnO film reacted with 1-ethynylpyrene.

As a control experiment, 11-(4-(pyrene-1-yl)-1H-1, 2, 3-triazole-1-yl)undecanoic acid (**5**) was directly bound to ZnO nanotip films, as shown in Scheme C 5. The ZnO nanotip film was reacted using the droplet method[25] with a 5 mM solution of **5** in THF/H_2O (2:1) for 12-15 h, then rinsed thoroughly with neat solvent and dried under nitrogen flow. The FTIR-ATR spectrum of the resulting film, shown in Figure C 11, shows the disappearance of the ν_{as}(C=O) band at 1698 cm^{-1} and of the ν_{as} (O-H) band in the 3000 cm^{-1} region, which is present in the spectrum of neat **5**, and the appearance of the bands in the ~ 1600-1400 cm^{-1} region, suggesting binding of the linker through carboxylate bonds. Similarly to what observed for the click reaction, FESEM images of the films after the binding of **5** indicated that there was no observable etching of the ZnO films.
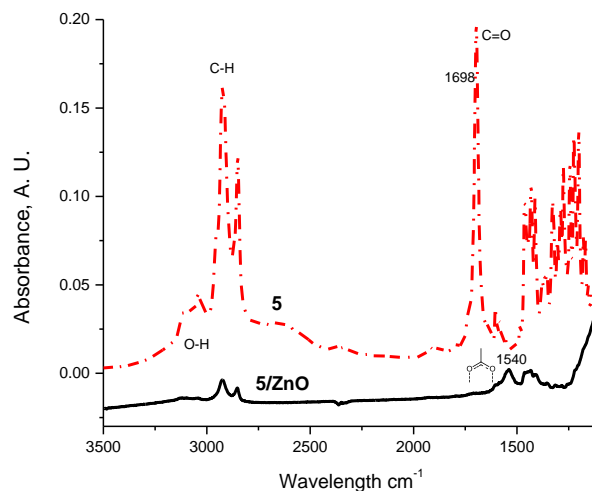
Figure C 11 FTIR-ATR of (a) compound **5** (top, red dashed line)and (b) **5**/ZnO nanorod film (bottom, black solid line)

The FTIR-ATR spectra of the films after the click reaction sequence (Steps A-B) were similar to the films functionalized by direct binding of pyrene derivative **5**, as shown in Figure C 12. Both films exhibited the characteristic ν_{as}(C-H) bands of the long saturated alkyl chain and aromatic ring in the 3000 cm^{-1} region and in the 3100 cm^{-1}, respectively, and the appearance of the carboxylate bonds bands in the~ 1600-1400 cm^{-1} region. This observation corroborates our conclusion that the click chemistry occurs on the surface, and leads to a pyrenyl-substituted ZnO layer.
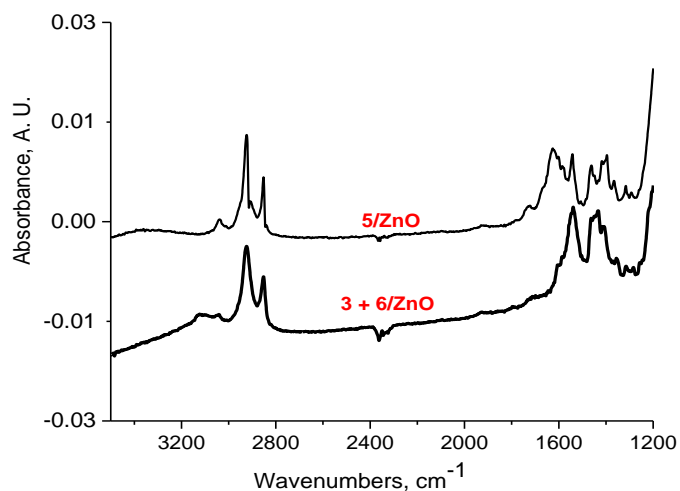
Figure C 12 FTIR-ATR spectra of 1-(4-(pyren-1-yl)-1H-1, 2, 3-triazol-1-yl)undecanoic acid (**5**) directly bound to ZnO nanorods (top) and **6**/ZnO nanorods films after click reaction with 1-ethynylpyrene (bottom).

Fluorescence emission spectra and fluorescence microscopy images of the ZnO films after the control experiment shown in Figure C 13 were very weak, suggesting a low surface coverage, but consistent with the spectra from Scheme C 5, Step B. The spectrum suggests the presence of pyrene static excimer (i.e. between pyrene molecules associated in the ground state), suggesting that the pyrene units are packed closely, at least in some areas of the ZnO nanorod surface. The FESEM image in Figure C 13 (insert) shows the apparently intact surface morphology of the ZnO nanorods on glass after the control experiment.
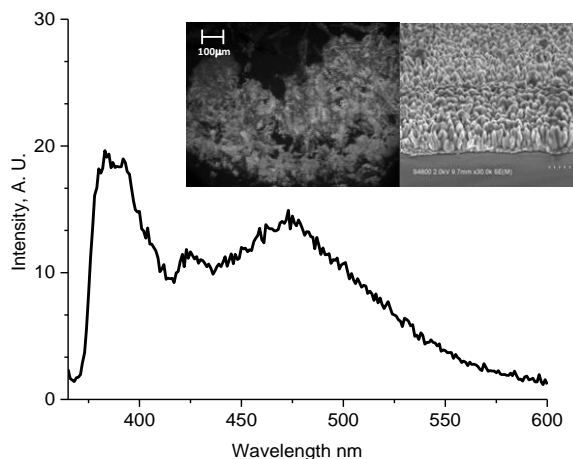
Figure C 13 Fluorescence emission spectrum of a **5**/ZnO film, λ_{ex} = 348 nm. *Inset:* Fluorescence microscopy image and FESEM image of the film after the control experiment involving the direct binding of **5**

The amount of loading on the surfaces of the films, however, could not be determined in a quantitative manner from the fluorescence photon count from each pixel of the fluorescence microscopy image, as we used a filter set that did not exactly match the peak emission of pyrene. Therefore, the intensity of the pixels did not exactly correspond to the actual photon count of the fluorescing molecules and may not be an accurate indication of the amount of loading on the films. The loading will be determined in future experiments by measuring frequency shift measurements of ZnO films grown on quartz crystal microbalances, as we have done in our earlier work.[29]

C.2.3 Biofunctionalization of ZnO with biotin

Biotin, a water soluble B-vitamin, exhibits high affinity with streptavidin, with a binding dissociation constant, K_d, in the order of 4×10^{-14}M.[43] Here, alkynated biotin **9** was bound to ZnO nanorod films by click chemistry under mild reaction condition and short reaction times (Scheme C 7 Step C). The biotin-functionalized films were reacted with streptavidin-fluorescein isothiocyanate (streptavidin-FITC) (Scheme C 7 Step D). The synthesis of alkynated biotin was processed through amide formation by carbodiimide (Scheme C 8). EDC was used to activate the carboxylic acids for amide formation, and N-hydroxysuccinimide was often added to increase yields and decrease side reactions.
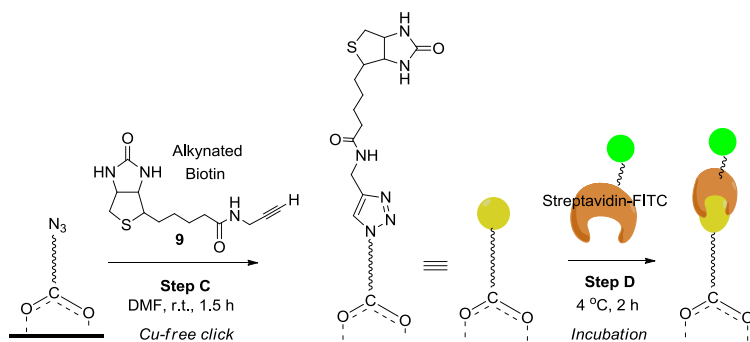
Scheme C 7 Functionalization of ZnO nanorod films with ethynylated biotin, followed by streptavidin-FITC binding.
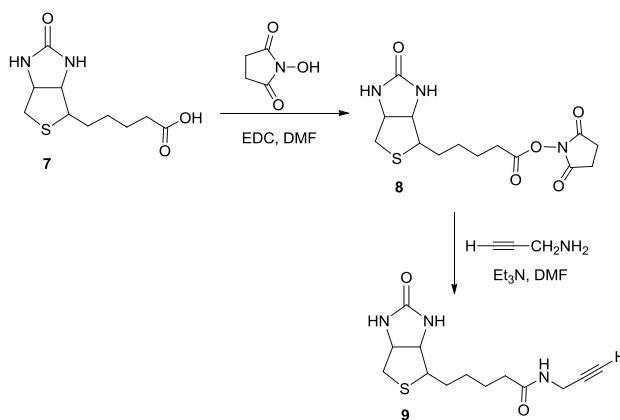
Scheme C 8 Synthesis of alkynated biotin (**9**).

FTIR-ATR was used to monitor the progress of the click reaction. The spectrum of the azide-terminated monolayer (Figure C 14, bottom line) showed a strong band at 2120 cm^{-1} characteristic of the asymmetric stretching band[44] ν_{as} of the azide group, $_{as}(N_3)$. The disappearance of the $\nu_{as}(N_3)$ band (Figure C 14, middle line) suggests the completion of the click reaction. The bands assigned to the carboxylate asymmetric stretch $\nu_{as}(O^{...}C^{...}O)$ from bound to ZnO nanorod surface remained unchanged. The appearance of a new band in the 1690 cm^{-1} region was assigned to the formation of an amide bond of alkynated biotin. The spectrum broadened considerably after Step D in Scheme C 7(Figure C 14, top line).
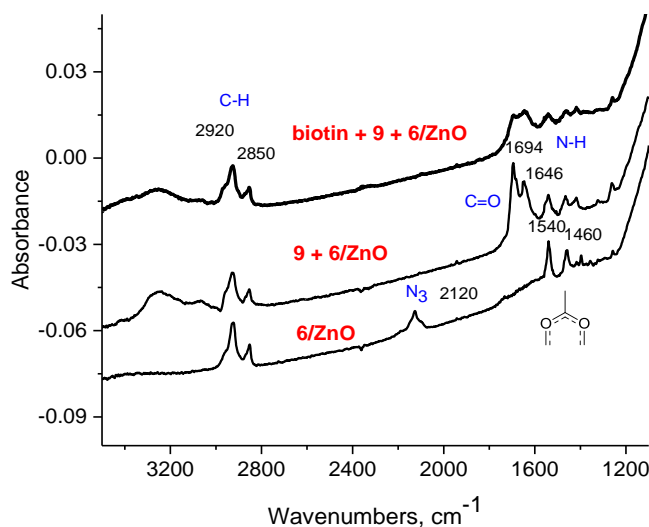
Figure C 14 FTIR-ATR of 11-azidodecanoic acid, **9**, bound to ZnO nanorods (bottom), azide functionalized ZnO nanorods click react with alkynated biotin (middle), Biotin bound to streptavidin (top).

The biotin-streptavidin bond formation was probed by steady-state fluorescence emission. The ZnO nanorod films with immobilized biotin, obtained after click reaction between alkynated biotin and the N_3-substituted ZnO nanorod films, did not fluoresce.

After treatment with streptavidin-FITC, upon excitation at 495 nm, the films were fluorescent as shown in Figure C 15. The fluorescence emission spectra of free streptavidin in solution and when bound to surface were very similar in shape. This, and the presence of significant emission suggest that at least not all fluorophores are in close contact, as self-quenching of the FITC would be occurring.[45] The fluorescence emission maximum (520 nm) of the films after Step D was identical to that of a streptavidin-FITC in PBS buffer solution, shown in Figure C 15 as a blue line. The FESEM image (inset) shows the surface of a ZnO nanorod film still intact after Step C.
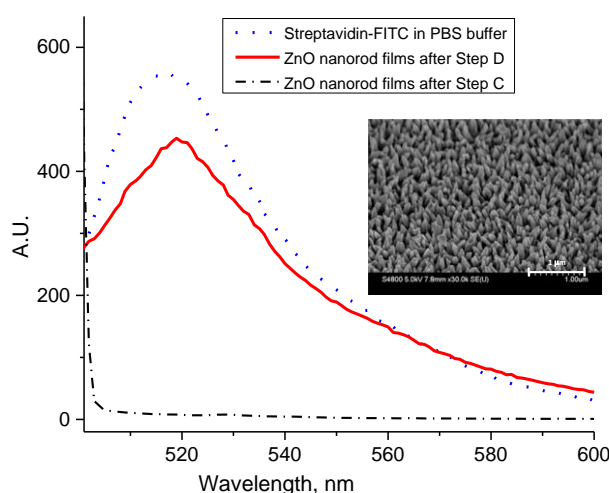
Figure C 15 Fluorescence emission spectra of streptavidin-FITC in 10 mM PBS solution (blue line), ZnO nanorod films after Step D (red line) and ZnO nanorod films after Step C(black line). *Inset:* FESEM image of ZnO nanorod surface after Step C.

As mentioned previously in the section describing the experiments with pyrene, the development of QCM sensors will allow the quantification of the mass loading measurements for each step, allowing estimating how many biotins will bind to streptavidin. However, we think that the biomolecules are not tightly packed on the

surfaces of the films, especially given the large size of the biotin-streptavidin complex, reported to be $47.53 \times 52.62 \times 23.58$ Å from crystallographic data*.[46]

C.2.4 Biofunctionalization of MgZnO with folic acid

The folate receptor (FR) is higly expressed on most epithelial cancer cells while normal cells show only restricted expression of FR. As a result, the FR has become a promising target in oncology.[47]   The α-carboxyl group is essential for high-affinity binding to FRs on human tumors; therefore the α-carboxyl group should not be modified or substituted for targeting tumors.   Here as illustrated in **Error! Reference source not found.**, alkynyl folic acid **11** was bound to MgZnO nanorod films by click chemistry under mild reaction condition and short reaction times. Due to the acidity of folic acid, which can have pH from 0 to 7 depending upon concentration, the ZnO nanostructured layers can be etched.[35]   Hence, we proposed MgZnO as alternative nanomaterials since MgZnO nanorods has increased resistance to acids and bases. The synthesis of alkynyl folic acid was achieved through carbodiimide reaction (Scheme C 9).
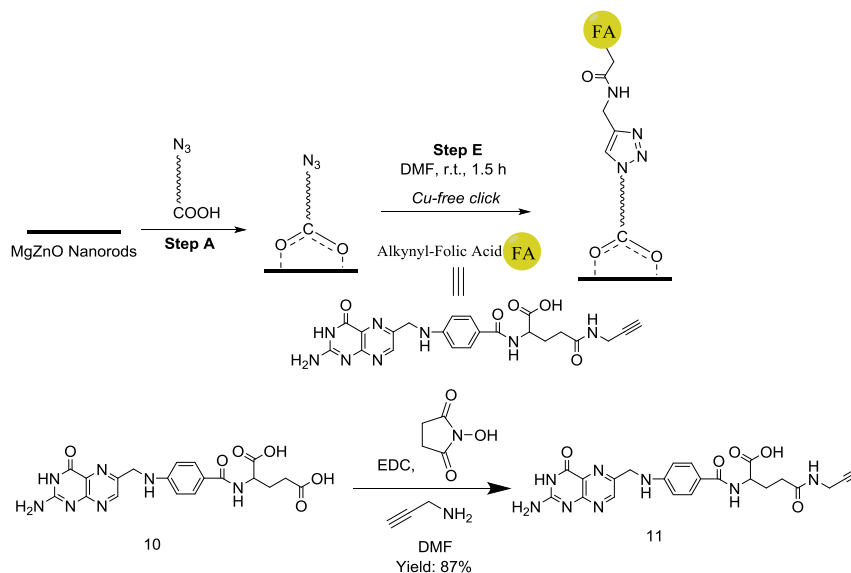
Scheme C 9 Functionalization of MgZnO nanorod films with alkynyl folic acid

FTIR-ATR was used to monitor the progress of the click reaction. The spectrum of the azide-terminated monolayer (Figure C 16, middle black line) showed a strong band at 2124 cm^{-1} characteristic of the asymmetric stretching band ν_{as} of the azide group, $\nu_{as}(N_3)$. The disappearance of the $\nu_{as}(N_3)$ band (Figure C 16, top blue line) suggests the completion of the click reaction. The appearance of a new band in the 1695 cm^{-1} and 1608 cm^{-1} region was assigned to the formation of an amide bond of alkynyl folic acid.
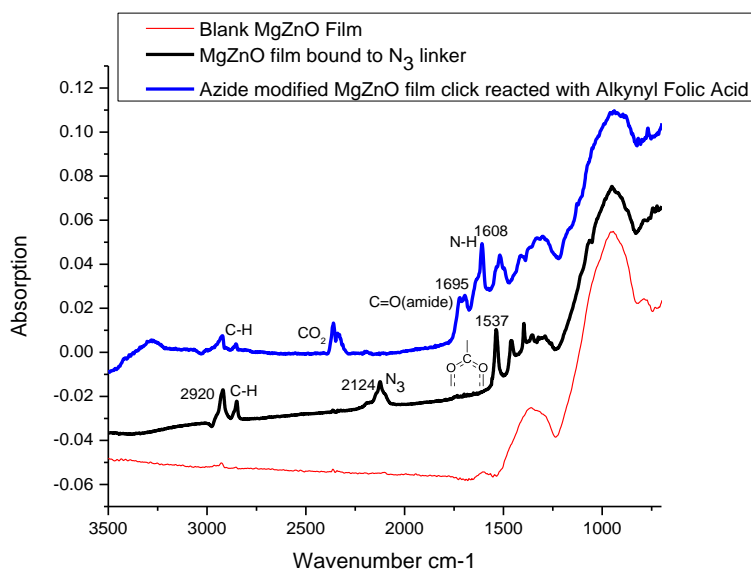
Figure C 16 FTIR-ATR of Black MgZnO nanorods (bottom red line), 11-azidodecanoic acid, **9**, bound to MgZnO nanorods (middle black line), azide functionalized MgZnO nanorods click react with alkynated biotin (top blue line).

In summary, alkynyl folic acid was successfully bound to MgZnO through Cu-free click reaction. The application of this methodology on nano-biosensors will be carried on by other member of our group.

C.3 Experimental Section*

General.

Materials: All reactions involving air- and moisture-sensitive reagents were performed under nitrogen atmosphere and in oven-dried or flame-dried glassware. Tetrahydrofurane (THF) was freshly distilled over sodium/benzophenone. Dichloromethane was distilled over calcium hydride. 11-Bromoundecanoic acid (99%, Sigma-Aldrich), sodium azide (99%, Alfa Aesar), 1-bromopyrene (TGI-America), biotin (Sigma-Aldrich), folic acid (Sigma-Aldrich), N-hydroxysuccinimide (Sigma-Aldrich), N-(3-dimethylaminopropyl)-N'-ethylcarbodiimide hydrochloride (EDC, Sigma-Aldrich), propargylamine (Sigma-Aldrich), streptavidin-fluorescein isothiocyanate (streptavidin-FITC) from Streptomyces avidin (Sigma-Aldrich), ethanol 200 proof, and 1-butanol, dimethylformamide were used as received. Freshly prepared 10 mM aqueous phosphate saline buffer (PBS) pH = 7.4 from Sigma was used for preparing the streptavidin-FITC solution. Membrane syringe filters, polytetrafluoroethylene (PTFE) 0.2 μm were purchased from Gelman for removing the bacteria from freshly prepared 10 mM aqueous phosphate saline buffer (PBS) pH = 7.4 solution. 1-Ethynylpyrene was prepared following a published procedure.[36]

Methods: ^{1}H-NMR and ^{13}C-NMR spectra were collected on a Varian NMR spectrometer operating at 499.896 MHz for ^{1}H and 125.711 MHz for ^{13}C. Chemical shifts were reported relative to the central line of the solvent: CDCl$_3$ (δ 7.27 ppm) or DMSO (δ 2.5 ppm) for ^{1}H spectra and CDCl$_3$ (δ 77.27 ppm) for ^{13}C spectra, and coupling

constants (*J*) are reported in Hz. High resolution mass spectra (ESI) were recorded on the departmental FTMS facility. Single attenuated total reflectance infrared (FTIR-ATR) spectra were performed on a Thermo Electron Corporation Nicolet 6700 FT-IR (ZnSe Crystal, number of spectra averaged 128, resolution 4 cm^{-1}). Fluorescence emission spectra were collected on a VARIAN CARY-Eclipse. The films were placed diagonally at a 45° angle in a 1 cm cuvette in air while recording the spectra. Reflection fluorescence images of the ZnO nanorods on glass substrate were collected with an Axiovert 200M confocal fluorescence microscope (Carl Zeiss, Gottingen, Germany) with an excitation bandpass filter of 325 nm – 375 nm full width a half maximum (FWHM) range and 420 nm – 470 nm (FWHM) emission bandpass filter. The wavelength ranges of the filter sets were selected for imaging the fluorescing pyrene layer on the ZnO films. FESEM images were collected on a Hitachi S4800.

C.3.1 Synthesis

Synthesis of Methyl 11-azidoundecanoate (2)[37,38]*:* To a stirring solution of 11-bromoundecanoic acid (1.06 g, 4 mmol) in methanol (6 ml), was added concentrated H_2SO_4 (0.26 ml). The solution was refluxed at 70 °C overnight under an atmosphere of nitrogen, then diluted with CH_2Cl_2 (50 ml) and extracted with water (2×25 ml), saturated aqueous sodium bicarbonate (2×25 ml) and brine (2×25 ml). The organic layer was evaporated in vacuum to afford methyl 11-bromoundecanoate, as clear oil (0.861 g, 77% yield) which was characterized by NMR and used in the next step. ^{1}H NMR δ_H(CDCl$_3$) 3.65 (3 H, s), 3.39 (2 H, t, *J* = 7), 2.29 (2 H, t, *J* = 7.5), 1.85-1.82 (2 H, m), 1.62-1.59 (2 H, m), 1.40-1.28 (10 H, m); ^{13}C NMR δ_c (CDCl$_3$) 174.20, 51.42, 34.08, 33.94, 32.86,

29.39, 29.35, 29.23, 29.14, 28.766, 28.18, 24.95. To a stirring solution of methyl 11-bromoundecanoate (689 mg, 2.5 mmol) in DMF (5 ml) was added sodium azide (321 mg, 5 mmol). The reaction mixture was heated at 85 $^{\circ}$C for 3 h, then diluted with CH_2Cl_2 (25 ml) and washed with 0.1 N aqueous HCl. The organic layer was dried over Na_2SO_4 and evaporated in vacuum to give **2** as a pale yellow oil (600 mg, 99% yield). ^{1}H NMR δ_H(CDCl_3) 3.65 (3H, s), 3.24 (2 H, t, *J* = 7), 2.29 (2 H, t, *J* = 7.5), 1.62-1.27 (14 H, m); ^{13}C NMR δ_c (CDCl_3) 174.17, 51.35, 51.30, 33.95, 29.82, 29.20, 29.10, 28.99, 28.79, 26.59, 26.01, 24.82.

Synthesis of 1-ethynylpyrene (3)[36]:

Sonogashira coupling: To a stirring solution of 1-bromopyrene (1.5 g, 5.3 mmol, 1 equiv) in fresh distilled diisopropylamine (122 mL, 23 mL/mmol), $PdCl_2(PPh_3)_2$ (371 mg, 0.53 mmol, 0.1 equiv) and CuI (203 mg, 1.07 mmol, 0.2 equiv) were added under nitrogen atmosphere. After 10 min, trimethylsilylacetylene (6.7 mL, 47.7 mmol, 9 equiv) was added and the reaction mixture was stirred at 45°C for overnight. The dark reaction mixture was purified by flash chromatography on a silica gel column by eluting with hexanes/ethyl acetate (9:1) to afford a dark solid (1.5 g) after dry under vacuum. ^{1}H NMR (δ_H CDCl_3) δ 8.58 (1 H, d, *J* = 9.0), 8.24 (1 H, d, *J* = 7.5), 8.20 – 8.15 (3 H, m), 8.10 – 8.02 (4 H, m), 0.41 (9 H, s).

Deprotection: To a stirring solution of 1-trimethylsilyethynylpyrene (134 mg, 0.45 mmol, 1 equiv) in THF (20 ml), TBAF (0.5 mL, 0.52 mmol, 1.15 equiv) was added drop by drop over 4-5mins. Keep reaction mixture in dark all the time and monitor the reaction by TLC. After 1h, reaction was completed. Add water (25 ml) into the reaction mixture and extract with dichloromethane (3×50 mL), dry over sodium sulfate and dry under

vacuum. The reaction mixture was purified by flash chromatography on a silica gel column by eluting with hexanes/ethyl acetate (9:1) to afford a pale yellow solid (74 mg) after dry under vacuum. ^{1}H NMR CDCl$_3$) δ 8.61 (1 H, d, $J = 9$), 8.25 − 8.18 (4 H, m), 8.13 − 8.03 (4 H, m), 3.68 (1 H, s).

Methyl 11-(4-(pyren-1-yl)-1H-1,2,3-triazole-1-yl)undecanoate (4)[39]: To a solution of 1-ethynylpyrene (**3**, 280 mg, 1.24 mmol) and methyl 11-azidoundecanoate (100 mg, 0.41 mmol) in THF (6 ml) and water (3 ml), a solution of CuSO$_4$·5H$_2$O (102 mg) in water (1.4 ml) was added in one portion. Then, a freshly prepared solution of sodium ascorbate (162 mg in 0.835 ml water) was added drop-wise and the reaction mixture was stirred for 30 h at room temperature. The progress of the reaction was monitored by FTIR-ATR (disappearance of the N$_3$ stretch band at 2100 cm^{-1} in Figure C.15). Then CH$_2$Cl$_2$ (25 ml) and an aqueous solution of ammonia (15 %) were added (25 ml), and the mixture was stirred for 10 min to extract the Cu(I) salts as [Cu(NH$_3$)$_6$]$^+$ in the aqueous phase. The organic phase was extracted with water (2x25 ml) and filtered through Celite. The solvent was removed under vacuum and the product was purified by column chromatography (hexane/ethyl acetate, 4/1) to afford **4** as a pale yellow powder (119 mg, 62% yield). ^{1}H NMR δ$_H$(CDCl$_3$) 8.65-8.63 (d, 1 H, $J = 10$), 8.30-8.28 (d, 1 H, $J = 10$), 8.24-8.00 (m, 8 H), 4.58-4.55 (t, 2 H, $J = 7$), 3.66 (s, 3 H), 2.32-2.29 (t, 2 H, $J = 7.5$), 2.09-2.05 (m, 4 H), 1.64-1.61 (m, 2 H), 1.61-1.31 (m, 10 H); ^{13}C NMR δ$_c$ (CDCl$_3$) 174.52, 146.59, 131.58, 131.56, 131.08, 128.78, 128.41, 128.08, 127.56, 127.41, 126.29, 125.62,125.36, 125.26, 125.08, 124.94, 124.89, 123.04, 51.66, 50.92, 34.28, 30.62, 29.53, 29.50, 29.40, 29.30, 29.21, 26.80, 25.12. HRMS (ESI)$^+$ *m/z* calcd for [C$_{30}$H$_{33}$N$_3$O$_2$+Na]$^+$ 490.2546, found [M+Na]$^+$ 490.2465.

11-(4-(Pyren-1-yl)-1H-1,2,3-triazole-1-yl) undecanoic acid (5)[40]: To a stirring solution of **4** (43 mg, 0.1 mmol) in CH_2Cl_2 (25 ml), were added 2.5 ml of a 2 M NaOH solution in methanol, and stirring was continued at room temperature for 24 h. The solution was extracted with water (3×25 ml), then 10% HCl was added dropwise until pH~2. The aqueous acidic solution was extracted with CH_2Cl_2 (3×25 ml). The combined organic layers were dried over Na_2SO_4 and evaporated in vacuum to afford carboxylic acid **5** as a white solid (23 mg, 51 % yield). ^{1}H NMR δ_H(CDCl$_3$) 8.71-8.69 (d, 1 H, J = 9), 8.28-8.27 (d, 1 H, J = 8), 8.28-7.96 (m, 8 H), 4.56-4.53 (t, 2 H, J = 7), 2.37-2.34 (t, 2 H, J = 7), 2.09-2.04 (m, 2 H), 1.66-1.61 (m, 2 H), 1.46-1.26 (m, 12 H). HRMS (ESI)[+] *m/z* calcd for $[C_{29}H_{31}N_3O_2+Na]^+$ 476.2406, found $[M+Na]^+$ 476.2308.

11-Azidodecanoic acid (6)[23]: To a stirring solution of **1** (1 g, 3.8 mmol) in DMF (5 ml) was added sodium azide (494 mg, 7.6 mmol). The reaction mixture was heated at 85°C for 3hours, then diluted with CH_2Cl_2 (25 ml) and washed with 0.1 N aq. HCl. The organic layer was dried over Na_2SO_4 and evaporated in vacuum to give **6** as a pale yellow oil (560 mg, 65%). ^{1}H NMR δ_H(CDCl$_3$) 3.26 (2H, t, J = 7.5), 2.35 (2 H, t, J = 7.5), 1.65-1.29 (16 H, m).

Alkynated Biotin (9)[48]: EDC (184 mg, 0.96 mmol, 1.2 equiv) was added to a solution of biotin (200 mg, 0.8 mmol) and N-hydroxysuccinimide (102 mg, 0.88 mmol) in DMF (15 ml). The solution was stirred for 24 h at room temperature under nitrogen, evaporated in vacuum, and the crude solid was triturated with methanol several times to form N-hydroxysuccinimidobiotin **8** as a white solid product (204 mg, 75%). Propargylamine (60 µl, 0.9 mmol, 2 equiv) was added to a solution of **8** (153 mg, 0.45

mmol) and triethylamine (125 μl, 0.9 mmol) in DMF (8.0 ml). The solution was stirred for 24 h at room temperature under nitrogen, concentrated and purified by column chromatography (silica gel, eluent: chloroform/methanol (6/1) to give alkynated biotin **9** as a white solid (90 mg, 75% yield). ^{1}H NMR δ_H(d$_6$-DMSO) 1.29-1.33 (m, 2 H), 1.44-1.51 (m, 2 H), 1.59-1.62 (m, 2 H), 2.07-2.10 (d, 2 H, J = 7.5), 2.57-2.59 (d, 1 H, J = 13.0), 2.81-2.84 (dd, 1 H, J_1= 4.5, J_2 = 5.0), 3.04-3.09 (m, 2 H), 3.83-3.83 (m, 2 H), 4.130 (m, 1 H), 4.29-4.31 (m, 1 H), 6.31 (s, 1 H), 6.36 (s, 1 H), 8.17 (s, 1 H). HRMS (ESI)$^+$ m/z calcd for [C$_{13}$H$_{19}$N$_3$O$_2$S+Na]$^+$ 304.1090, found [M+Na]$^+$ 304.1099, calcd for [C$_{13}$H$_{19}$N$_3$O$_2$S+H]$^+$ 282.1271, found [M+H]$^+$ 282.1279.

Alkynyl folic acid (11)[49,50]*:* Folic Acid (485mg, 1.1mmol) was dissolved in DMF (10ml) and cooled in a water/ice bath. N-Hydroxysuccinimide (144mg, 1.25mmol) and EDC (240mg, 1.25mmol) were added, and the resulting mixture was stirred in an ice bath for 30 min. A solution of propargylamine (72μl, 1.125mmol) in DMF (5.0ml) was added, and the resulting mixture was allowed to warm to room temperature and stirred for 24h. The reaction mixture was poured into water (100ml) and stirred for 30min to form a precipitate. The orange-yellow precipitate was filtered, washed with acetone, and dried under vacuum to give a product in 86% yield. ^{1}H NMR δ_H(d$_6$-DMSO) 8.64(s, 1H), 8.24-8.21(m, 1H), 7.95(m, 1H), 7.67-7.67 (t, 2H), 6.87(s, 2H), 6.65-6.63(d, 2H), 4.49-4.48(d, 2H), 4.32-4.30(m, 1H), 3.84-3.81(m, 2H), 3.03-3.01(t, 1H), 2.89(s, 1H), 2.73(s, 1H), 2.31-2.20 (m, 2H), 1.98-1.96 (m, 1H), 1.87-1.85(m, 1H).

C.3.2 Functionalization of ZnO/MgZnO Nanorod Films Surface

The click reaction on the ZnO/MgZnO nanorod surface was performed by the "droplet method", as previously reported.[29] Briefly, this method involved immersing the film in a small volume of the indicated solution (2-3 ml) in a sealed vial. After reacting for the indicated period of the time, the films were thoroughly rinsed with neat solvent and dried under gentle nitrogen flow. The films were stored for days in the dark without apparent change of their FTIR-ATR spectra.

Formation of Bifunctional Linker Layer (Step A). The ZnO nanorods film was reacted using the droplet method[25] with 10 mM 11-azidodecanoic acid solution in 1-butanol/ethanol 2/1 for 12-15 h, then rinsed thoroughly with neat solvent and dried under nitrogen flow.

Cu-free Click reaction with 1-ethynylpyrene (Scheme C.4, Step B). The functionalized ZnO nanorod film from Step A was placed in a sealed vial with 1-ethynylpyrene (3 ml of a 45 mM THF solution), then the solution was heated at 50 $^{\circ}$C for 5.5 h. The reaction was monitored by FTIR-ATR of the film (disappearance of the N_3 band at 2100 cm^{-1}). Then the film was rinsed thoroughly with neat solvent and dried under nitrogen flow.

Cu-free Click reaction with alyknated biotin (Scheme C.5, Step C). The functionalized ZnO film from Step A was immersed in a vial of alkynated biotin solution (3 ml of a 10 mM DMF solution) at room temperature for 1.5 h. The completion of

reaction was monitored by FTIR-ATR (disappearance of the azide band at 2100 cm^{-1}). Then the film was rinsed thoroughly with neat solvent and dried under nitrogen flow.

Binding of Streptavidin-FITC (Scheme C.5, Step D). The biotin-modified ZnO Film was incubated[23] for 2 h at 4 $^{\circ}$C into freshly prepared 1 mg/ml streptavidin solution in 10 mM PBS buffer filtered through a 0.2 µm polytetrafluoroethylene (PTFE) filter. Then the film was rinsed thoroughly with PBS buffer and dried under nitrogen flow.

Cu-free Click reaction with alyknal folic acid (Scheme C.6, Step E). The functionalized ZnO film from Step A was immersed in a vial of alkynated folic acid solution (3 ml of a 10 mM DMF solution) at room temperature for 1.5 h. The completion of reaction was monitored by FTIR-ATR (disappearance of the azide band at 2100 cm^{-1}). Then the film was rinsed thoroughly with neat solvent and dried under nitrogen flow.

C.4 Conclusion

We have demonstrated that ZnO or MgZnO nanorod films can be functionalized by a stepwise strategy involving Cu-free click chemistry. A long chain saturated carboxylic acid capped with an azide end group was bound to the ZnO/MgZnO nanorod surface through the COOH moiety, leaving the N$_3$ group available for click reaction with an alkyne.   Three types of alkyne derivatives were reacted with the functionalized ZnO/MgZnO films through copper-free click reaction: 1-ethynypyrene, a fluorescent probe, alkynated biotin and alkynyl folic acid. The biotin-immobilized films bind successfully with streptavidin. The advantages of Cu-free click chemistry include mild reaction conditions, the ability to perform in the absence of Cu(I) or Cu(0) byproduct, and

enabling surface immobilization of biomolecules on ZnO/MgZnO nanorods. The application of this methodology to nano-biosensors, including quartz crystal microbalances is in progress. The development of the sensors will allow probing the mass loading (surface coverage) obtained by the method described here. The data obtained with the pyrene probe and the streptavidin-FITC, however, suggest that the molecules and biomolecules anchored thorugh the click method are not tightly or uniformly packed on the surface of the semiconductor.

C.5 References

(1)   Taratula, O.; Galoppini, E.; Mendelsohn, R.; Reyes, P. I.; Zhang, Z.; Duan, Z.; Zhong, J.; Lu, Y. *Langmuir : the ACS journal of surfaces and colloids* **2009**, *25*, 2107.

(2)   Lummerstorfer, T.; Hoffmann, H. *The Journal of Physical Chemistry B* **2004**, *108*, 3963.

(3)   Toulemon, D.; Pichon, B. P.; Cattoën, X.; Man, M. W. C.; Begin-Colin, S. *Chemical Communications* **2011**, *47*, 11954.

(4)   Devaraj, N. K.; Collman, J. P. *QSAR & Combinatorial Science* **2007**, *26*, 1253.

(5)   Bishop, L. M.; Yeager, J. C.; Chen, X.; Wheeler, J. N.; Torelli, M. D.; Benson, M. C.; Burke, S. D.; Pedersen, J. A.; Hamers, R. J. *Langmuir : the ACS journal of surfaces and colloids* **2012**, *28*, 1322.

(6)   Kolb, H. C.; Finn, M. G.; Sharpless, K. B. *Angewandte Chemie International Edition* **2001**, *40*, 2004.

(7)   Kolb, H. C.; Sharpless, K. B. *Drug Discovery Today* **2003**, *8*, 1128.

(8)   *Proceedings of the Chemical Society* **1961**, 357.

(9)   Rusmini, F.; Zhong, Z.; Feijen, J. *Biomacromolecules* **2007**, *8*, 1775.

(10)   Himo, F.; Lovell, T.; Hilgraf, R.; Rostovtsev, V. V.; Noodleman, L.; Sharpless, K. B.; Fokin, V. V. *Journal of the American Chemical Society* **2004**, *127*, 210.

(11)   Wang, T. and Guo, Z.J. (2006), Copper in medicine: homeostasis, chelation therapy and anitumor drug design, Current Medical Chemistry, 13, 525-537.

(12)   Sletten, E. M.; Bertozzi, C. R. *Angewandte Chemie International Edition* **2009**, *48*, 6974.

(13)   Baskin, J. M.; Prescher, J. A.; Laughlin, S. T.; Agard, N. J.; Chang, P. V.; Miller, I. A.; Lo, A.; Codelli, J. A.; Bertozzi, C. R. *Proceedings of the National Academy of Sciences* **2007**, *104*, 16793.

(14)   Li, Z.; Seo, T. S.; Ju, J. *Tetrahedron Letters* **2004**, *45*, 3143.

(15)   Lummerstorfer, T.; Hoffmann, H. *The Journal of Physical Chemistry B* **2004**, *108*, 3963.

(16)   Imanishi, A.; Yamane, S.; Nakato, Y. *Langmuir : the ACS journal of surfaces and colloids* **2008**, *24*, 10755.

(17)   Boren, B. C.; Narayan, S.; Rasmussen, L. K.; Zhang, L.; Zhao, H.; Lin, Z.; Jia, G.; Fokin, V. V. *Journal of the American Chemical Society* **2008**, *130*, 8923.

(18)   Based on Web of Science.

(19)   Rostovtsev, V. V.; Green, L. G.; Fokin, V. V.; Sharpless, K. B. *Angewandte Chemie International Edition* **2002**, *41*, 2596.

(20)   Collman, J. P.; Devaraj, N. K.; Eberspacher, T. P. A.; Chidsey, C. E. D. *Langmuir : the ACS journal of surfaces and colloids* **2006**, *22*, 2457.

(21)   Benson, M. C.; Ruther, R. E.; Gerken, J. B.; Rigsby, M. L.; Bishop, L. M.; Tan, Y.; Stahl, S. S.; Hamers, R. J. *ACS applied materials & interfaces* **2011**, *3*, 3110.

(22)   Haensch, C.; Hoeppener, S.; Schubert, U. S. *Nanotechnology* **2008**, *19*, 035703.

(23)   Sun, X. L.; Stabler, C. L.; Cazalis, C. S.; Chaikof, E. L. *Bioconjugate chemistry* **2006**, *17*, 52.

(24)   Hayashi, K.; Moriya, M.; Sakamoto, W.; Yogo, T. *Chemistry of Materials* **2009**, *21*, 1318.

(25)   Santos, C. M.; Kumar, A.; Zhang, W.; Cai, C. *Chemical Communications* **2009**, 2854.

(26)   Bolley, J.; Guenin, E.; Lievre, N.; Lecouvey, M.; Soussan, M.; Lalatonne, Y.; Motte, L. *Langmuir : the ACS journal of surfaces and colloids* **2013**, *29*, 14639.

(27)   Limapichat, W.; Basu, A. *Journal of Colloid and Interface Science* **2008**, *318*, 140.

(28)   Henriksson, A.; Friedbacher, G.; Hoffmann, H. *Langmuir : the ACS journal of surfaces and colloids* **2011**, *27*, 7345.

(29)   Cao, Y.; Galoppini, E.; Reyes, P. I.; Duan, Z.; Lu, Y. *Langmuir : the ACS journal of surfaces and colloids* **2012**, *28*, 7947.

(30)   Manova, R. K.; Pujari, S. P.; Weijers, C. A. G. M.; Zuilhof, H.; van Beek, T. A. *Langmuir : the ACS journal of surfaces and colloids* **2012**, *28*, 8651.

(31)   Baskin, J. M.; Bertozzi, C. R. In *Click Chemistry for Biotechnology and Materials Science*; John Wiley & Sons, Ltd: 2009, p 29.

(32)   Reyes, P. I.; Zhang, Z.; Chen, H. H.; Duan, Z. Q.; Zhong, J.; Saraf, G.; Lu, Y. C.; Taratula, O.; Galoppini, E.; Boustany, N. N. *Ieee Sens J* **2009**, *9*, 1302.

(33)   Cao, Y.; Galoppini, E.; Reyes, P. I.; Lu, Y. *Langmuir : the ACS journal of surfaces and colloids* **2013**, *29*, 7768.

(34)   Sudimack, J.; Lee, R. J. *Advanced Drug Delivery Reviews* **2000**, *41*, 147.

(35)   Wu, Z.; Li, X.; Hou, C.; Qian, Y. *Journal of Chemical & Engineering Data* **2010**, *55*, 3958.

(36)   Rivera, E.; Belletete, M.; Zhu, X. X.; Durocher, G.; Giasson, R. *Polymer* **2002**, *43*, 5059.

(37)   Gibson, S. E.; Jones, J. O.; Kalindjian, S. B.; Knight, J. D.; Mainolfi, N.; Rudd, M.; Steed, J. W.; Tozer, M. J.; Wright, P. T. *Tetrahedron* **2004**, *60*, 6945.

(38)   Sun, S.; Wu, P. *The journal of physical chemistry. A* **2010**, *114*, 8331.

(39)   Romero, T.; Caballero, A.; Tarraga, A.; Molina, P. *Organic letters* **2009**, *11*, 3466.

(40)   Theodorou, V.; Skobridis, K.; Tzakos, A. G.; Ragoussis, V. *Tetrahedron Lett* **2007**, *48*, 8230.

(41)   Thyagarajan, S.; Galoppini, E.; Persson, P.; Giaimuccio, J. M.; Meyer, G. J. *Langmuir* **2009**, *25*, 9219.

(42)   Taratula, O.; Galoppini, E.; Wang, D.; Chu, D.; Zhang, Z.; Chen, H.; Saraf, G.; Lu, Y. *The journal of physical chemistry. B* **2006**, *110*, 6506.

(43)   Holmberg, A.; Blomstergren, A.; Nord, O.; Lukacs, M.; Lundeberg, J.; Uhlen, M. *Electrophoresis* **2005**, *26*, 501.

(44)   Lieber, E.; Rao, C. N. R.; Chao, T. S.; Hoffman, C. W. W. *Anal. Chem.* **1957**, *29*, 916.

(45)   Mittal, R.; Bruchez, M. P. *Bioconjugate chemistry* **2011**, *22*, 362.

(46)   Pähler, A.; Hendrickson, W. A.; Kolks, M. A.; Argaraña, C. E.; Cantor, C. R. *J. Biol. Chem.* **1987**, *262*, 13933.

(47)   Ross, T. L.; Honer, M.; Lam, P. Y. H.; Mindt, T. L.; Groehn, V.; Schibli, R.; Schubiger, P. A.; Ametamey, S. M. *Bioconjugate Chemistry* **2008**, *19*, 2462.

(48)   Wang, X.; Liu, L.; Luo, Y.; Zhao, H. *Langmuir : the ACS journal of surfaces and colloids* **2009**, *25*, 744.

(49)   Saeed, A. O.; Magnusson, J. P.; Moradi, E.; Soliman, M.; Wang, W.; Stolnik, S.; Thurecht, K. J.; Howdle, S. M.; Alexander, C. *Bioconjugate Chemistry* **2011**, *22*, 156.

(50)   Das, M.; Bandyopadhyay, D.; Mishra, D.; Datir, S.; Dhak, P.; Jain, S.; Maiti, T. K.; Basak, A.; Pramanik, P. *Bioconjugate chemistry* **2011**, *22*, 1181.

Chapter D

Studies of Pyrene@CB[8] on Metal Oxide Surfaces

D.1 Pyrene

Fluorescent probes are useful in investigations of many aspects of chemistry and biochemistry. For example, to study their conformations and interactions, in nonradioactive detection and visualization modes.[1] Among the available fluorophores, pyrene and its derivatives have long been attractive by virtue of their inherent chemical and photochemical characteristics. Pyrene is a polycyclic aromatic hydrocarbon consisting of four fused benzene rings, resulting in a planar aromatic system. Pyrene and its derivatives have high fluorescence quantum yield (0.99 in acetone, 0.62 in acetonitrile and 0.75 in methanol).[2,3] _ENREF_2 Indeed, pyrene fluorophores have excimer formation in their systems and their rather long fluorescence lifetimes (hundreds of ns),[4] which have prompted researchers to explore various applications, such as surface coverage studies and the development of novel strategies for detecting DNA and RNA.[5] In this section, two unique spectral features of the fluorescence emission spectra are exploited to obtain information regarding pyrene-complex systems, such as molecular organization.

Pyrene Value: The first notable spectral feature of pyrene is the sensitivity to the microenvironment.[6] The fluorescence emission spectrum of pyrene shows five major vibronic bands (Bands I, II, III, IV and V) along with well-defined peaks at ~ 375, 379, 385 and 410 nm respectively (Figure D.1, left).[7] When compared with the emission intensity of Band I at 375nm, which is assigned to the first vibronic band, the intensity of Band III at 385 nm assigned to the third vibronic band is significantly enhanced in a hydrophobic environment. In contrast, the intensity of Band I is significantly higher than

that of Band III in polar environments.[8] Narayanaswami and co-workers have demonstrated this feature of pyrene by comparing the emission spectra of pyrene in hexane (Figure D 1, left) and dimethylsulfoxide (DMSO) (Figure D 1, right).[9] Hexane has low dielectric constant of ~ 4.8 and is a nonpolar solvent. DMSO has high dielectric constant of ~ 47.2 and dipole moment of 3.96 D so it is a relatively polar solvent. In hexane, pyrene displays a dominant Band III relative to Band I, while in DMSO, Band I is dominant compared to Band III. The reasons for this observation have been attributed to excited state interaction of the molecule with the surrounding solvent, as well as solvent reorientation around the excited state dipole.[10]

Pyrene in Hexane   Pyrene in DMSO
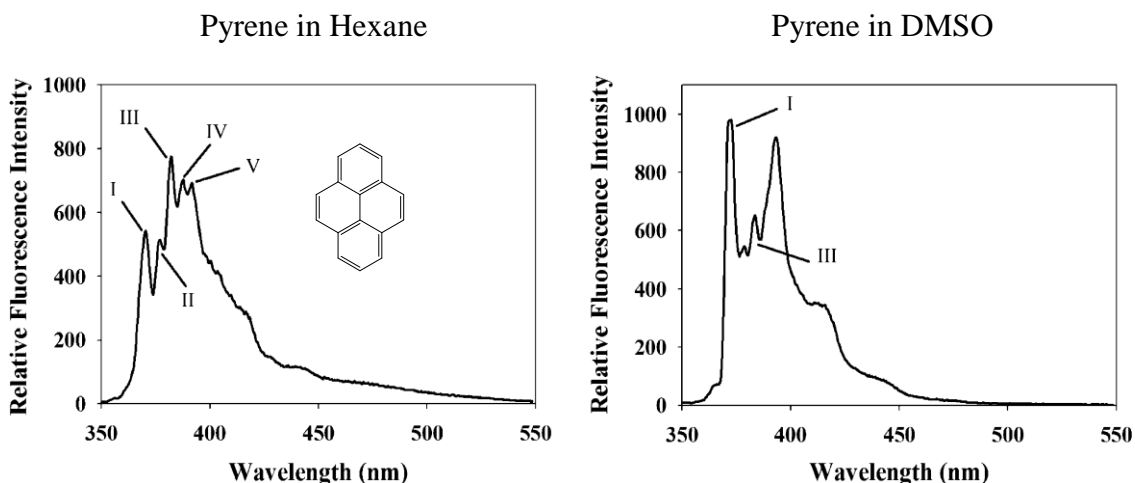
Figure D 1 Pyrene fluorescence emission is sensitive to solvent polarity. Arrows point to Bands I, II, III, IV, and V for the spectrum in hexane. Only Bands I and III are shown for DMSO (taken from reference 10).

The ratio of the fluorescence emission intensities of Band I/II has been extensively used to characterize the environment of pyrene when included in microheterogeneous systems. Bohne and coworkers have used this property to study the complexation of pyrene with cyclodextrin host-guest systems through steady-state fluorescence experiments.[11] In addition, singlet excited pyrene in the presence of ground-state pyrene

forms an excimer, which commonly shows a broad emission centered at about ~ 460nm and is red-shifted from the monomer emission. As illustrated in Figure D 2, in the presence of cyclodextrin as an organic host with different concentrations, monomer and excimer emissions of pyrene were observed. In water, pyrene monomer emission had a high I/III emission-intensity ratio.[12] With increasing cyclodextrin concentrations, the monomer emission intensities as well as the I/III ratios changed. By analysis of these observed changes of ratios, it was determined that the complexation mode of Pyrene@cyclodextrin is as 1:1, 1:2 or 2:2 complexes, depending on the concentration.
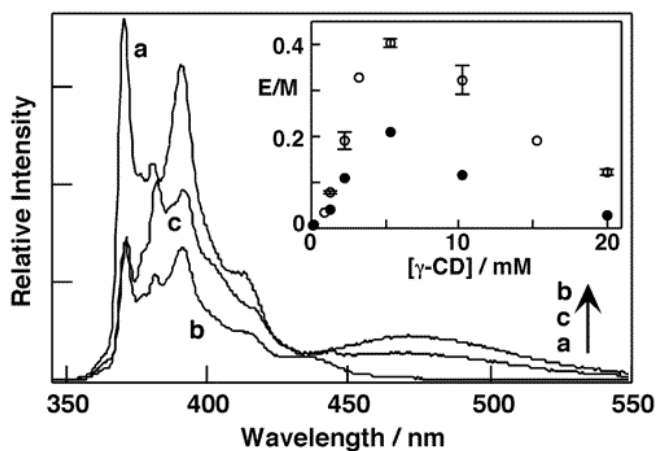
Figure D 2 Fluorescence spectra for pyrene (0.5 μM) in (a) water and in the presence of (b) 5 mM and (c) 20 mM γ-CD. The inset shows the dependence of the intensity ratio for the excimer (473 nm) and monomer (383 nm) (E/M) emissions for 0.5 μM and 0.25 μM pyrene on the γ-CD concentration (taken from reference 12).

Excimer Emission: The second notable feature of pyrene fluorescence emission is the excimer formation, which appears to be a broad, unstructured, and significantly red-shifted band (ranging from 425 to 550 nm, commonly centered on 460 nm). The exicmer formation occurrs when two pyrene units are < 10 Å from each other. The mechanism of pyrene excimer emission was described by Lehrer and coworkers.[13] A

scheme simplified from Lehrer[13] is shown below to describe the process of pyrene fluorescence emission. Excitation of a ground state monomer (M) gives rise to an excited state monomer (M*), which decays and results in the monomer emission spectrum. Then, M interacts with a spatially proximal M to yield M·M, one of the possibilities is that M·M is in a precise orientation to create excitation (M·M*) and lead to excimer formation (E*) (Equation 1).

$$M \longrightarrow M^* \longrightarrow M + h\upsilon_M \quad \text{(momomer emission)} \qquad\qquad \text{Eq 1}$$

$$M + M \longrightarrow M\cdot M \longrightarrow M\cdot M^* \longrightarrow E^* \longrightarrow M\cdot M + h\upsilon_E \text{ (excimer emission)}^7$$
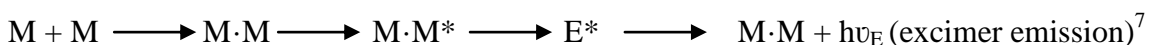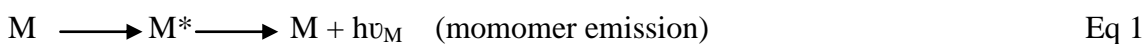
Several research groups have observed excimer formation on functionalization of various surfaces with pyrene moieties. Fang and co-workers have proposed a pyrene-functionalized fluorescent film for sensing nitroaromatic compounds, as illustrated in Figure D 3(a). The steady-state fluorescence emission showed the composed of two sharp peaks at wavelengths of 380 nm and 401 nm, and one broad band centered at 500nm (Figure D 3(b)).[14]
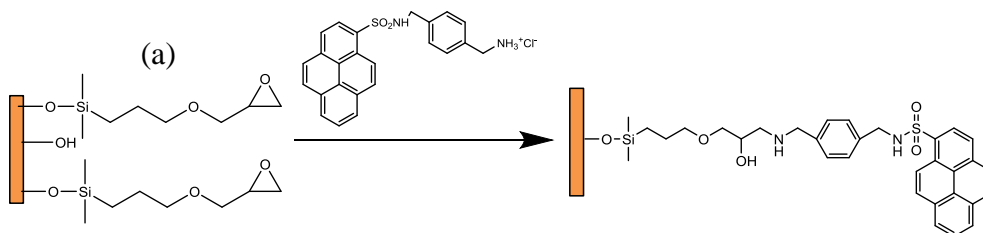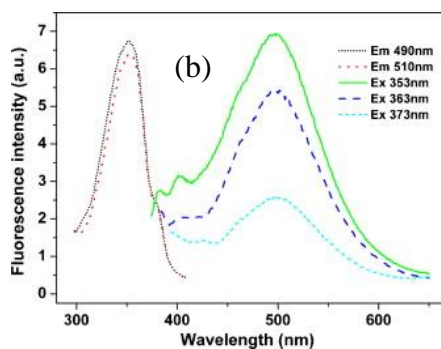
Figure D 3 (a) Schematic representation of immobilization of pyrene as fluorophore onto a glass plate surface. (b) Fluorescence excitation and emission spectra of the film in aqueous solution (taken from reference 14).

Analysis of the excitation and absorption spectra of pyrene-modified semiconductor surfaces was used to obtain information on surface coverage.[15] Excimer formation on the surface suggests that the pyrene molecules pack closely with high surface coverage. In previous studies by our group, a series of pyrene chromophores were synthesized to bind to the semiconductor surface through tripodal (1) or rigid-rod (2) linkers, as illustrated below. The absorption and fluorescence spectra of **1** and **3** on a sapphire substrate are shown in Figure D 4.[15]

The data collected for 1 showed the broad, featureless, and significantly red-shifted band assigned to excimer formation when compared with that of **3** in solution. This suggested that the rod-like pyrene chromophore **1** aggregates on the surface. Compared with **1**, the fluorescence spectrum of **3** on sapphire (a planar surface) was similar to that of **1** in solution, with no indication of excimer emission. By studying formation of excimer in the fluorescence spectra, we demonstrated that by increasing the size of the footprint for an anchor group, aggregation of pyrene chromophore molecules was reduced on planar surfaces.
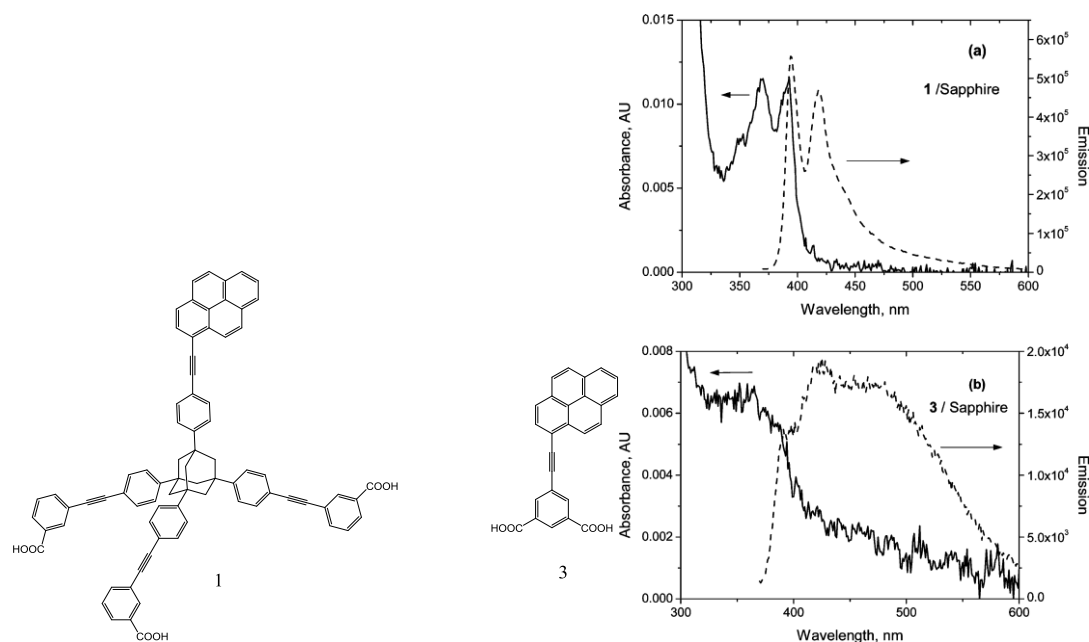
Figure D 4 Absorbance (solid line) and fluorescence (dashed line) spectra of tripod 1 (a) and pyrene-Ipa-rod 3 (b) anchored to a planar sapphire substrate; λexc= 355 nm (taken from reference 15).

D.2 Results and Discussion

In the study of the functionalization of ZnO nanorod films (refer to Chapter B) with 1-ethynylpyrene through click chemistry, predominance of the excimer emission band was observed. This observation suggests that pyrene units come in close contact (<3.5 Å) on the ZnO nanorod surface,[16] and a highly inhomogeneous emission intensity distribution was noticed, which could be a result of a disordered layer.[17]

In this chapter, we proposed an organic host-guest system by using cucurbit[8]uril as host molecules to encapsulate pyrene-**7** as a pyrene-based fluorophore to improve the binding orientation on metal oxide films, as illustrated in Scheme D 1. The reason to use

cucurbit[8]uril is that it exhibits high complexation affinity for pyrene in aqueous media.[18]

5-(4-(pyren-1-ylethynyl)phenyl)pentanoic acid

pyrene-7

Cucurbit[8]uril

CB[8]

MO_n

MO_n
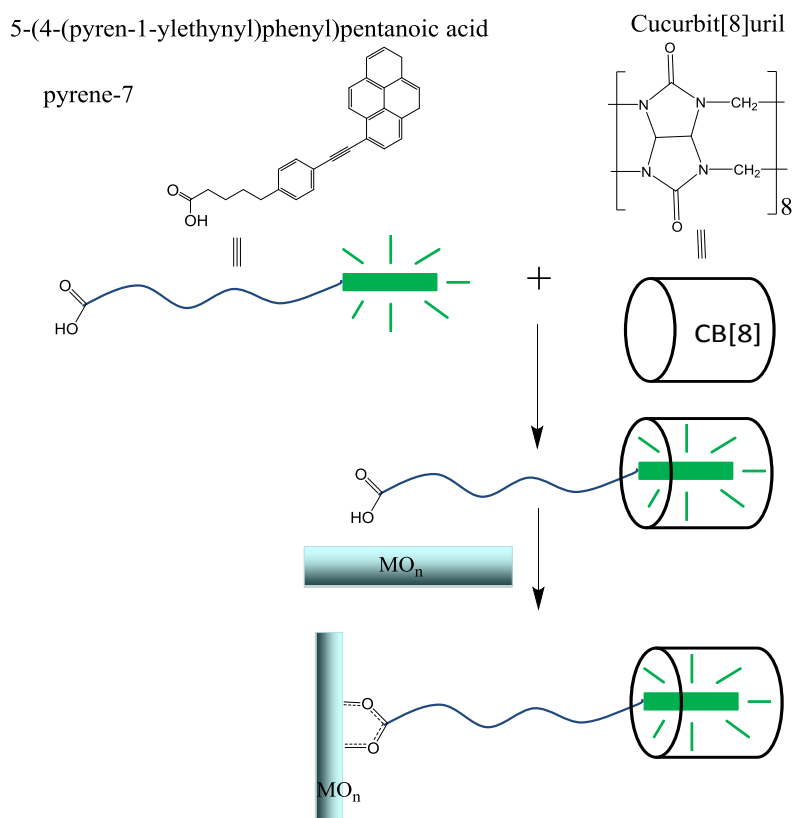
Scheme D 1 pyrene-**7**@CB8 complexation system on MOn surfaces

The surface binding orientation was investigated by fluorescence emission spectra by comparing the only pyrene-based fluorophores and pyrene-**7**@CB8 complexes on TiO_2 and ZrO_2 surfaces.

D.2.1 Synthesis

The synthesis of pyrene-**7** is illustrated in Scheme D 2. The first step was iodination, introducing an iodine group on the pyrene framework.[19] The second step was Fisher esterification of 5-(4-Iodophenyl)pentanoic acid **2** to increase the solubility.[19] The synthesis of methyl 5-(4-ethynylphenyl)pentanoate **5** was achieved through Sonogashira

coupling with trimethylsilylacetylene followed by deprotection with TBAF.[20] Methyl 5-(4-(pyren-1-ylethynyl)phenyl)pentanoate **6** was also synthesized through Sonogashira coupling with 1-iodopyrene.[19] The final step was hydrolysis of the ester group.[21]
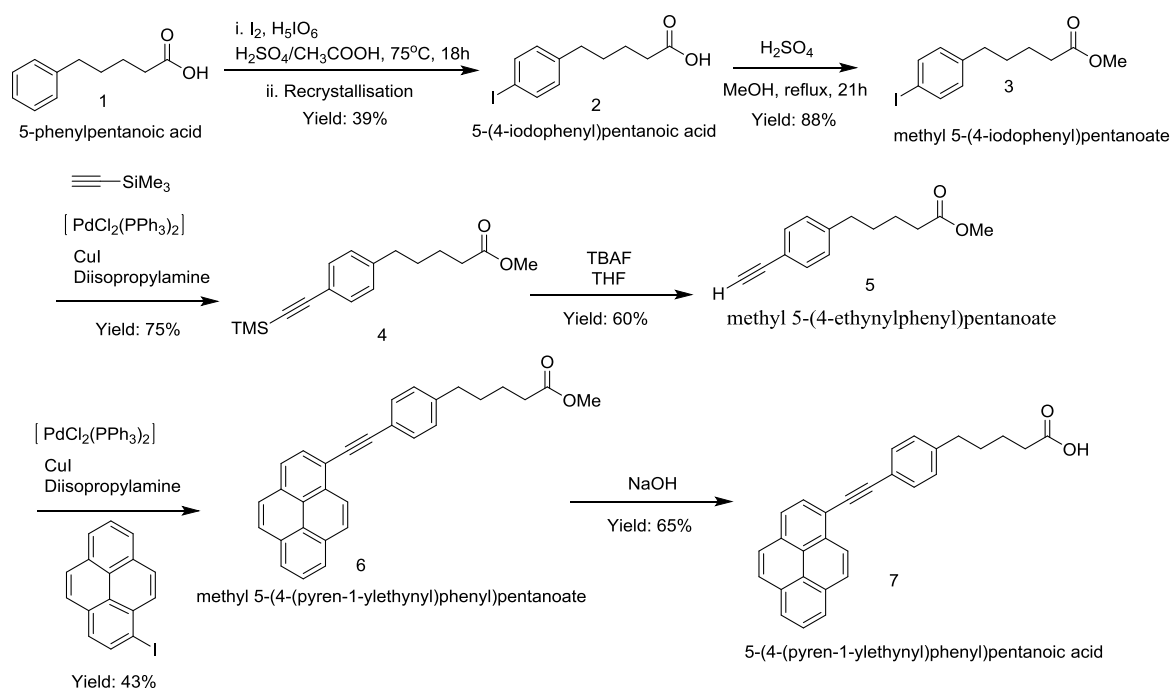
Scheme D 2 Synthesis of pyrene-7 (7)

D.2.2 Photophysical Studies of pyrene-7 as Pyrene-based Chromophore

The absorption maxima of pyrene-**7** in dichloromethane (red line in Figure D 5) was shifted to longer wavelengths (λ_{max}=378 nm)compared with non-substituted pyrene (black line in Figure D 5) by introducing the phenylethynyl unit. This modification was necessary in order to selectively photoexcite pyrene-**7** to study the emission and absorption on the surface of TiO_2 ($\lambda_{abs} < 400$ nm).
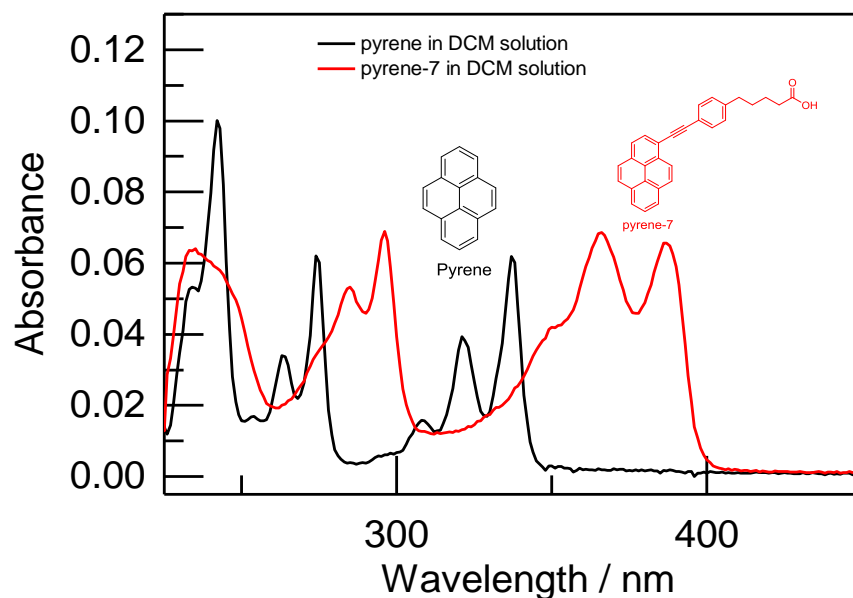
Figure D 5 UV-visible absorption spectra of pyrene-**7** and pyrene in dichloromethane.

The fluorescence maxima of pyrene-**7** in dichloromethane (Figure D 6, left) is observed at the longer wavelengths compared with non-substituted pyrene (Figure D 6, right).
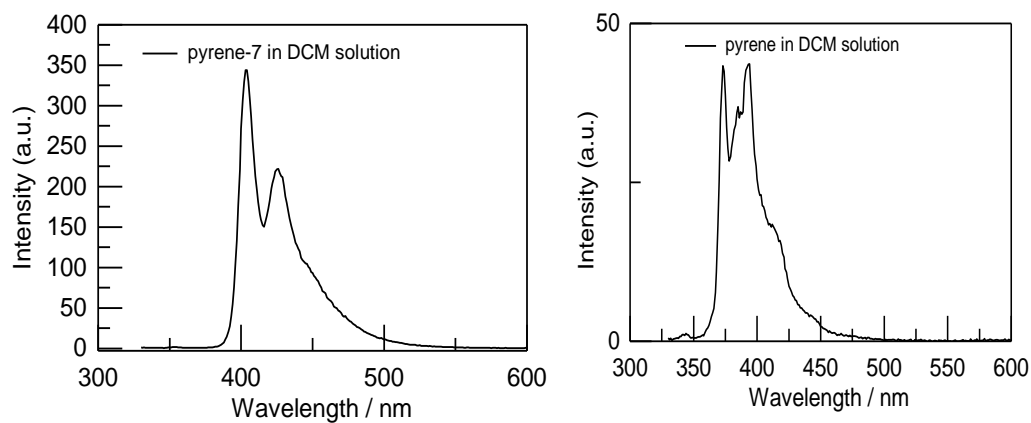
Figure D 6 Fluorescence emission spectra of pyrene-**7** (λ_{exc}=378nm) and pyrene (λ_{exc}=311nm) in dichloromethane.

Fluorescence quantum yields (Φ) were calculated based on the equation (1): [22]

$$\Phi_{sample} = \left(\frac{A_{ref}}{A_{sample}} \times \frac{I_{sample}}{I_{ref}} \right) \Phi_{ref}$$ **Eq. 1**

The subscript '*ref*' refers to the reference. *A* is the absorbance at the excitation wavelength. *I* is the integrated emission area. The fluorescence quantum yields of pyrene-**7** were determined in a dichloromethane solution using pyrene as the reference.[23,3] Table D-1 shows the results of the quantum yield calculations.

Table D - 1 Fluorescence Quantum Yield

Compound	λ_{ex} (nm)	$\Phi^{(a)}$ ± 0.01
pyrene	311	0.068
pyrene-**7**	378	0.6153

(a)   Pyrene was used as the reference with Φ= 0.068 in dichloromethane[23,3]

D.2.3 Determination of Complexation

The purpose of the solution study was to find the experimental conditions for encapsulation of pyrene-**7**@CB[8] in solutions, and then study the binding of the pyrene-**7**@CB[8] complexes on TiO_2 and ZrO_2 surfaces.

Determination of Actual Concentration of CB[8]. CB[8] was chosen to study host-guest system because of the relatively large cavity and facile preparation.[24] The actual concentration of CB[8] is necessary to determine the complexation of host-guest system.[25] However, CB[8] samples often contain various impurities, such as water from atmospheric moisture,[26] and hydrogen chloride, which is typically introduced in the

course of synthesis.[27]   The complete removal of impurities from CB[8] samples is difficult and time consuming.   The impurities are often relatively inert in host-guest binding studies, and their removal is not strictly necessary.[28]   However they prevent the determination of an accurate concentration.

Kaifer's group[29] has developed a simple and convenient method to determine the concentration of CB[8] samples by using absorption spectroscopy. This method is based on the formation of highly stable complexes between CB[8] and cobaltocenium (Cob^+), an organometallic cation easily obtainable in pure form, relatively cheap, and not hydroscopic.

In our experiment, 3.00 mL of cobaltocenium (Cob^+) aqueous solution, 2.3 μM calculated according to the Beer-Lambert Law, was placed in a 10mm × 10mm quartz cell. The absorbance peak of Cob^+ at 261nm was decreased and red-shifted upon titration with CB[8], which is shown in Figure D 7. Since Cob^+ is the UV-Vis active species, its concentration was maintained constant through the titration so that any absorbance changes were due to the formation of the less absorbing Cob^+ inclusion complex.
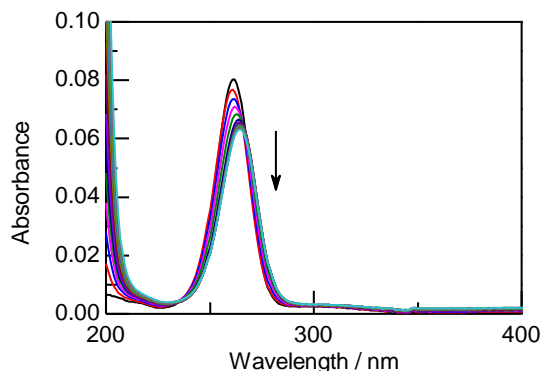
Figure D 7 Absorption spectra of Cob^+ (2.3 μM in pure water) in the presence of increasing CB[8] concentrations (0~9 μM in the direction of the arrow).

The red lines in Figure D 8 show the data fit to two straight lines. Since the binding affinities between Cob^+ and CB[8] are quite high, the intersection of two straight lines was employed to determine the concentration of 1.0 equiv of CB[8] based on the volume of CB[8] added at the endpoint(V_E), as illustrated in equation 2. The initial volume of Cob^+ (V_0) was 3.00 ml.
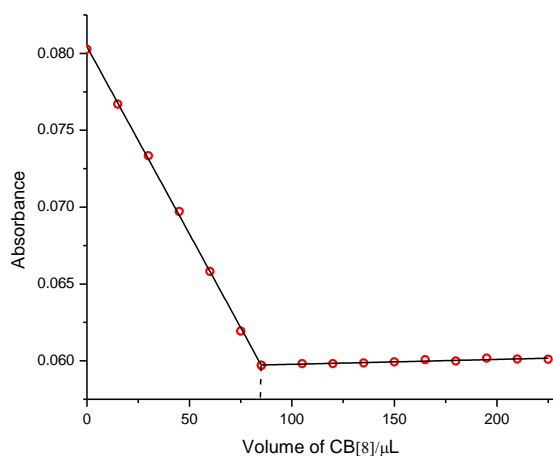
Figure D 8 Binding isotherm obtained by plotting the absorbance at 261nm against the volume of CB[8] added into Cob^+ aqueous solution.

$$[CB[8]]act = \frac{[Cob+] \times V_0}{V_E} \qquad \text{Eq. 2}$$

Determination of Complexation of pyrene-7@CB[8]. In our study, steady-state fluorescence spectra were used to investigate the complexation of pyrene-**7**@CB[8]. Several models (Model 1-3) were proposed based on the structure of pyrene-**7**@CB[8] complexes as shown below.

$$Py + CB \xrightleftharpoons{K_{11}} PyCB \quad (1)$$

$$PyCB + CB \xrightleftharpoons{K_{12}} PyCB_2 \quad (2)$$

$$PyCB_2 + CB \xrightleftharpoons{K_{13}} PyCB_3 \quad (3)$$
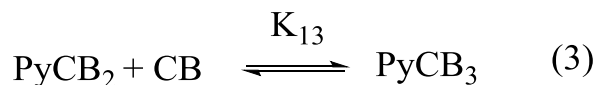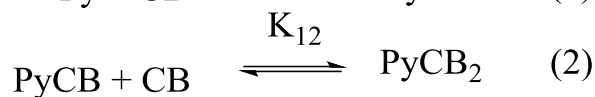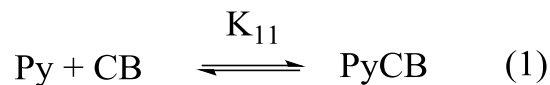
The pyrene emission shows vibronic structure and the ratio of the intensity of fluorescence emission spectra at 385 nm to the intensity at 395 nm (Figure D 9) is sensitive to the solvent polarity. This property has been extensively used to characterize the environment of pyrene when included in microheterogeneous systems.[8] The numerical fitting results showed in Figure D 10 experimentally proved that Model 1 is the right model for the complexation study in pyrene-**7**@CB[8] system. In summary, CB[8] only contain one pyrene-**7** molecule to form a 1:1 complex, and this result is consistent with studies reported previously for pyrene@CB[8].[18]
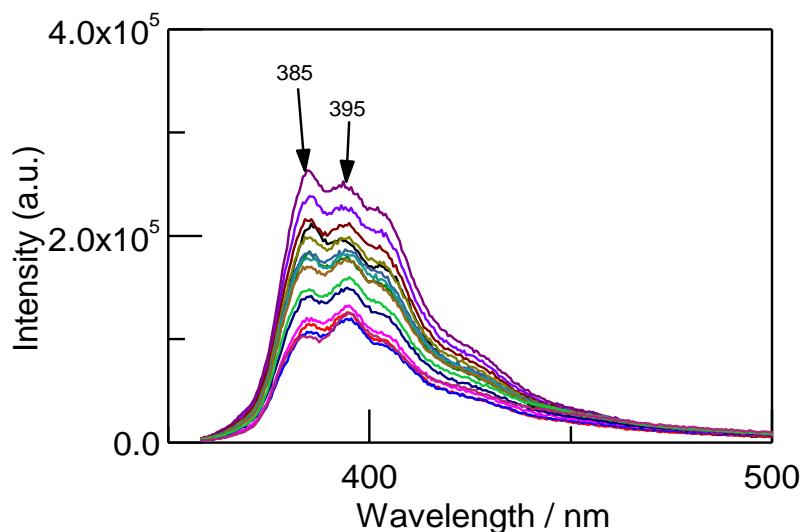
Figure D 9 Fluorescence emission spectra for pyrene (0.5 μM) in in the presence of CB[8].
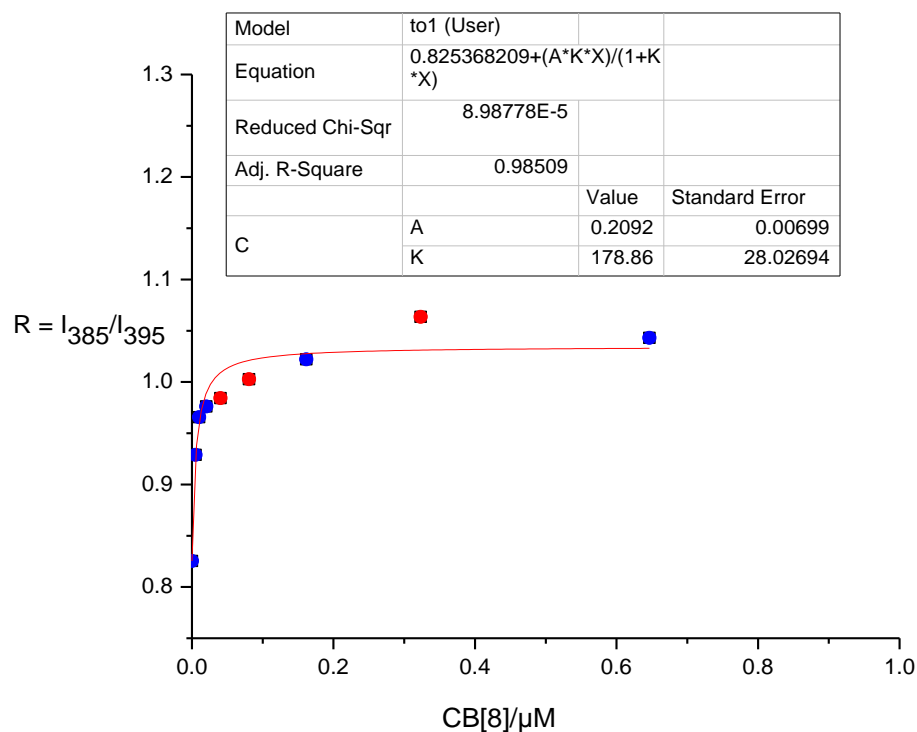
Figure D 10 Numerical fit of the [CB[8]] dependence of R (the ratio of intensity at 385 nm to 395 nm) to the 1:1 binding model.

D.2.3 Binding Study

ZrO_2 (Zirconium Dioxide) nanoparticles have a wide band gap given (5.0eV).[30, 31, 32] This property makes ZrO_2 an excellent substrate for steady state fluorescence studies of excited state chromophores on nanoparticle surfaces. The fluorescence emission of chromophores on ZrO_2 is not quenched.

Pyrene-7 bound to TiO_2 and ZrO_2. pyrene-**7** was bound to TiO_2 and ZrO_2 films by immersing the films in solution as described in Experimental Section. A weak absorption band at 350 nm on TiO_2 in Figure D 11(a) was observed for pyrene-**7** on TiO_2. Absorption band at 355 nm in Figure D 11(b) was observed for pyrene-**7** on ZrO_2. The

difference of absorption for binding on TiO_2 and ZrO_2 was due to difference surface coverages, which was difficult to control.
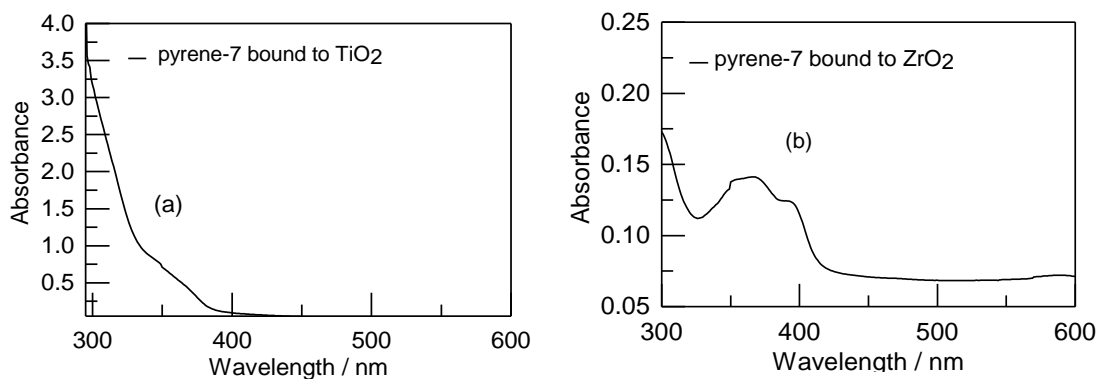
Figure D 11 UV-visible absorption spectra of (a) pyrene-**7** bound to TiO_2 and (b) pyrene-**7** bound to ZrO_2.

Compared to the spectral features of pyrene-**7** in solution showed in Figure D 6, the fluorescence emission spectrum of the film of pyrene-**7** on TiO_2 in Figure D 12(a) exhibited a broad, featureless, and centered band at 500 nm. The florescence emission spectrum of the film of pyrene-**7** on ZrO_2 in Figure D 12(b) had a broad and red-shifted band, but well-defined and higher intensity at 495 nm. These changes in the fluorescence spectrum are identical to the characteristic pyrene excimer emission. This pyrene excimer and close contacts could be the result of a disordered layer, where the pyrene moieties come in close proximity, consistent with our previous results.[33]
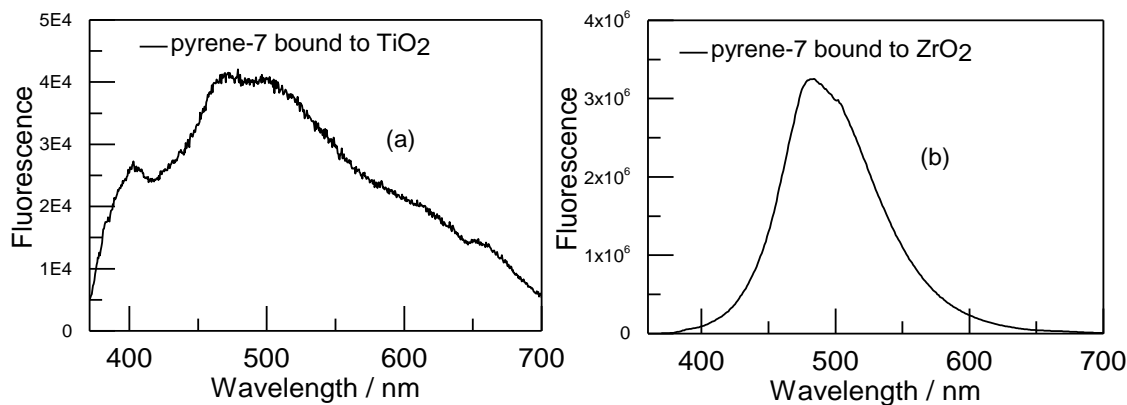
Figure D 12 Fluorescence Emission Spectra of (a) pyrene-**7** bound to TiO$_2$ (λ_{exc}=360 nm) (b) pyrene-**7** bound to ZrO$_2$ (λ_{exc}=364 nm).

Pyrene-7@CB[8] bound to TiO$_2$ and ZrO$_2$: Pyrene-**7**@CB[8] was bound to TiO$_2$ and ZrO$_2$ films by immersing the films in solution, as described in the Experimental Section.

Compared with the fluorescence emission spectra of pyrene-**7** bound to TiO$_2$ (Figure D 12, a), the presence of sharp monomer peak observed at 390 nm (Figure D 13) demonstrated decreased aggregation of pyrene units on surfaces. However, the broad and red-shifted peak was still present, which showed pyrene-**7**@CB[8] only could depress, but not completely prevent the formation of excimer. Similar results were collected for binding ZrO$_2$. Compared with the fluorescence emission spectra of pyrene-**7** bound to TiO$_2$ (Figure D 13), the observed sharp monomer peak at 390nm and significantly blue-shifted spectra (Figure D 14) demonstrated the ability to decrease aggregation of a chromophore on nanostructured surfaces.
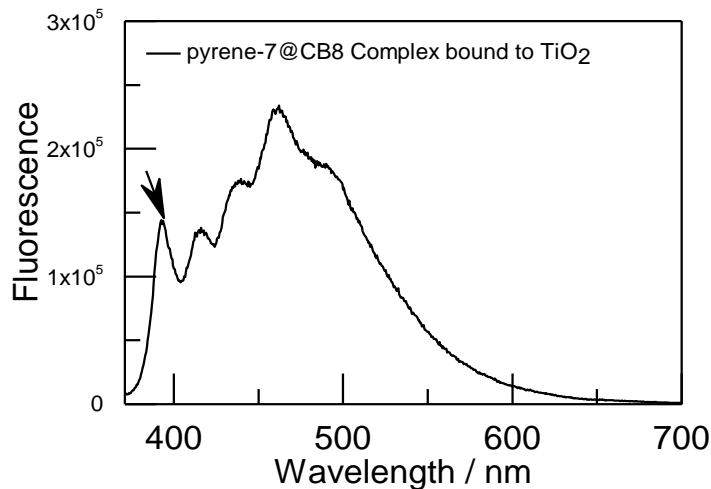
Figure D 13 Fluorescence Emission Spectra of pyrene-**7**@CB[8] Complex bound to TiO$_2$ (λ_{exc}=364 nm). Arrow points to monomer peak.
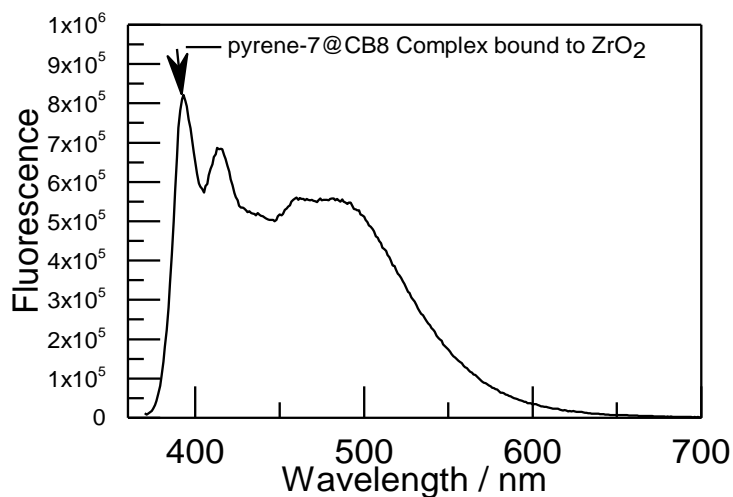
Figure D 14 Fluorescence Emission Spectra of pyrene-**7**@CB[8] Complex bound to ZrO$_2$ (λ_{exc}=364 nm). Arrow points to pyrene monomer peak.

In summary, by studying the emission spectra of only pyrene-**7** and pyrene-**7**@CB8 complex on metal oxide surfaces, we demonstrated the only pyrene-**7** on metal oxide surfaces formed the excimer of pyrene unit due to aggregation or disorder of bindng. With encapsulation of pyrene-**7** into CB[8] on surfaces, we were able to reduce the aggregation.

D.3 Experimental Section

General.

Materials: All reactions involving air- and moisture-sensitive reagents were performed under nitrogen atmosphere and in oven-dried or flame-dried glassware. Solvents and concentrated acids were purchased from Pharmco. Diisopropyl amine and dichloromethane were distilled over calcium hydride under N_2 atmosphere. THF was distilled with sodium and benzophenone while under N_2 atmosphere. Hexanes were distilled in air prior to use in column chromatography. 5-phenylpentanoic acid (Sigma-Aldrich), Iodine (Sigma-Aldrich), periodic acid (Sigma-Aldrich), CuI (Acros Organics), $PdCl_2(PPh_3)_2$ (Strem), Trimethylsilyl Acetylene (Alfa Aescar), TBAF (Tetrabutylammonium fluoride, 1.9 M solution in tetrahydrofuran) (Sigma-Aldrich), Isopropanol (Pharmco HPLC grade), methanol (Fisher HPLC grade), nitric acid (Fisher ACS grade), poly(ethyleneglycol) (PEG, av. Mol. Wt. 2000, Aldrich), titanium (IV) isopropoxide (Aldrich), Zirconium (IV) propoxide (70% in 1-propanol, Aldrich), Cucurbit[8]uril hydrate were used as received. The synthesis of 1-iodo-pyrene was previously reported.[33] Silica gel (230-400 mesh) was purchased from Sorbent Technologies. Deuterated NMR solvents were purchased from Cambridge Isotopes.

Methods: ^{1}H-NMR and ^{13}C-NMR spectra were collected on a Varian NMR spectrometer operating at 499.896 MHz for ^{1}H and 125.711 MHz for [13]C. Chemical shifts were reported relative to the central line of the solvent: $CDCl_3$ (δ 7.27 ppm) for ^{1}H spectra and $CDCl_3$ (δ 77.27 ppm) for ^{13}C spectra, and coupling constants (*J*) are reported

in Hz. Single attenuated total reflectance infrared (FTIR-ATR) spectra were performed on a Thermo Electron Corporation Nicolet 6700 FT-IR (ZnSe Crystal, number of spectra averaged 128, resolution 4 cm^{-1}). Steady-state fluorescence spectra were acquired and recorded at room temperature on a VARIAN CARY-Eclipse. UV-vis absorbance spectra were collected at room temperature on a Varian Cary 500 spectrophotometer. The films were placed diagonally at a 45° angle in a 1 cm cuvette in air while recording the spectra.

D.3.1 Synthesis

Synthesis of 5-(4-Iodophenyl)pentanoic acid (2):[19] The reaction flask was charged with 5-phenylpentanoic acid (8.0 g, 44.89 mmol, 1.0 equiv), periodic acid (2.05 g, 8.89mmol, 0.2 equiv), and iodine (4.56 g, 18.0 mmol, 0.4 equiv). A solution of 10M sulfuric acid (1.5 mL) and glacial acetic acid (48 mL) in distilled water (10 mL) was added. The reaction was heated at 75 °C for overnight under an atmosphere of nitrogen. The reaction flask was allowed to cool to room temperature, distilled water (100 mL) was added, and the resulting precipitate was collected on a sintered funnel and dissolved in CH_2Cl_2 (100 mL). The solution was washed with distilled water and saturated aqueous sodium thiosulfate. The organic layer was dried (sodium sulfate) and concentrated *in vacuo* to afford a white solid. Purification via crystallization from Hexane-Chloroform afforded compound **2** as white powder (4.3 g, 31%). ^{1}H NMR δ_H(CDCl$_3$) 7.61-7.59 (2H, d, $J = 8.05$), 6.95-6.93 (2 H, d, $J = 8.05$), 2.59 (2 H, s), 2.38 (2 H, s), 1.66 (4 H, s).

Synthesis of Methyl 5-(4-iodophenyl) pentanoate (3)[19]: To a stirring solution of 5-(4-iodophenyl)-pentanoic acid (1.22 g, 4 mmol) in methanol (6 ml), was added concentrated H_2SO_4 (0.26 ml). The solution was refluxed at 70 $^{\circ}$C for 21h under an atmosphere of nitrogen, then diluted with CH_2Cl_2 (50 ml) and extracted with water (2×25 ml), saturated aqueous sodium bicarbonate (2×25 ml) and brine (2×25 ml). The organic layer was dried over sodium sulfate and evaporated in vacuum to afford product 3, as pale yellow oil (0.829 g, 88% yield). ^1H NMR δ_H(CDCl$_3$) 7.60-7.58 (2H, d, J = 8.20), 6.94-6.92 (2 H, d, J = 8.20), 3.66 (3H, s), 2.57 (2 H, t, J = 7.25), 2.33 (2 H, t, J = 6.85), 1.66 (4 H, s); ^{13}C NMR δ_c (CDCl$_3$) 173.90, 141.73, 137.36, 130.57, 90.88, 51.57, 35.09, 33.87, 30.68, 24.28.

Synthesis of Methyl-5-(4-((trimethylsillyl)ethynyl)phenyl)pentanoate (4)[20]:

To a stirring solution of 3 (0.809 g, 2.54 mmol, 1 equiv) in fresh distilled diisopropylamine (58ml, 23ml/mmol), PdCl$_2$(PPh$_3$)$_2$ (178 mg, 0.254 mmol, 0.1 equiv) and CuI (96.87 mg, 0.51 mmol, 0.2 equiv) were added under nitrogen atmosphere. After 10 min, trimethylsilylacetylene (3.22 ml, 22.86 mmol, and 9 equiv) was added and the reaction mixture was stirred at 45°C for overnight. The dark crude product was purified by flash chromatography on a silica gel column by eluting with hexanes/ethyl acetate (9:1) to afford a dark orange oil (0.6883 g, 97% yield) after dry under vacuum. ^1H NMR (δ_H CDCl$_3$) δ 7.39-7.37 (2 H, d, J = 8.0), 7.11-7.09 (2 H, d, J = 7.95), 3.66 (3 H, S), 2.62 (2 H, s), 2.33 (2 H, s), 1.64 (4 H, s), 0.25 (9 H, s); ^{13}C NMR δ_c (CDCl$_3$) 174.11, 142.95, 132.12, 128.45, 120.68, 105.44, 93.58, 51.65, 35.64, 34.03, 30.73, 24.64, 0.19.

Synthesis of Methyl-5-(4-ethynylphenyl)pentanoate (5)[20]:

To a stirring solution of **4** (486.5 mg, 1.7 mmol, 1 equiv) in THF (50 ml), TBAF (2.36 ml, 2.36 mmol, 1.4 equiv) was added drop by drop over 4-5mins. Keep reaction mixture in dark all the time and monitor the reaction by TLC.   After 2h, the reaction was completed.   Water (25 ml) was added and the aqueous layer was extracted with dichloromethane (3×50 ml), dried over sodium sulfate, and the solvent removed *in vacuo*. The crude was purified by flash chromatography on a silica gel column by eluting with hexanes/ethyl acetate (9:1) to afford a yellow solid (219.3mg, 60% yield) after dry under vacuum. ^{1}H NMR (CDCl$_3$) δ 7.42-7.40 (2 H, d, J = 8.0), 7.14 − 7.12 (2 H, d, J = 7.95), 3.67 (3H, s), 3.04 (1 H, s), 2.65 -2.63 (2 H, d, J = 7.0), 2.34 − 2.32 (2 H, d, J = 7.0), 1.66 (4 H, m); ^{13}C NMR δ$_c$ (CDCl$_3$) 174.15, 143.30, 132.31, 128.58, 119.65, 83.95, 76.78, 51.72, 35.67, 34.05, 30.78, 24.67.

Methyl 5-(4-(pyren-1-ylethynyl)phenyl)pentanoate(6)[19]: To a solution of **5** (100 mg, 0.462 mmol, 1 equiv) and 1-iodopyrene (227 mg, 0.693 mmol, 1.5 equiv) in freshly distilled diisopropylamine (13 ml, 28 ml/mmol) and freshly distilled THF (13 ml, 28 ml/mmol), CuI (17mg,0.0924mmol,0.2equiv) was added. The reaction was purged with N$_2$ for 30 minutes and Pd(PPh$_3$)$_4$ (53.4 mg, 0.0462 mmol, 0.1 equiv) was added to form a yellow solution. The solution was refluxed at 86 °C overnight and the crude product was purified by column chromatography (hexane/ethyl acetate, 9/1) to afford **6** as dark orange oil (192.4 mg, 43% yield). ^{1}H NMR δ$_H$(CDCl$_3$) 8.69-8.67 (d, 2 H, J = 9.5), 8.25-8.07 (m, 9 H), 7.65-7.64 (d, 2H, J = 8.0), 3.69 (3H, s), 2.72 − 2.69 (2H, t, J = 7.0), 2.39 − 2.36 (2H, t, J = 7.0), 1.72 (4H, m).

5-(4-(pyren-1-ylethynyl)phenyl)pentanoic acid (7)[21]: To a stirring solution of **6** (80 mg, 0.19 mmol) in CH_2Cl_2 (50 ml), were added 5 ml of a 2 M NaOH solution in methanol, and stirring was continued at room temperature for 24 h. The solution was extracted with water (3×50 ml), then 10% HCl was added dropwise until pH~2. The aqueous acidic solution was extracted with CH_2Cl_2 (3×50 ml). The combined organic layers were dried over Na_2SO_4 and evaporated in vacuum to afford carboxylic acid **7** as a yellow solid (50 mg, 65 % yield). ^{1}H NMR δ_H(CDCl$_3$) 8.69-8.67 (d, 2 H, J = 9.5), 8.21-8.08 (m, 9 H), 7.66-7.64 (d, 2H, J = 8.0), 2.72 (2H, m), 2.44 (2H, m), 1.75 (4H, m). ^{13}C NMR δ_c (CDCl$_3$) 142.78, 131.99, 131.86 131.41, 131.28, 131.25, 129.70, 128.74, 128.40, 128.21, 127.41, 126.36, 125.76, 125.72, 125.66, 124.68, 124.66, 124.50, 121.09, 118.17, 95.39, 88.27, 36.69, 33.53, 30.72, 29.85, 24.42. HRMS (ESI)[+] *m/z* calcd for $[C_{29}H_{31}N_3O_2+Na]^+$ 476.2406, found $[M+Na]^+$ 476.2308.

D.3.2 Preparation of Nanostructured Metal Oxide Films

Titanium Dioxide Synthesis. Sol-gel preparation of TiO_2 nanoparticles was carried out via the hydrolysis of titanium(IV) isopropoxide in an aqueous nitric acid solution under nitrogen as previously reported procedures.[34,35] A three necked round bottom flask was set up with a thermometer, dropping funnel in the middle neck and Dean-Stark apparatus, as illustrated in Figure D 15. A 100 mL solution of water containing 0.69 mL of Conc. HNO_3 (68 − 70 %) was placed in the round bottom flask and allowed to stir vigorously at room temperature. A 20 mL solution of titanium(IV) isopropoxide was

placed in the addition funnel and diluted with 80 mL of isopropanol giving a total volume of 100 mL in the addition funnel. This solution was purged with nitrogen for 5 min and kept under a steady flow of nitrogen to prevent hydrolysis occurring before addition to the acidic solution. The latter mixture was then added dropwise to the acidic solution at a rate of *ca.* one drop per second. A white solid is immediately formed once the titanium(IV) isopropoxide:isopropanol mixture comes into contact with the acidic solution indicating rapid hydrolysis of the titanium(IV) isopropoxide. It is important to keep the reaction mixture stirring vigorously during this addition to prevent the formation of any large clusters of TiO_2 and also to prevent the TiO_2 particles from sticking to the glass reaction vessel, hence the dropping funnel being placed at the center of the flask.
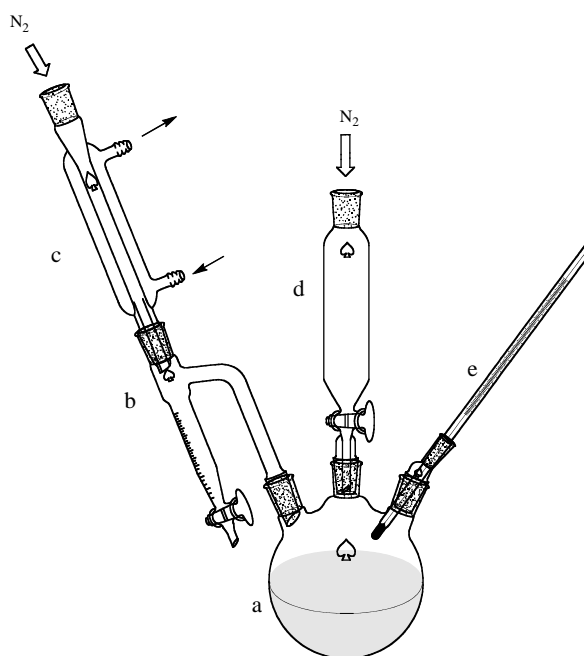

Figure D 15 Experimental set up for the hydrolysis.

After all the titanium(IV) isopropoxide solution was consumed and the hydrolysis was complete, changes in the set have to be made: the dropping funnel is removed and

the Dean-Stark apparatus as well as the flask should be covered by aluminum foil. The insulation is necessary during the following distillation. The isopropanol needs to be removed from the aqueous solution and can be collected as isopropanol/water mixture of approximately 130 mL at a temperature range of 86-95 °C. The distillation has to be terminated as soon as the distillate reaches 100 °C, indicating that only water remains in the solution. At this point the set-up is reduced to the three-neck round bottom flask with a condenser in the middle. The reaction mixture remains overnight to reflux. Following the reflux also the condenser is removed and the reaction volume is reduced to 45 mL by allowing the water to evaporate. The reaction mixture was allowed to cool down and sonicated for 5 min and transferred to the glass beaker with a magnetic stirring rod belonging to the titanium autoclave. The titanium autoclave (Model 4760, Parr) is programmed to heat the sol gel at 200 °C for 12 hours at a pressure reaching 17-18 bar.
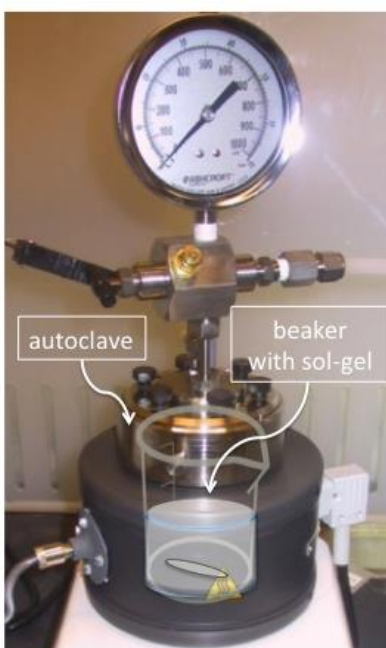

Figure D 16 Picture of the custom-made titanium autoclave for the sol gel process of TiO$_2$ nanoparticles (taken from reference 36).

The white sol-gel was cooled to room temperature, sonicated (5 min), and transferred from the autoclave beaker to a graduated beaker. At this point the TiO_2 concentration in the gel was determined by the 'glass dies' method. The method involves weighing a small amount of sol-gel on a glass slide before and after drying the gel at 100 °C to remove the containing water. The difference determines the wt. % of TiO_2 in the sol-gel. The concentration should be in a range of 13-17 wt % in order to be processed.

Poly(ethylene glycol) (PEG 2,000; av. Mol. Wt. 2,000) amount: 6 g/L was added to the colloid to yield a white viscous paste and the mixture was stirred for at least 72 h to reach a good homogeneity for the casting of TiO_2 paste on a substrate. The paste was left stirring and covered from light exposure for approximately up to one month for thin film preparation. Evidence of a degraded paste is a yellow discoloration. TiO_2 pastes older that one month were discarded.

Titanium Dioxide Film Preparation. The TiO_2 films were casted on conducting glass (FTO). Briefly, TiO_2 paste was spread using a glass test tube on the precut conductive glass, followed by sintering at 450 °C for 30 min under oxygen flow. The films were allowed to cool down before immediate use or were stored in a dark desiccator. No difference was observed when using films stored for weeks as indicated.

Zirconium Dioxide Film Preparation. Sol-gel preparation of ZrO_2 nanoparticles was carried out in a similar manner to that of TiO_2 nanoparticles described above. A three necked round bottom flask was set up with a thermometer, dropping funnel and Dean-Stark apparatus. A 100 mL solution of water containing 0.69 ml Conc. HNO_3 (68 –

70 %) was placed in the round bottom flask and allowed to stir vigorously at room temperature. A 20 mL solution of 70 % zirconium(IV) isopropoxide was placed in the addition funnel and diluted with 80 mL of isopropanol giving a total volume of 100 mL in the addition funnel. This solution was purged with nitrogen for 5 min and kept under a steady flow of nitrogen. The latter mixture was then added dropwise to the acidic solution at a rate of *ca*. one drop per second. The rapid formation of a white solid indicates rapid hydrolysis of the zirconium(IV) isopropoxide and immediate formation of the oxide nanoparticles. The reaction mixture was brought to reflux after addition is completed. Dean-Stark apparatus aided the distillation of isopropanol from the reaction mixture. During the first 3 h of reflux, a volume of *ca.* 170 mL isopropanol was collected over a temperature range of 86 – 95 ℃. When the reflux temperature reaches 100 ℃ all the isopropanol was removed. The Dean-Stark apparatus was removed and the reaction is allowed to reflux for 8 h. Following reflux, the water was evaporated from the flask until a final volume of 21 mL was reached (this corresponds to a ZrO_2 concentration of 2.13 M). The reaction mixture was allowed to cool. Stirring was sustained throughout procedure to maintain homogeneity of sol-gel. The resulting white sol was sonicated for 2 min. The white sol was then transferred to a glass beaker which was placed in a sealed titanium autoclave. The sol was allowed to stir in the autoclave with heating at 200 ℃ for 12 h (a typical pressure of 17 – 18 bar was observed). The sol was allowed to cool. The percentage weight ZrO_2 was calculated via the 'glass dies' method. The white sol was then transferred to a 50 mL beaker. In order to optimize the solution viscosity, poly(ethyleneglycol) (avg. Mol. Wt. 2,000) was added (*ca.* 1.5 g PEG per 25 cm^3 sol-gel). The PEG was allowed to stir in the sol-gel for 6 h. This gel was then applied on a

cover glass slide and stored as per the procedure described for the preparation of TiO_2 films. The morphology of ZrO_2 films was similar to that of TiO_2 and the average diameter of ZrO_2 nanoparticles were ~ 10 nm.

UV absorption spectra of TiO_2 and ZrO_2 Nanoparticles. TiO_2 has an absorption at 350nm and the absorption of ZrO_2 is at 300nm, as illustrated in Figure D 17.
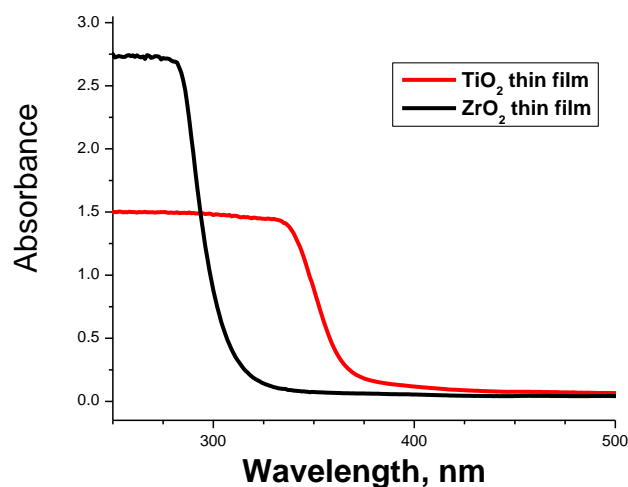

Figure D 17 UV adsorption of TiO_2 (red line) and ZrO_2 (black line).

D. 3.3 Binding Method

Binding of pyrene-**7** on TiO_2 and ZrO_2 were done by immersing the films in an aqueous solution with 40μM pyrene-**7** in acetonitrile solution for overnight (12~15h). Afterwards, the films were rinsed with neat solvents several times and dried under N_2.

Binding of the complex (pyrene-**7**@CB8) on TiO_2 and ZrO_2 followed previously reported method.[37] Experimentally, we determined pyrene-**7**@CB8 formed a 1:1 complexation. To ensure all the pyrene unites were complexed, we used 2 equivalent of

CB[8] as host. Therefore, pyrene-**7** was added into CB[8] aqueous solution to form 1:2 guest@host complexes with 40 μM the concentration of pyrene-**7**. TiO_2 and ZrO_2 films were immersed into this solution for one day. Then, the films were carefully dried under N_2.

D.4 Conclusion

The absorption of pyrene-**7** was seen to be shifted to longer wavelengths compared with those of the unsubstituted pyrene, and fluorescence quantum yields of pyrene-**7** also significantly increased. Fluorescence emission spectra were used to study only pyrene-**7** and pyrene-**7**@CB[8] bound to metal oxide surfaces. TiO_2 and ZrO_2 were used as nanostructured metal oxide surfaces with similar morphologies but different band gaps. For pyrene-**7** bound to TiO_2 and ZrO_2, excimer formation was observed through fluorescence emission with broad and red-shifted emission peaks. Cucurbit[8]uril form a water-soluble 1:1 guest@host complexe with pyrene. Pyrene-**7**@CB[8] complexes bound to TiO_2 showed the presence of monomer peak on TiO_2 and ZrO_2. However, with ZrO_2, the presence of pyrene monomer peak has higher intensity and the emission spectra were well-defined and blue-shifted. Meanwhile, for both surfaces, the excimer was still present with pyrene-**7**@CB[8] complexes. By formation of pyrene-**7**@CB8 complexe, CB[8] could improve the separation of pyrene units and suppress the excimer formation.

D.5 References

(1)   R. P. Haugland, Handbook of Fluorescent Probes and Research Chemicals, 9th ed., Molecular Probes, Eugene (OR), 2002.

(2)   Karpovich, D. S.; Blanchard, G. J. *The Journal of Physical Chemistry* **1995**, *99*, 3951.

(3)   Katoh, R.; Suzuki, K.; Furube, A.; Kotani, M.; Tokumaru, K. *The Journal of Physical Chemistry C* **2009**, *113*, 2961.

(4)   Förster, T. *Angewandte Chemie International Edition in English* **1969**, *8*, 333.

(5)   Fujimoto, K.; Shimizu, H.; Inouye, M. *The Journal of Organic Chemistry* **2004**, *69*, 3271.

(6)   Ramamurthy, V. Photochemistry in Organized and Constrained Media; VCH Publishers: New York, 1991.

(7)   Bains, G.; Patel, A. B.; Narayanaswami, V. *Molecules* **2011**, *16*, 7909.

(8)   Kalyanasundaram, K.; Thomas, J. K. *Journal of the American Chemical Society* **1977**, *99*, 2039.

(9)   Patel, A. B.; Khumsupan, P.; Narayanaswami, V. *Biochemistry* **2010**, *49*, 1766.

(10)   Nakajima, A. *Journal of Molecular Spectroscopy* **1976**, *61*, 467.

(11)   Bohne, C. *Chemical Society reviews* **2014**.

(12)   Dyck, A. S. M.; Kisiel, U.; Bohne, C. *The Journal of Physical Chemistry B* **2003**, *107*, 11652.

(13)   Lehrer, S. In *Proteins: Structure, Function, and Engineering*; Biswas, B. B., Roy, S., Eds.; Springer US: 1995; Vol. 24, p 115.

(14)   Du, H.; He, G.; Liu, T.; Ding, L.; Fang, Y. *Journal of Photochemistry and Photobiology A: Chemistry* **2011**, *217*, 356.

(15)   Thyagarajan, S.; Galoppini*, E.; Persson, P.; Giaimuccio, J. M.; Meyer, G. J. *Langmuir : the ACS journal of surfaces and colloids* **2009**, *25*, 9219.

(16)   Cao, Y.; Galoppini, E.; Reyes, P. I.; Lu, Y. *Langmuir : the ACS journal of surfaces and colloids* **2013**, *29*, 7768.

(17)   Thyagarajan, S.; Galoppini, E.; Persson, P.; Giaimuccio, J. M.; Meyer, G. J. *Langmuir : the ACS journal of surfaces and colloids* **2009**, *25*, 9219.

(18)   Jiao, D.; Geng, J.; Loh, X. J.; Das, D.; Lee, T.-C.; Scherman, O. A. *Angewandte Chemie International Edition* **2012**, *51*, 9633.

(19)   Gibson, S. E.; Jones, J. O.; Kalindjian, S. B.; Knight, J. D.; Mainolfi, N.; Rudd, M.; Steed, J. W.; Tozer, M. J.; Wright, P. T. *Tetrahedron* **2004**, *60*, 6945.

(20)   Grosshenny, V.; Romero, F. M.; Ziessel, R. *The Journal of Organic Chemistry* **1997**, *62*, 1491.

(21)   Theodorou, V.; Skobridis, K.; Tzakos, A. G.; Ragoussis, V. *Tetrahedron Letters* **2007**, *48*, 8230.

(22)   Crosby, G. A.; Demas, J. N. *The Journal of Physical Chemistry* **1971**, *75*, 991.

(23)   Shirdel, J.; Penzkofer, A.; Procházka, R.; Shen, Z.; Strauss, J.; Daub, J. *Chemical Physics* **2007**, *331*, 427.

(24)   Kim, J.; Jung, I.-S.; Kim, S.-Y.; Lee, E.; Kang, J.-K.; Sakamoto, S.; Yamaguchi, K.; Kim, K. *Journal of the American Chemical Society* **2000**, *122*, 540.

(25)   Ivanov, D. A.; Petrov, N. K.; Nikitina, E. A.; Basilevsky, M. V.; Vedernikov, A. I.; Gromov, S. P.; Alfimov, M. V. *The Journal of Physical Chemistry A* **2011**, *115*, 4505.

(26)   Walker, S.; Kaur, R.; McInnes, F. J.; Wheate, N. J. *Molecular Pharmaceutics* **2010**, *7*, 2166.

(27)   Day, A.; Arnold, A. P.; Blanch, R. J.; Snushall, B. *The Journal of Organic Chemistry* **2001**, *66*, 8094.

(28)   Sasmal, S.; Sinha, M. K.; Keinan, E. *Organic letters* **2004**, *6*, 1225.

(29)   Yi, S.; Kaifer, A. E. *The Journal of Organic Chemistry* **2011**, *76*, 10275.

(30)   Rochford, J.; Galoppini, E. *Langmuir : the ACS journal of surfaces and colloids* **2008**, *24*, 5366.

(31)   Rochford, J.; Chu, D.; Hagfeldt, A.; Galoppini, E. *Journal of the American Chemical Society* **2007**, *129*, 4655.

(32)   Galoppini, E. *Coordination Chemistry Reviews* **2004**, *248*, 1283.

(33)   Thyagarajan, S.; Liu, A.; Famoyin, O. A.; Lamberto, M.; Galoppini, E. *Tetrahedron* **2007**, *63*, 7550.

(34)   Heimer, T. A.; D'Arcangelis, S. T.; Farzad, F.; Stipkala, J. M.; Meyer, G. J. *Inorganic Chemistry* **1996**, *35*, 5319.

(35)   Taratula, O.; Galoppini, E.; Wang, D.; Chu, D.; Zhang, Z.; Chen, H.; Saraf, G.; Lu, Y. *The Journal of Physical Chemistry B* **2006**, *110*, 6506.

(36)   Freitag, M. Ph. D. dissertation, Rutgers - Newark, 2011

(37)   Freitag, M.; Galoppini, E. *Langmuir : the ACS journal of surfaces and colloids* **2010**, *26*, 8262.

Chapter E

Functionalization of Rubrene Single Crystal

E.1 Background

E.1.1 Rubrene Single Crystal

In this thesis, we initiated a new direction for our work involving organic semiconductors. Organic semiconductors based on Π-conjugated small molecules or polymers have engendered substantial research interest for commercial applications in sensors, solar cells, light-emitting diodes, and printable electronics.[1,2,3] Organic semiconductor-based electronic devices hold the promise of low-cost manufacturing, high performance, and compatibility with flexible substrates, which is believed to successfully compete with inorganic electronics.[4] Carrier mobility in organic semiconductors is a topic of active ongoing research aimed at material characteristics for obtaining high performance of devices.[5] In particular, the single crystal of rubrene (5,6,11,12-tetraphenylnapthacene, $C_{42}H_{28}$ in inset Figure E 1) has been demonstrated as one of the highest mobility organic semiconductor materials.[6] Rubrene single crystal is an electron rich p-type semiconductor and OFETs (Organic Field Effect Transistor) based on single-crystalline rubrene have been prepared. Rubrene exhibits a room-temperature field-effect hole mobility as large as 20 $cm^2V^{-1}s^{-1}$.[7, 8] This intrinsic transport behavior on the surface of rubrene crystals has been further confirmed by Hall measurements that yield mobilities consistent with the FET (Field Effect Transistor) measurements.[9]
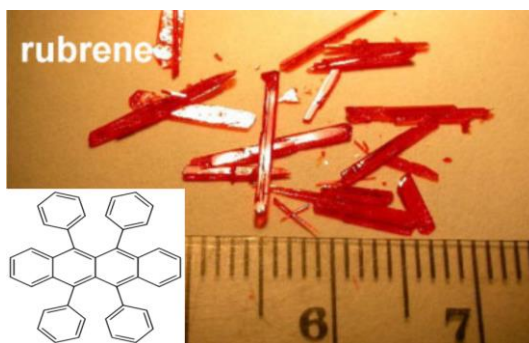
Figure E 1 Rubrene single crystals (taken from reference 6) and structure

Single rubrene crystals have been grown from the vapor phase in a stream of transport gas, in horizontal reactors of glass or quartz tubing.[10, 11] Most of the organic crystals are shaped as elongated needles or thin platelets.[12] In the physical vapor transport method, the starting material is placed in the hottest region of the reactor, and the crystal growth occurs within a narrow temperature range near its cold end. For better separation of larger and purer crystals from the rest of the re-deposited material along the tube, the temperature gradient should be sufficiently small (typically, 2-5°C/cm).[12] Ultra-high-purity hydrogen has been used as a transport gas to grow high quality rubrene crystals. It is unclear at present how the transport gas affects the quality of the crystals. Uncontrollable variations of the crystal quality have been observed and could be caused by residual water vapor or oxygen in the reactors.[12]

Photo-induced reactions with oxygen have been reported for organic molecules and the products of these photo reactions can act as traps for carrier charges or as anchor groups to bind rubrene.[13] The exact mechanism of the photo-induced reaction with rubrene is not fully understood. The main proposed rubrene defects observed from oxygen contamination resulting in epoxy, peroxide, and alcohol substituents[14] are listed

in Figure E 2. Previous studies by Podzorov suggest the monolayer molecules covalently

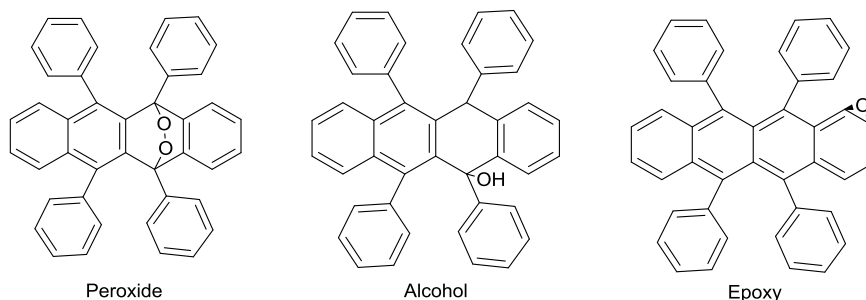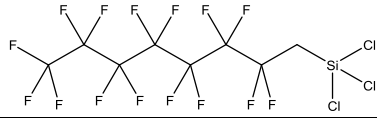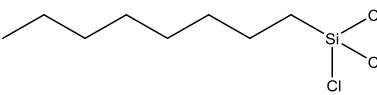bind to the oxygen defects, of which more details will be discussed later.
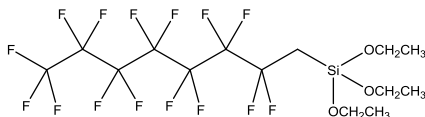

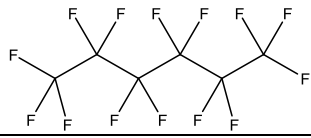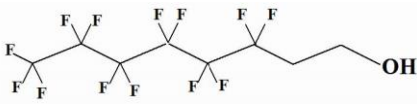Peroxide   Alcohol   Epoxy

Figure E 2 Some possible rubrene derivatives from oxygen contamination (taken from reference 14).

E.1.2 Functionalization of the Surface of Rubrene with self-assembled monolayers

Self-Assembled Monolayers (SAMs) have been extensively studied and widely

used for a variety of surface modifications.[15,16,17] Podzorov and coworkers proposed for

the first time the growth of organosilane SAMs at the surface rubrene.   Several

organosilane SAM molecules listed in Table E 1 have been investigated, such as non-

fluorinated silanes, n-octyltrichlorosilane (OTS), and fluorinated silanes (tridecafluoro-

1,1,2,2-tetrahydrooctyl)trichlorosilane   (FTS).[18]   Their conductivity change was

monitored throughout the functionalization process.

Table E 1 Organosilane SAM molecules grown on rubrene single crystals (taken from reference **18**)

	Structure	Name	Effect on Conductivity
1		(tridecafluoro-1,1,2,2-tetrahydrooctyl)trichlorosilane (FTS)	very large increase (four to five orders of magnitude)
2		n-octyltrichlorosilane (OTS)	small increase (a factor of ten)
3		fluoroalkyltriethoxysilane	medium increase (two orders of magnitude)
5		tetradecafluorohexane	none
7		1*H*,1*H*,2*H*,2*H*-perfluoro-1-octanol	large increase, but vanishes *in vacuo*

From the results shown in Table E 1, trichlorosilanes, triethoxysilanes and trimethoxysilanes have shown a persistent and reproducible increase of conductivity. Molecule 5 has similar fluorinated structure without the change of conductivity. Molecule 7 is the only non-silane molecule which has resulted in a large increase of conductivity. However, this increased conductivity is reduced to its initial value by pumping the sample chamber with a mechanical pump. The change of conductivity

indicates that this weak bind is due to physisorbtion at the surface, such as weak hydrogen bonds of the C-OH group to the rubrene surfaces. In summary, trichlorosilane, trimethoxysilane and triethoxysilane form a permanent strong covalent bond to rubrene crystal surfaces. Based on the efficiency of hydrolysis, trichlorosilane performed the highest as anchor group for the functionalization of rubene.

The mechanism of SAM formation with silane as anchor group at the surface of rubrene crystals has not yet been fully understood. However, the reactions involved in the self-assembly of silane molecules at silicon dioxide surface are reasonably well understood.[19] Chabal's group has used infrared absorption spectroscopy (IRAS) to determine silane-rubrene bond since IRAS has sufficient sensitivity to reveal submonolayer-bonding events on silicon surfaces,[20, 21, 22, 23] and proposed that the endoperoxide species that formed upon exposure of the rubrene surfaces to atmospheric oxygen and ambient light provided a reactive site for silane molecules.[24] Silanes may hydrolyze in the presence of water on the rubrene surfaces to form trichlorosilanols, then hydroxyl groups bind to oxidized sites present on rubrene (in Figure E 3). The signature of this interaction, a Si-O-C bond was observed by IRAS.

Figure E 3 The proposed mechanism for silane binding to rubrene

However, infrared transmission of a rubrene crystal does not allow a sufficient infrared beam to reach the detector with acceptable signal intensity. IRAS characterization was only applied on spin-cast rubrene thin films. Frisbie's group has further studied the silane SAM formed on surfaces by using Kelvin Probe Force Microscopy (KFM) to study surface potential mapping.[14] KFM is a noncontact technique sensitive to surface potential variations due to molecular dipoles. The findings were in good agreement with the mechanism proposed by Yves Chabal. The dipole, measured by KFM, is indicative of the mixed surface chemistry. It is likely that not all of the silane molecules are directly bonded to rubrene and therefore they will not all have the same dipole moment. Specifically, there are two types of silane molecules in the SAMs: "bonded" silanes that are directly connected to rubrene via an Si-O-rubrene lingae, and "un-bonded" silanes that form a surrounding cross-linked network with no direct connection to the rubrene (in Figure E 3).[14]

As illustrated in Table E 1, the increase of conductivity was observed and caused by the large dipole moment between p-type rubrene crystals (holes) and fluorinated electron withdrawing groups (negative charges) of SAM layers introduced, which leads to the possibility of doping organic semiconductors (Figure E 4). The possibility that HCl released during the hydrolysis of trichlorosilane (the dopant) was excluded by a simple control experiment in which rubrene crystals were directly exposed to HCl gas. The conductivity was monitored and showed no significant change.
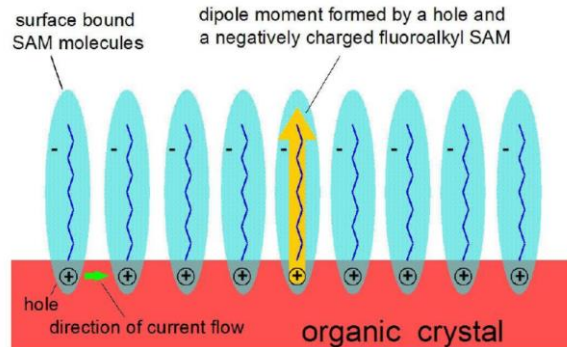
Figure E 4 The proposed surface doping by SAM (taken from reference **18**)

Besides the conductivity measurements, a number of electrical analysis techniques were applied for studying the surface properties of SAMs modified rubrene crystals. Scanning Electron Microscopy (SEM) of SAM layers on rubrene surfaces at different times of binding, showed that at initial binding stage, SAM molecules tend to grow around surface defects, such as molecular growth steps, and dust to create the islands. As the binding time increased, the SAM islands grew in size until the entire surface was coated uniformly with SAM islands.[14,18] Also, atomic force microscopy (AFM) studies the thickness of SAM layers, showing that the average height of the SAM islands is in good agreement with the length of the FTS molecules.[25] This suggests that FTS molecules stand nearly perpendicular with respect to the surface basal plane as in Figure E 4.

The sensing behavior of rubrene crystals when exposed to chemical vapors of organic solvent was also investigated by Ji's group.[26] The resistivity of rubrene has a marginal change upon exposure to benzene, ethanol, acetone, hexane, dimethylformamide. Furthermore, Podzorov's group has reported the effect of chemical vapors of solvents to SAM functionalized rubrene crystal surfaces.[18] Polar solvents, such

as acetone, ethanol, and proponal, caused a decrease of conductivity of SAM functionlized rubrene and non-polar solvents, such as hexane and pentane, do not cause a decrease in conductivity.[18] It is likely that polar solvents are able to penetrate between the SAM molecules and introduce orientational disorder that creates a rough potential landscape at the interface, leading to localization of conducting holes and creating a decrease of SAM induced conductivity.[18]

Overall, silane molecules have been studied to functionalize rubrene single crystal surfaces for doping by inducing a dipole moment with highly fluorinated chains. However, the chemistry and perspective of this method are limited by the extreme moisture sensitivity of silane molecules and the very limited surface chemistry explored thus far. In this thesis, we report for the first time that graft substituted aryl groups via the diazotization reaction on the rubrene single crystals.

E.2 Results and Discussion

In this chapter, we proposed one step functionalization method for further tuning the rubrene crystal surfaces by silane molecules. We also tested a step-wise functionalization strategy to attach desired head groups onto the monolayer via secondary click chemistry with various anchor groups. In addition to silane molecules, we also grafted aryl groups via the diazotization reaction, since aryldiazonium slats have enabled researchers to graft subsitituted aryl groups onto grapheme, silicon or metal surfaces, thereby forming well-ordered monolayers.[27,28,29] To our knowledge, no research group has applied this anchoring method to rubrene crystals. Material characteristics, such as

conductivity change and carrier mobility, which in turn depend on the surface properties of the semiconductor, were used to monitor the each step of functionalization.

The result of conductivity change and carrier mobility were carried out in the group of Professor Vitaly Podzorov at Rutgers University-New Brunswick, with the assistance of Dr. Yuanzhen Chen.

## E.2.1 One step functionalization method for surface doping

Rubrene single crystal was provided by the Podzorov group. The synthesis of rubrene single crystal has been reported previously.[10,12] The crystals are transparent orange colored platelets, typically 0.1-2μm thick, as showed in Figure E 5. The crystal samples were stored in the dark.

Figure E 5 Rubrene Single Crystals

Head-Linker-Anchor (HLA) molecules were synthesized, where the head group consists of an electron donor (D) or acceptor (A) group (as illustrated in Scheme E 1, N,N-dimethyl aniline (NMe$_2$) as donors and Nitro (NO$_2$) as acceptors), the linker group a modified phenyl moiety, and the anchor group a modified siloxane to bind the molecules to the surfaces of single crystal rubrene samples. The goal of the one-step

functionalization with HLA molecules is to explore doping of the surface region of rubrene (both for p-type and n-type modifications). Obtaining n-type doping is particularly attractive as it has not been achieved for rubrene.
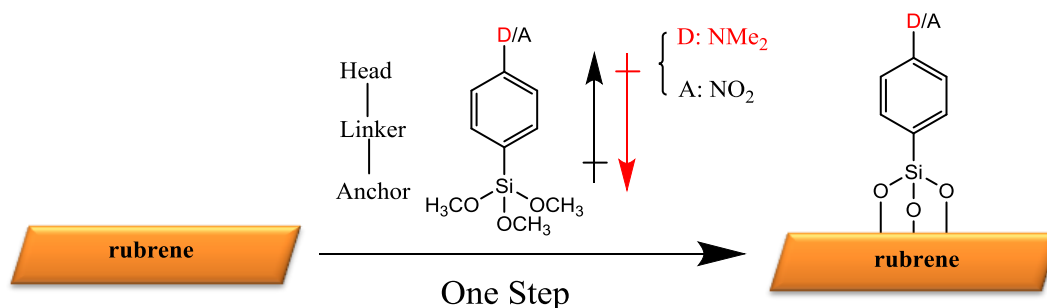
Scheme E 1 Representative donor/acceptor head units for the proposed HLA systems on rubrene crystals

Synthesis of HLA molecules: The syntheses of 4-ethynyl-*N.N*-dimethylanilline **1** and 1-ethynyl-4-nitrobenzene **3** were through Sonogashira reactions to couple with 4-bromo-N,N-dimethylaniline. *N,N*-dimethyl-4-((trimethoxysilyl)ethynyl)aniline **2** and triethoxy((4-nitrophenyl)ethynyl)silane **4** were synthesized using lithium diisopropylamide or *n*-butyllithium as strong base in a nucleophilic substitution reaction.[16,30] Due to extreme water and air sensitivity of the trimethoxy silane molecules, the purification of these molecules was challenging. Silane products were stored under nitrogen.

In our case, N,N-dimethyl-4-((trimethoxysilyl)ethynyl)aniline **2** and triethoxy((4-nitrophenyl)ethynyl)silane **4** have high boiling points and very low stability in air, leading to low quality of the desired products. The results collected from ^{1}H NMR and

GC/MS analysis showed the majority of each sample consisted of a mixture of desired product and uncharacterized impurities.
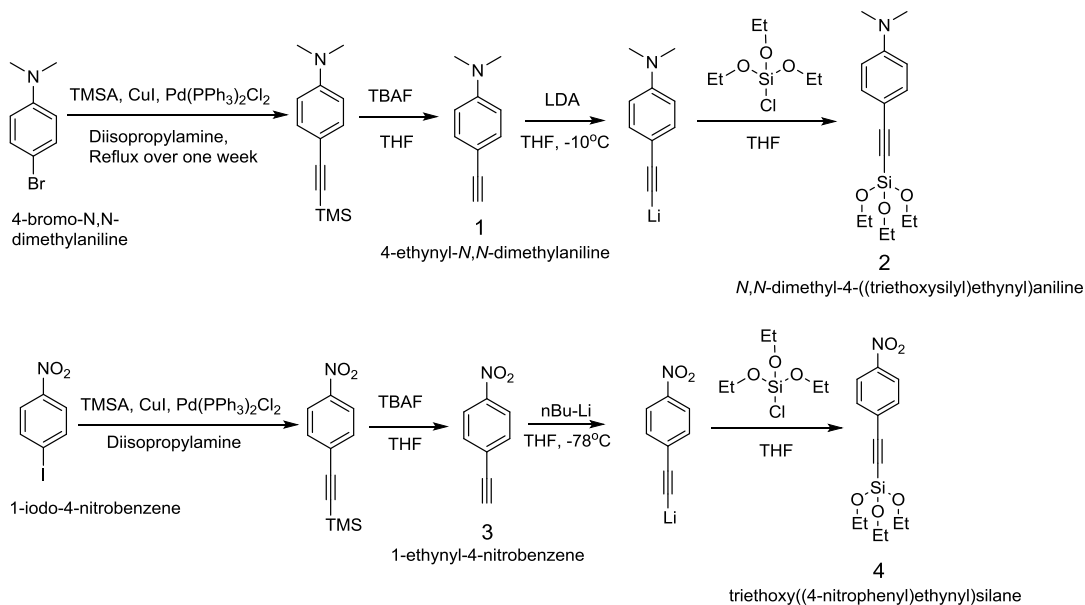
Figure E 6 The synthesis of Head-Linker-Anchor Molecules

Conductivity Measurement:

The conductivity of rubrene crystal samples were measured after functionalization with HLA molecules **2** and **4**. With the HLA molecules modified with $-NO_2$ as the head groups, initial conductivity of the rubrene crystal was 0.5 nS, and, after functionalization, conductivity increased four-fold to 2 nS. With the HLA molecules modified with electron donors as the head groups, no detectable change in conductivity was observed. In previous studies, (tridecafluoro-1,1,2,2-tetrahydrooctyl)trichlorosilane (FTS) as self-assembled monolayers was deposited directly on rubrene crystals and their surface conductivity showed an increase of four to five orders of magnitude.[18] This dramatic increase the result of a large dipole moment based on FTS. The design of HLA molecules were similar with FTS, however the conductivity change was decreased. The

possible explanations for this result are either low binding efficiencies of triethoxysilane or the weak electron donating and accepting properties of the groups utilized.

Conclusion: The results for one-step functionalization of rubrene single crystal with HLA molecules for further doping surfaces were not satisfactory. In summary, the electronic properties of rubrene surfaces were not tunable in a controllable manner through these HLA systems.

E. 2.2 Step-wise Functionalization of Rubrene through Azide Substitution Reaction

We proposed to form azide functional layers at the surface of rubrene crystals for further functionalization via click chemistry. Two routes were explored, as illustrated in Scheme E 2. In route 1, we directly deposited a synthesized 3-azidopropyltrimethoxysilane as SAM molecule (trimethoxysilane as anchor group and azide as the head group). In previous studies by our collaborator Dr. Podzorov, trichlorosilane performed better as an anchor group than trimethoxysilane and triethoxysilane for binding to rubrene surfaces. In route 2, we explored the functionalization of rubrene crystals with (3-bromopropyl)trichlorosilane with trichlorosilane as anchor group, leaving bromine as head groups for azide substitution reaction. We deposited the first layer by vapor deposition methodology as described in the Experimental Section. The azide substitution reaction was carried out in water to prevent dissolution and damage of the rubrene crystals by organic solvents.
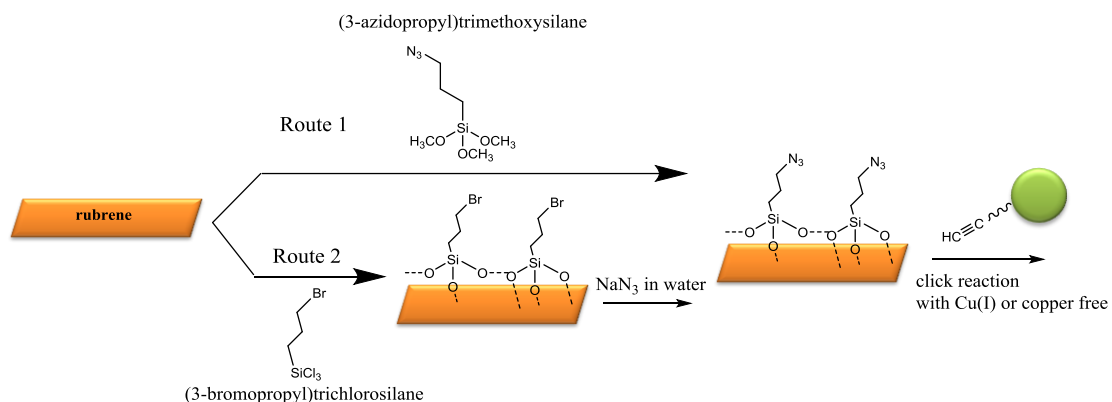
Scheme E 2 Proposed step-wise Functionalization of Rubrene

Route 1- Direct deposit azide modified monolayers: FTIR-ATR was used as preliminary characterization method to monitor binding after a few drops of concentrated 3-azidopropyltrimethoxysilane were directly deposited on rubrene crystals for 24h at room temperature. The spectrum of the azide-terminated layer (Figure E 7, top red line) showed a strong band at 2096 cm^{-1} characteristic of the asymmetric stretching band ν_{as} of the azide group, $_{as}(N_3)$.[31]
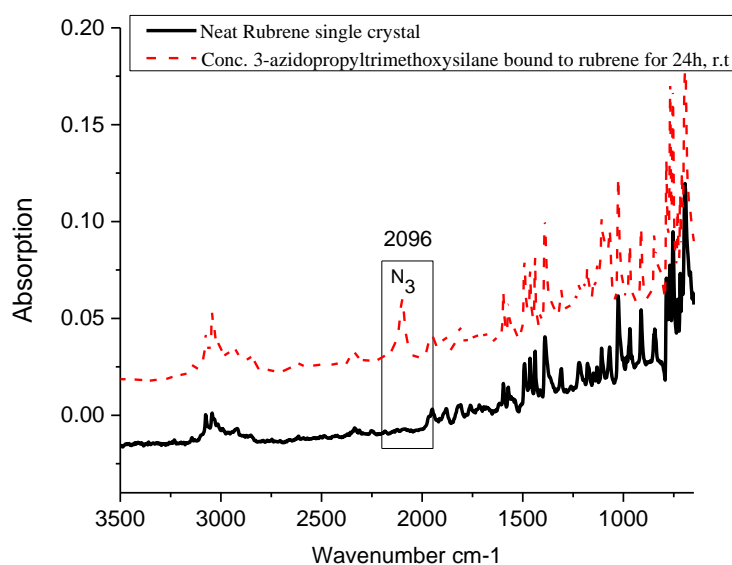
Figure E 7 FTIR-ATR Spectra of 3-azidopropyltrimethoxysilane bound to Rubrene single crystal

However, FTIR-ATR measurements may damage the functionalized rubrene crystals as they require contact pressure on the crystal surface, so we employed conductivity measurements as the main technique to monitor functionalization. Conductivity change was not significant and did not yield stable readings during the functionalization process with 3-azidopropyltrimethoxysilane. Possible explanations for the low impact on the conductivity are first, low coverage on the rubrene surface; second methanol, as a byproduct of trimethoxysilane functionalization of rubrene, could partially damage or dissolve rubrene crystals. The observation of small visible bubbles, Figure E 8, seems to support this hypothesis.
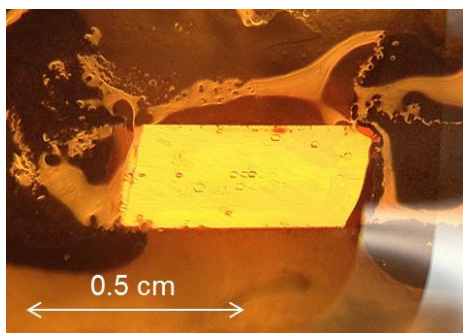
Figure E 8 Partial damage of rubrene single crystal after functionalization

Route 2- Step-wise functionalization of rubrene through azide substitution: The conductivity was monitored throughout the entire process, as illustrated in Figure E 9. Dark conductivity was increased by about two orders of magnitude after rubrene crystals were explored under vapor deposition of (3-bromopropyl)trichlorosilane for 2 h at room temperature. Over seven weeks, the dark conductivity did not change, suggesting that the

SAM-functionalization was stable. Upon replacement of -Br by -N_3, the conductivity decreased by one order of magnitude.
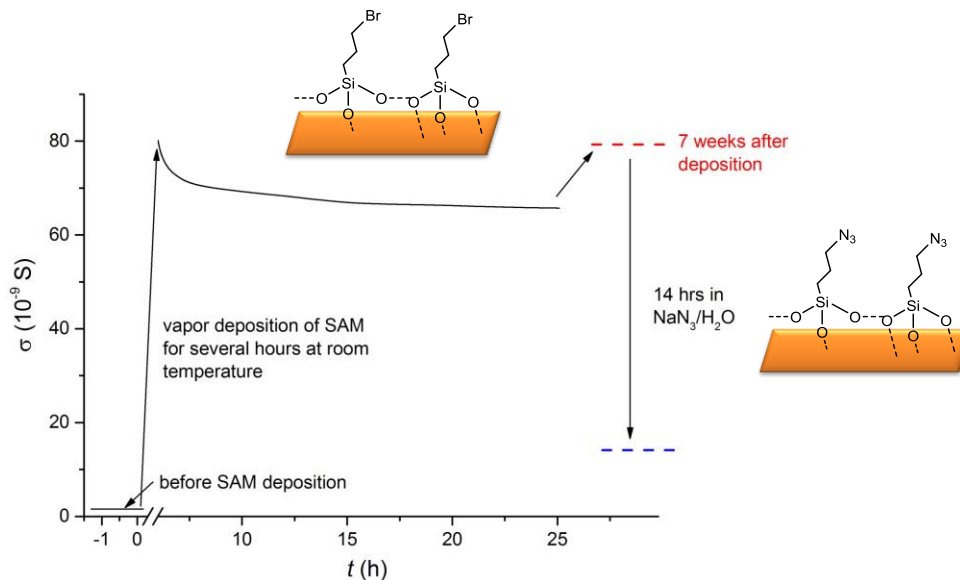
Figure E 9 Conductivity Monitor of step-wise functionalization

The entire functionalization process was carried out on three different samples with different binding times and different temperatures. Sample A (left, in Figure E 10) was deposited with vapor of (3-bromopropyl)trichlorosilane for 2h at room temperature, Sample B (middle, in Figure E 10) was deposition with higher temperature (60°C) for 3h, and Sample C (right, in Figure E 10) was deposition for 2 days at room temperature. The conductivity for the rubrene crystals without functionalization was close to zero. With the formation of (3-bromopropyl)trichlorosilane layer, the conductivity significantly increased (red cubic, in Figure E 10) for all three samples. This increase could be based on the dipolar moment introduced by bromine terminated monolayers, which is consistent with previous studies.[18] Moreover, with the increase of temperature and longer deposition time, the conductivity has increased more. This result could also be due to the increased surface coverage with bromine terminated monolayers. Also, the rubrene

single crystals were hydrophobic, an observation supporting functionalization with a hydrophobic chain. After deposition with the terminal bromine layer, it became hydrophilic which supports the presence of the polar functional layer. After azide substitution reaction by immersing three samples into sodium azide aqueous solution for certain time at room temperature, the conductivity has decreased for all three samples. The possible explanation is the disappearance of dipole moment introduced by bromine.
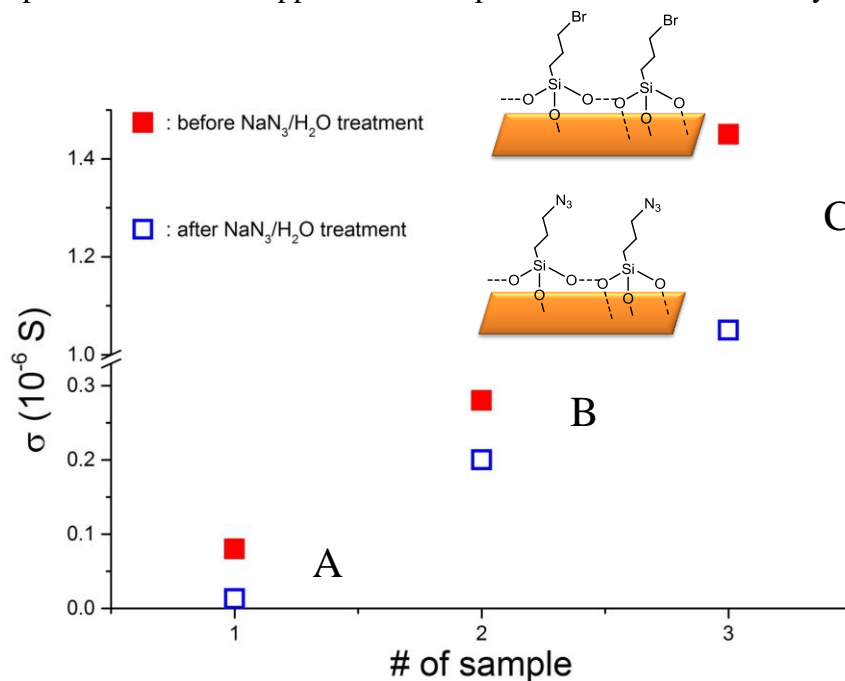
Figure E 10 Conductivity Monitor of three functionalization samples under various experiment condition

Generally, carrier mobility (μ) refers to electron and holes mobility in semiconductors and it is also the most common parameter used to characterize semiconductors. The most commonly used experimental method for mobility determination in semiconductors are Hall effect measurements.[32] Hall Effect can be observed when the combination of a magnetic field (B) through a sample and a current along the length of the sample (I_0) creates an electrical current (I) perpendicular to both

the magnetic field and the current, which in turn creates a transverse voltage (V_{Hall}) that is perpendicular to both the magnetic field and the current, as illustrated in Scheme E 3. The carrier mobility was calculated based on equation 2.
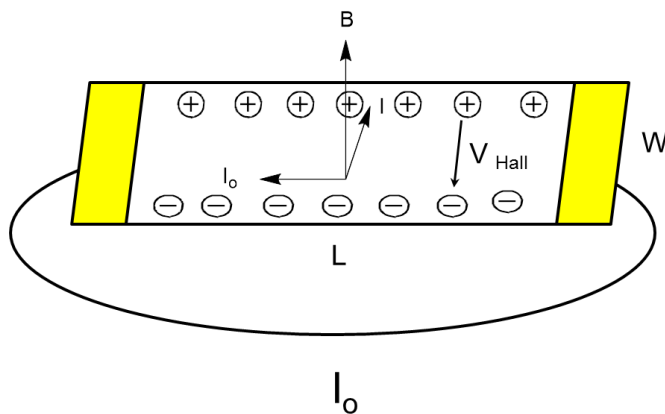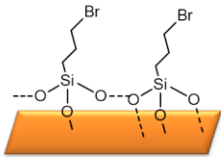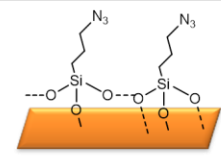
$$V_{Hall}=V_L(W/L)\mu B+V_0 \qquad eq\ (2)$$

Scheme E 3 Hall Measurement

The carrier mobility was listed in Table E 1 for three samples. From Sample A to Sample C, the conductivity increased with increasing surface coverage. However, the carrier mobility decreased with the increase of conductivity. The possible explanation was with more surface coverage, the bromine terminated layer molecules were stabilized holes of rubrene crystals that the mobility of holes decreased. This was also observed with previous studies.[33] After the azide substitution reaction, for Sample A, conductivity measurements were impossible due to the increase in noise arising from the change in carrier mobility.

Table E 2 Hall Measurement Data of three samples

	A	B	C
(3-bromopropyl)silane structure (Br, Br)	2.6cm²/(Vs)	0.55cm²/(Vs)	0.6 cm²/(Vs)
azide-substituted silane structure (N₃, N₃)	Too noisy to detect	1.8 cm²/(Vs)	0.5 cm²/(Vs)

In summary, (3-bromopropyl)trichlorosilane was successfully bound on rubrene through trichlorosilane as anchor group, and the azide substitution was observed. Conductivity and carrier mobility was used to characterize the functionalization of rubrene crystals. XPS measurements are in progress

E. 2.3 Aryl Diazonium Salts as New Anchor Group

Employing aryl diazonium salts as an anchor group can be used instead of silanization to overcome the moisture sensitivity of silane molecules. The diazonium salts will anchor through a robust C-C bond. They may bind at sites that differ from the silanization sites and may lead to extensive and uniform functionalization without in-plane polymerization. The bound aromatic group will be conjugated and rigid and can carry substituents. In applications with rubrene, this reaction can lead to grafting at the pendant phenyl rings, dramatically altering the properties of rubrene.[34]

The mechanism of the diazonium salt reaction with the rubrene crystals most likely occurs through a free radical mechanism, as has been proposed for the diazonium functionalization of the graphane and graphene.[35,36] In our case, 4-bromobenzenediazonium tetrafluoroborate was chosen for functionalization of rubrene crystal surfaces, as the tetrafluoroborates can be stored almost indefinitely at room temperature, decompose gently when heated, and are easy to handle experimentally. Moreover, the bromine-terminated head group was expected to change the conductivity of rubrene, similar to (3-bromopropyl)trichlorosilane-functionalized rubrene. The conductivity and carrier mobility was monitored.

As illustrated in Figure E 11, dark conductivity dramatically increased due to functionalization by 4-bromobenzenediazonium tetrafluoroborate. Over seven weeks, the conductivity did not change, indicating the SAM-functionalization is quite stable. From the Hall measurement, mobility (μ) were extracted, $\mu = 0.74$ cm^2/(Vs). In conclusion, the preliminary results showed for the first time that aryl diazonium salts can be applied as anchor groups for the functionalization of rubrene.
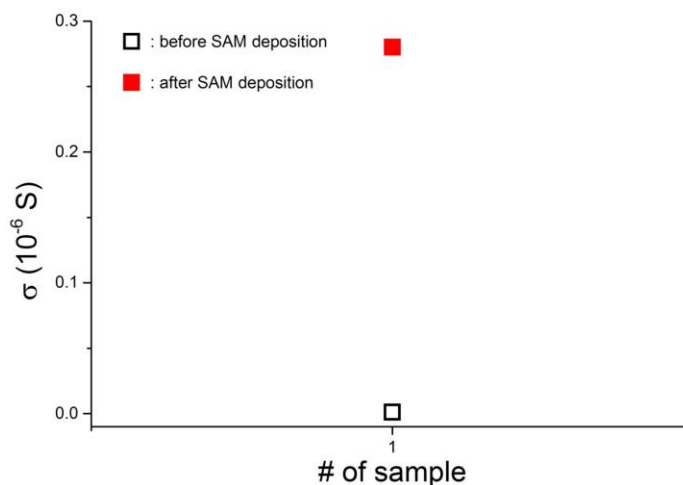
Figure E 11 Dark conductivity measurement

E.3 Experimental Section

General.

Materials: All reactions involving air- and moisture-sensitive reagents were performed under nitrogen atmosphere and in oven-dried or flame-dried glassware. THF was distilled with sodium and benzophenone while under N_2 atmosphere or purified with an MBraun MB-SPS compact benchtop solvent purification system with purification columns for THF. Diisopropyl amine and dichloromethane were distilled over calcium hydride under N_2 atmosphere. 4-Bromo-N,N - dimethylaniline (VWR), 1-Iodo-4-nitrobenzene (VWR), (3-bromopropyl)trichlorosilnae (Sigma-Aldrich), 4-Bromobenzenediazonium tetrafluoroborate salt(Sigma-Aldrich), sodium azide (99%, Alfa Aesar), CuI (Acros Organics), $PdCl_2(PPh_3)_2$ (Strem), Trimethylsilyl Acetylene (Alfa Aescar), TBAF (Tetrabutylammonium fluoride, 1.9M solution in tetrahydrofuran) (Sigma-Aldrich), Lithium Diisopropylamide (LDA, 2.0M in THF/heptane/ethylbenzene), n-Butyllithium (2.5M in hexanes), dimethylformamide were used as received.

Methods: ^{1}H-NMR and ^{13}C-NMR spectra were collected on a Varian NMR spectrometer operating at 499.896 MHz for ^{1}H and 125.711 MHz for ^{13}C. Chemical shifts were reported relative to the central line of the solvent: $CDCl_3$ (δ 7.27 ppm) for ^{1}H spectra and $CDCl_3$ (δ 77.27 ppm) for ^{13}C spectra, and coupling constants (*J*) are reported in Hz. Single attenuated total reflectance infrared (FTIR-ATR) spectra were performed

on a Thermo Electron Corporation Nicolet 6700 FT-IR (ZnSe Crystal, number of spectra averaged 128, resolution 4 cm^{-1}).

E.3.1 Synthesis

Synthesis of 4-ethynyl-N,N-dimethylaniline (1)[37]:

To a stirring solution of 4-Bromo-N,N-dimethylaniline (1 g, 5 mmol, 1 equiv) in fresh distilled diisopropylamine (115 mL, 23 ml/mmol), PdCl$_2$(PPh$_3$)$_2$ (350 mg, 0.50 mmol, 0.1 equiv) and CuI (190 mg, 1.0 mmol, 0.2 equiv) were added under nitrogen atmosphere. After 10 min, trimethylsilylacetylene (6.3 mL, 45 mmol, and 9 equiv) was added and the reaction mixture was stirred at 87°C for over one week. The dark reaction mixture was purified by flash chromatography on a silica gel column by eluting with hexanes/ethyl acetate (9:1) to afford a dark solid (77.21mg, 7.11% yield) after dry under vacuum.

To a stirring solution of N,N-dimethyl-4-((trimethysilyl)ethynyl)aniline (77 mg, 0.35 mmol, 1 equiv) in THF (10 mL), TBAF (0.49 mL, 0.49 mmol, 1.4 equiv) was added dropwise over 4-5 mins. The mixture was kept in the dark monitored by TLC.   After 1.5 h, the reaction was completed. Water (10 mL) was added and the reaction mixture was extracted with dichloromethane (3×25 mL), dried over sodium sulfate and the solvent removed under vacuum.   The reaction mixture was purified by flash chromatography on a silica gel column by eluting with hexanes/ethyl acetate (9:1) to afford a pale yellow solid (40 mg, 78.8% yield) after dry under vacuum. ^{1}H NMR (CDCl$_3$) δ 7.38 – 7.37 (2 H, d, J = 5), 6.64 – 6.62 (2 H, d, J = 10), 2.98 (7 H, s).

1-ethynyl-4-nitrobenzene (3)[38]:

To a stirring solution of 1-iodo-4-nitrobenzene (1 g, 4.01 mmol, 1 equiv) in freshly distilled diisopropylamine (92 mL, 23 mL/mmol), PdCl$_2$(PPh$_3$)$_2$ (281 mg, 0.40 mmol, 0.1 equiv) and CuI (153 mg, 0.80 mmol, 0.2 equiv) were added under nitrogen atmosphere. After 10 min, trimethylsilylacetylene (5.1 mL, 36 mmol, 9 equiv) was added and the reaction mixture was stirred at 55 $^{\circ}$C for one week. The dark mixture was purified by flash chromatography on silica gel by eluting with hexanes/ethyl acetate (9:1) to afford a dark solid (480 mg, 55% yield).

To a stirring solution of trimethyl((4-nitrophenyl)ehynyl)silane (300 mg, 1.37 mmol, 1 equiv) in THF (40 mL), TBAF (2 mL, 1.92 mmol, 1.4 equiv) was added dropwise over 4-5mins. The reaction was kept in the dark and monitored by TLC. After 1.5 h, reaction was completed. Water (50 mL) was added and the mixture was extracted with dichloromethane (3×50 mL), dried over sodium sulfate and the solvent removed *in vacuo*. The reaction mixture was purified by flash chromatography on silica gel by eluting with hexanes/ethyl acetate (9:1) to afford a yellow solid (100 mg, 49.6% yield). ^{1}H NMR (CDCl$_3$) δ 8.22 − 8.20 (2 H, d, *J* = 10), 7.66 − 7.64 (2 H, d, *J* = 10), 3.37 (1 H, s). ^{13}C NMR (CDCl$_3$) δ 147.75, 133.18, 129.12, 123.76, 82.52, 81.81.

N,N-dimethyl-4-((trimethoxysilyl)ethynyl)aniline ***(2)***[30,39]: 4-ethynyl-N,N-dimethylaniline(1) (200 mg, 1.4 mmol, 1 equiv) was dissolved in freshly distilled THF (14 mL, 10 mL/mmol) in a flame dried flask under N$_2$. The mixture was cooled to -10 $^{\circ}$C in ice and acetone. LDA (0.655 mL, 1.31 mmol, 0.95 equiv) was added dropwise while the temperature was maintained and then stirred for 1 h. Chlorotriethyoxysilane (0.412 mL, 2.1 mmol, 1.5 equiv) was added to the reaction mixture, and stirring and cooling were maintained for 2 h upon which the reaction was allowed to warm to room

temperature and stirring maintained overnight. After removing the THF *in vacuo*, anhydrous hexane was added to precipitate the LiCl salts. The hexane was removed *in vacuo* to afford a dark oil. ^{1}H NMR and GC/MS were used to characterize the product. The results showed the majority of product with unclear by-products impurity.

Triethoxy((4-nitrophenyl)ethynyl)silane (4)[39]: 1-ethynyl-4-nitrobenzene(2) (100 mg, 0.68 mmol, 1 equiv) was dissolved in freshly distilled THF (6.8 mL, 10 mL/mmol) in a flame dried flask under N_2. The mixture was cooled to -78°C in dye ice and acetone. nBu-Li (0.258 mL, 0.645 mmol, 0.95 equiv) was added dropwise while the temperature was maintained and then stirred for 1 h. Chlorotriethyoxysilane (0.126 mL, 0.645 mmol, 0.95 equiv) was added to the reaction mixture, and stirring and cooling were maintained for 2 h upon which the reaction was allowed to warm to room temperature and stirring maintained overnight. After removing the THF *in vacuo*, anhydrous hexane was added to precipitate the LiCl salts. The hexane was removed *in vacuo* to afford a dark oil. ^{1}H NMR and GC/MS were used to characterize the product. The results showed the majority of product with unclear by-products impurity.

Synthesis of 3-azidopropyltrimethoxysilane(APTMS)[40,41] :

To a 50 mL two-neck flask, 3-chloropropyltrimethoxysilane (4.5 mL, 24 mmol, 1 equiv) was dissolved in DMF (30 mL) and sodium azide (3.3 g, 48 mmol, 2 equiv) was added. After the reaction mixture was stirred at 100 ^{o}C for 24 h, the solid in the reaction mixture was removed by filtration. The filtrate was concentrated under high vacuum to obtain a clear oil (2.35 g, 47% yield). ^{1}H NMR (CDCl$_3$) δ 3.57 (9 H, m), 3.25 (2 H, m), 1.69 (2 H, m), 0.68 (2 H, m).

E. 3.2 Binding Method

General Rubrene Crystal Sample Preparation (Figure E 12). Rubrene single crystal sample was glued with rubber cement on glass substrate. Then, the electrical contacts have been prepared at the surface of organic crystals by thermal evaporation of silver or application of a thin layer of colloidal graphite.[12] After functionalization of a variety of binding molecules, the crystal sample was put into the chamber for future conductivity measurement. After each functionalization step, the rubrene crystal sample was rinsed several times with neat solvents and air dried.

Functionalization of Head-Linker-Achnor Molecules for doping surfaces. A few drops of concentrated N,N-dimethyl-4-((trimethoxysilyl)ethynyl)aniline **2** or Triethoxy((4-nitrophenyl)ethynyl)silane **4** liquid was deposited on rubrene crystal sample for several hours to days. Then, the conductivity was measured.
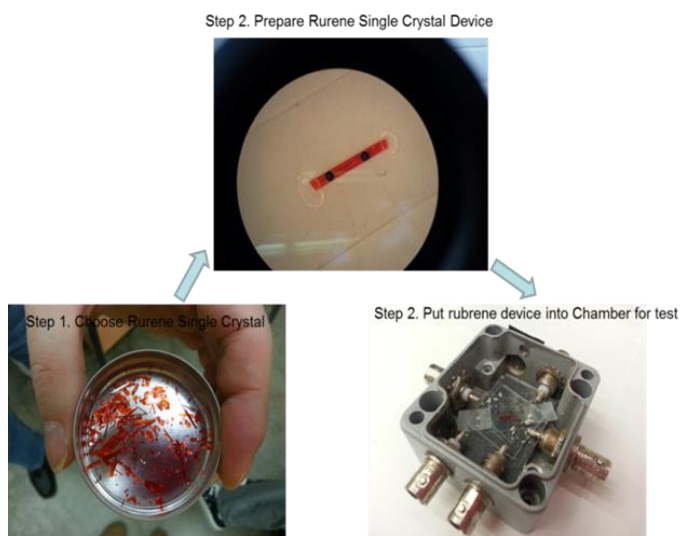
Figure E 12 General Rubrene Crystal Sample Preparation

Functionalization of Rubrene with Bifunctional Linker . Simple vapor deposition method was used to bind (3-bromopropyl)trichlorosilane or 3-

azidopropyltrimethoxysilane bifunctional molecules, as shown below. Briefly, the concentrated bifunctional molecules as SAM solution (3~5ml) was stored in a beak and left in a sealed glass chamber with rubrene crystal samples taped on the top of chamber, as showed in Figure E 13. The typical binding times ranged from several hours to several days and the temperature ranged from room temperature to 80°C.
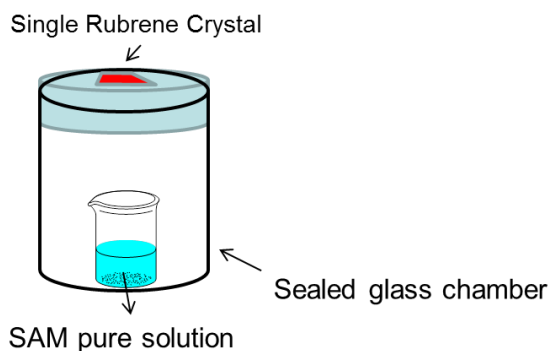
Figure E 13 Experiment set up for functionalization of rubrene single crystal

The azide exchange with (3-bromopropyl)trichlorosilnae functionalized rubrene crystal samples was carried out by immersing the crystal samples into a saturated sodium azide solution in ultra-pure water for several hours to days, while monitoring the conductivity.

Functionalization of Rubrene with diazonium salts as anchor group. The rubrene crystal samples were immersed into 50mM 4-Bromobenzenediazonium tetrafluoroborate salt solution in ultra-pure water. The typical binding time ranged from several hours to days.

E.4 Conclusion

We proposed to create functional layers at the surface of rubrene single crystals. We bind HLA molecular monolayers comprising a head group, a linker, and an anchor. The anchor will form the covalent bond with the surface. The linker will serve as a simple spacer. The head group will consist of a small group with withdraws or donates electrons, or a desired functional group via secondary click chemistry. With N,N-dimethyl aniline as electron donors and nitro as acceptors, the results were not satisfactory. The azide functional group was successfully introduced on rubrene crystal surface through substitution with bromine. The conductivity increased and a decrease of carrier mobility was observed with larger surface coverage. The characterization measurements, including XPS, are currently being investigated to study the properties of the functional layers. Meanwhile, aryl diazonium salts were successfully employed instead of silanes for binding to rubrene crystal surfaces leading to conductivity changes after deposition.

E.5 References

(1)   Forrest, S. R. *Nature* **2004**, *428*, 911.

(2)   Bässler, H.; Köhler, A. **2011**, *312*, 1.

(3)   Yang, Y. S.; Yasuda, T.; Kakizoe, H.; Mieno, H.; Kino, H.; Tateyama, Y.; Adachi, C. *Chemical Communications* **2013**, *49*, 6483.

(4)   M. Pope and C. E. Swenber, Electronic Processes in Organic Crystals and Polymers, 2nd ed. (Oxford University Press, New York, London, 1999).

(5)   Organic Filed-Effect Transistors, (Eds: Z. Bao, J. Locklin), Taylor & Francis, Boca Raton, London, New York 2007.

(6)   Podzorov, V.; Pudalov, V. M.; Gershenson, M. E. *Applied Physics Letters* **2003**, *82*, 1739.

(7)   Podzorov, V.; Sysoev, S. E.; Loginova, E.; Pudalov, V. M.; Gershenson, M. E. *Applied Physics Letters* **2003**, *83*, 3504.

(8)   Briseno, A. L.; Mannsfeld, S. C. B.; Ling, M. M.; Liu, S.; Tseng, R. J.; Reese, C.; Roberts, M. E.; Yang, Y.; Wudl, F.; Bao, Z. *Nature* **2006**, *444*, 913.

(9)   Podzorov, V.; Menard, E.; Rogers, J. A.; Gershenson, M. E. *Physical Review Letters* **2005**, *95*, 226601.

(10)   Haas, S.; Stassen, A. F.; Schuck, G.; Pernstich, K. P.; Gundlach, D. J.; Batlogg, B.; Berens, U.; Kirner, H. J. *Physical Review B* **2007**, *76*, 115203.

(11)   Kloc, C.; Simpkins, P. G.; Siegrist, T.; Laudise, R. A. *Journal of Crystal Growth* **1997**, *182*, 416.

(12)   de Boer, R. W. I.; Gershenson, M. E.; Morpurgo, A. F.; Podzorov, V. *physica status solidi (a)* **2004**, *201*, 1302.

(13)   Dabestani, R.; Nelson, M.; Sigman, M. E. *Photochemistry and Photobiology* **1996**, *64*, 80.

(14)   Ellison, D. J.; Lee, B.; Podzorov, V.; Frisbie, C. D. *Advanced Materials* **2011**, *23*, 502.

(15)   Boudinet, D.; Benwadih, M.; Altazin, S.; Verilhac, J.-M.; De Vito, E.; Serbutoviez, C.; Horowitz, G.; Facchetti, A. *Journal of the American Chemical Society* **2011**, *133*, 9968.

(16)   Hoogboom, J.; Garcia, P. M. L.; Otten, M. B. J.; Elemans, J. A. A. W.; Sly, J.; Lazarenko, S. V.; Rasing, T.; Rowan, A. E.; Nolte, R. J. M. *Journal of the American Chemical Society* **2005**, *127*, 11047.

(17)   Wang, B.; Haick, H. *ACS applied materials & interfaces* **2013**, *5*, 2289.

(18)   Calhoun, M. F.; Sanchez, J.; Olaya, D.; Gershenson, M. E.; Podzorov, V. *Nature Materials* **2007**, *7*, 84.

(19)   Sagiv, J. *Journal of the American Chemical Society* **1980**, *102*, 92.

(20)   Michalak, D. J.; Rivillon, S.; Chabal, Y. J.; Estève, A.; Lewis, N. S. *The Journal of Physical Chemistry B* **2006**, *110*, 20426.

(21)   Kulkarni, S. A.; Vijayamohanan, K. P. *Surface Science* **2007**, *601*, 2983.

(22)   Dong, J.; Wang, A.; Ng, K. Y. S.; Mao, G. *Thin Solid Films* **2006**, *515*, 2116.

(23)   Wen, K.; Maoz, R.; Cohen, H.; Sagiv, J.; Gibaud, A.; Desert, A.; Ocko, B. M. *ACS nano* **2008**, *2*, 579.

(24)   Melissa A. Stokes, An In-situ Study of Organic Semiconductor Thin Films for Gas Sensing, A dissertation thesis

(25)   Sugimura, H.; Hayashi, K.; Saito, N.; Nakagiri, N.; Takai, O. *Applied Surface Science* **2002**, *188*, 403.

(26)   Wang, H.; Xu, X.; Li, L.; Carroll, P. J.; Ji, H.-F. *Analytical Chemistry Letters* **2011**, *1*, 158.

(27)   Mahouche-Chergui, S.; Gam-Derouich, S.; Mangeney, C.; Chehimi, M. M. *Chemical Society reviews* **2011**, *40*, 4143.

(28)   Bahr, J. L.; Yang, J.; Kosynkin, D. V.; Bronikowski, M. J.; Smalley, R. E.; Tour, J. M. *Journal of the American Chemical Society* **2001**, *123*, 6536.

(29)   Abdula, D.; Nguyen, K. T.; Shim, M. *The Journal of Physical Chemistry C* **2007**, *111*, 17755.

(30)   Goettmann, F.; Boissière, C.; Grosso, D.; Mercier, F.; Le Floch, P.; Sanchez, C. *Chemistry – A European Journal* **2005**, *11*, 7416.

(31)   Lieber, E.; Rao, C. N. R.; Chao, T. S.; Hoffman, C. W. W. *Anal. Chem.* **1957**, *29*, 916.

(32)   S. M. Sze and K. K. N, Physics of Semiconductor Devices, John Wiley & Sons, Inc., New Jersey, 3rd edn, 2007

(33)   Chen, Y.; Lee, B.; Yi, H. T.; Lee, S. S.; Payne, M. M.; Pola, S.; Kuo, C. H.; Loo, Y. L.; Anthony, J. E.; Tao, Y. T.; Podzorov, V. *Physical Chemistry Chemical Physics* **2012**, *14*, 14142.

(34)   Xie, W.; Prabhumirashi, P. L.; Nakayama, Y.; McGarry, K. A.; Geier, M. L.; Uragami, Y.; Mase, K.; Douglas, C. J.; Ishii, H.; Hersam, M. C.; Frisbie, C. D. *ACS nano* **2013**, *7*, 10245.

(35)   Sun, Z.; Pint, C. L.; Marcano, D. C.; Zhang, C.; Yao, J.; Ruan, G.; Yan, Z.; Zhu, Y.; Hauge, R. H.; Tour, J. M. *Nature Communications* **2011**, *2*, 559.

(36)   Paulus, G. L. C.; Wang, Q. H.; Strano, M. S. *Accounts of Chemical Research* **2013**, *46*, 160.

(37)   Jian, H.; Tour, J. M. *The Journal of Organic Chemistry* **2003**, *68*, 5091.

(38)   Stein, M.; Berger, R.; Seichter, W.; Hulliger, J.; Weber, E. *Journal of Fluorine Chemistry* **2012**, *135*, 231.

(39)   Maskus, M.; Abruña, H. D. *Langmuir : the ACS journal of surfaces and colloids* **1996**, *12*, 4455.

(40)   Meng, D.; Sun, J.; Jiang, S.; Zeng, Y.; Li, Y.; Yan, S.; Geng, J.; Huang, Y. *Journal of Materials Chemistry* **2012**, *22*, 21583.

(41)   Paoprasert, P.; Spalenka, J. W.; Peterson, D. L.; Ruther, R. E.; Hamers, R. J.; Evans, P. G.; Gopalan, P. *Journal of Materials Chemistry* **2010**, *20*, 2651.

Appendix: ^{1}H and ^{13}C NMR spectra

^{1}H NMR (CDCl$_3$)

PDHA

^{13}C NMR (CDCl$_3$)

^{1}H NMR (CDCl$_3$)

Br—(CH$_2$)$_{10}$—COOMe

Methyl 11-azidoundecanoate

7.27

3.66
3.41
3.39
3.38

2.31
2.29
2.28
1.85
1.84
1.82
1.62
1.61
1.59
1.42
1.41
1.39
1.28

1.00
0.70

0.74
0.70
0.78
0.75
3.93

f1 (ppm)

^{13}C NMR (CDCl$_3$)

Methyl 11-azidoundecanoate 13C in DCM

174.18

77.47
77.22 CDCl3
76.96

51.41

34.08
33.94
32.86
29.39
29.34
29.23
29.14
28.76
28.18
24.95

^{1}H NMR (CDCl$_3$)

$N_3-(CH_2)_{10}-COOMe$

Methyl 11-azidoundecanoate 1H CDCl3

3.65

3.26
3.24
3.23

2.31
2.29
2.28

1.62
1.61
1.60
1.58
1.57
1.55

1.37
1.35
1.33
1.28

1.49 1.00 1.08 2.20 6.87

f1 (ppm)

^{13}C NMR (CDCl$_3$)

Methyl 11-azidoundecanoate 13C CDCl3

174.15

77.48
77.24
76.97

51.35
51.30

33.95
29.28
29.20
29.09
28.99
28.72
26.59
26.01
24.82

f1 (ppm)

^{1}H NMR (CDCl$_3$)

1-trimethylsilyethynylpyrene 1H CDCl3

8.59
8.58
8.24
8.23
8.21
8.20
8.18
8.17
8.15
8.11
8.09
8.05
8.04
8.03
8.02
7.27 CDCl3
1.56 HDO
0.42
0.40

TMS
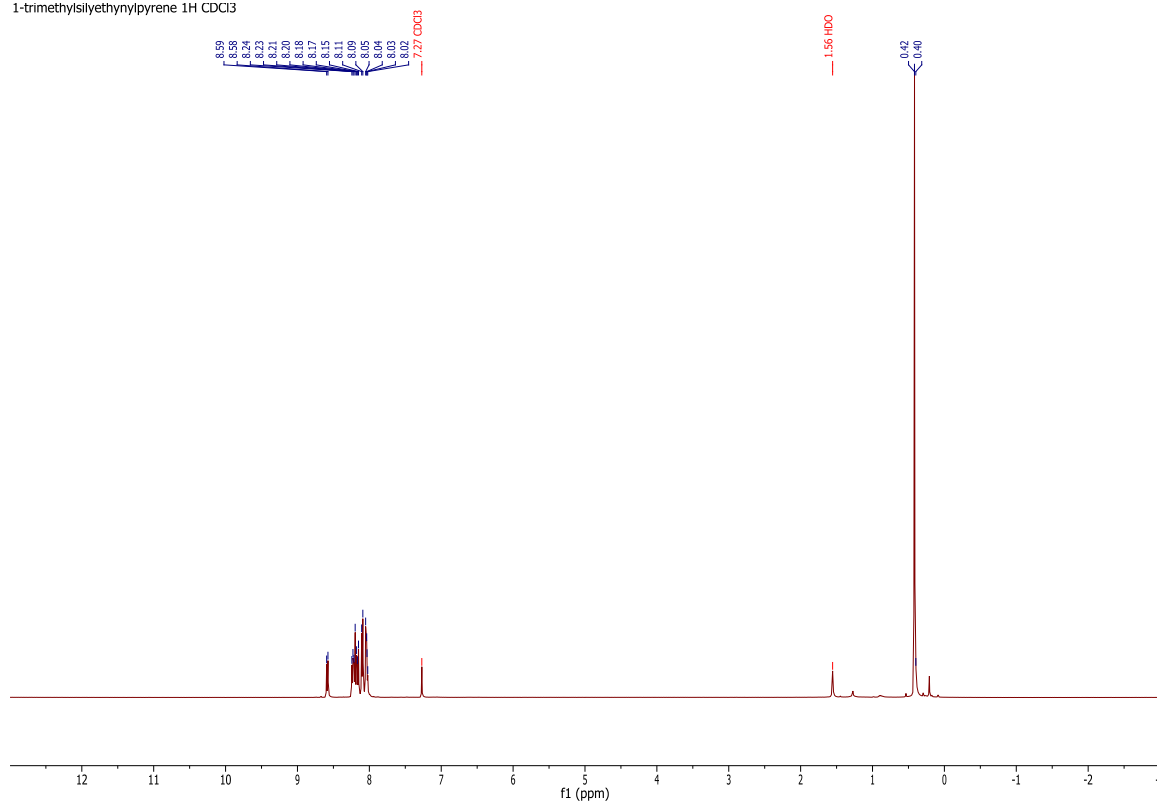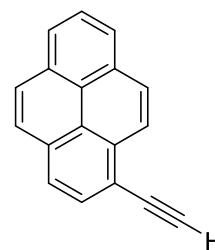
^{1}H NMR (CDCl$_3$)

1-Ethynylpyrene 1H CDCl3
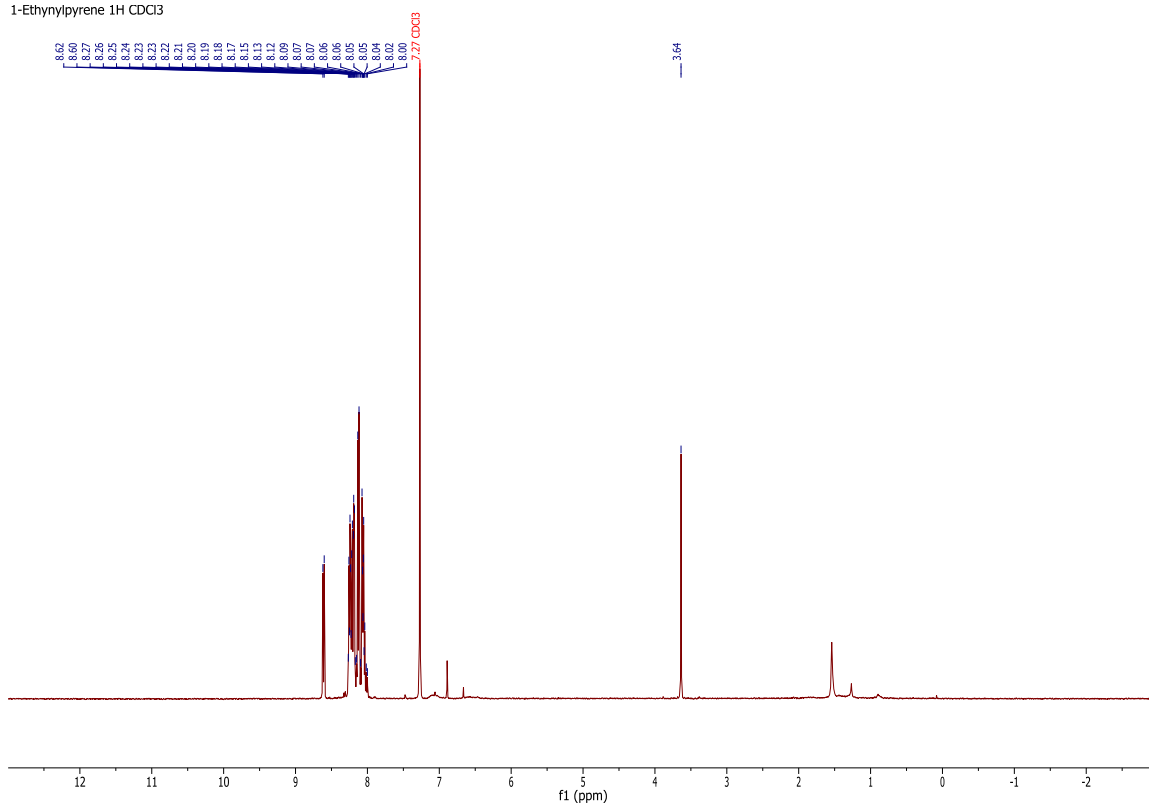
^{13}C NMR (CDCl$_3$)

1-Ethynylpyrene 13C CDCl3

132.71
131.81
131.40
131.21
130.36
128.76
128.61
127.39
126.49
125.94
125.89
125.52
124.58
124.42

116.73

82.96
82.80
82.79

77.48 CDCl3
77.43 CDCl3
77.22 CDCl3
76.97 CDCl3

f1 (ppm)

^{1}H NMR (CDCl$_3$)

Methyl 11-(4-(pyren-1-yl)-1H-1,2,3-triazole-1-yl)undecanoate
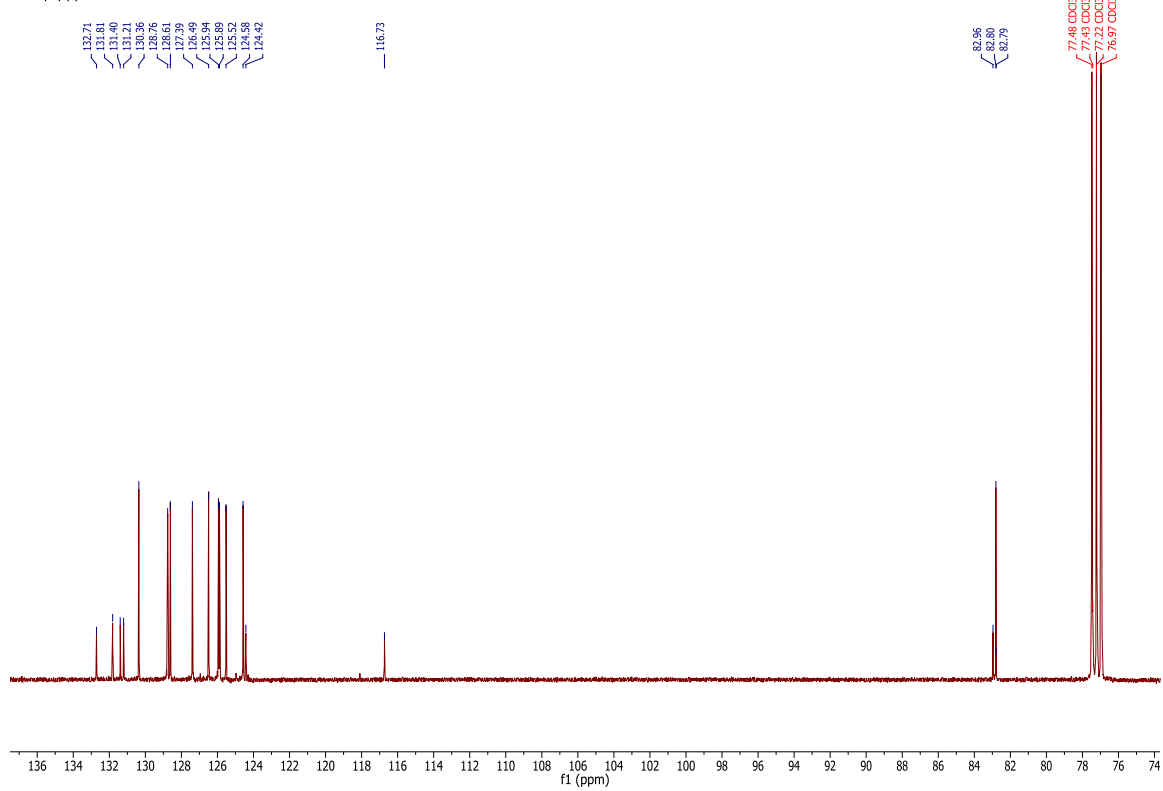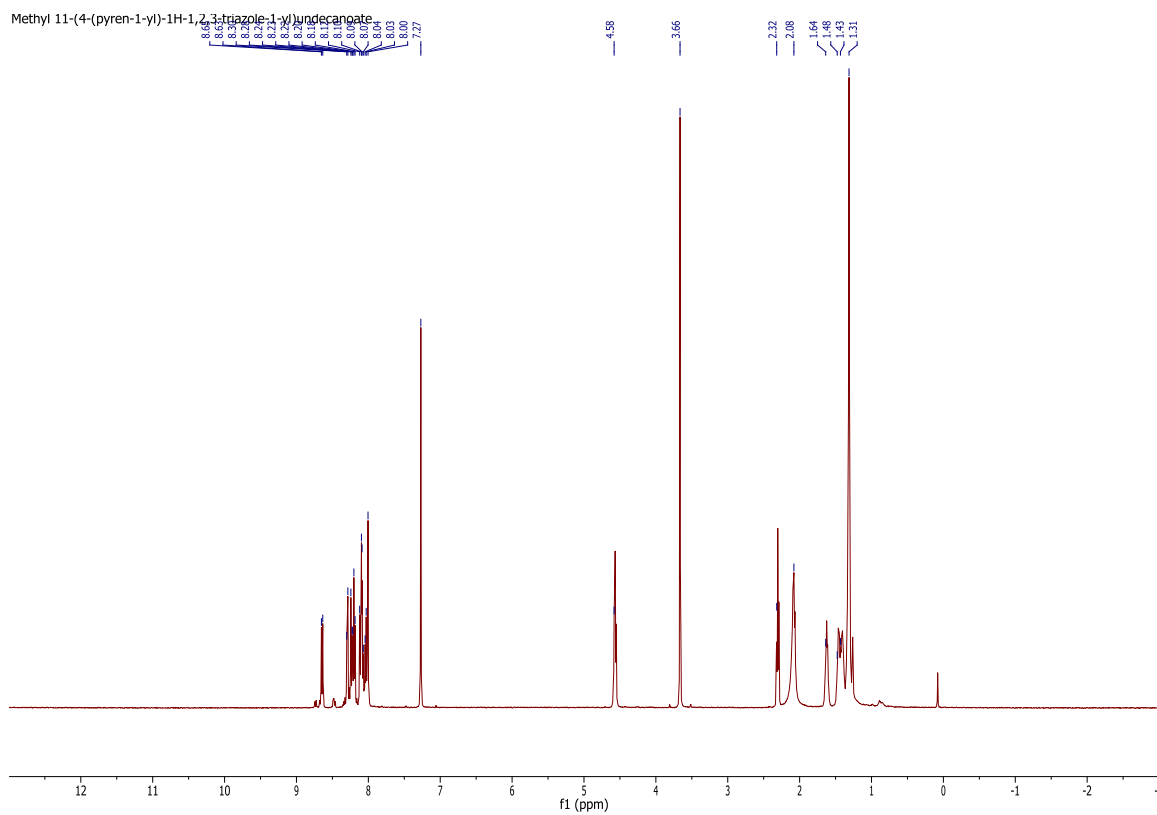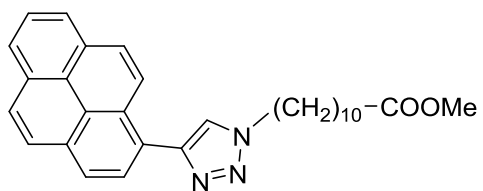
¹³C NMR (CDCl₃)

Methyl 11-(4-(pyren-1-yl)-1H-1,2,3-triazole-1-yl)undecanoate 13C CDCl3

¹H NMR (CDCl₃)
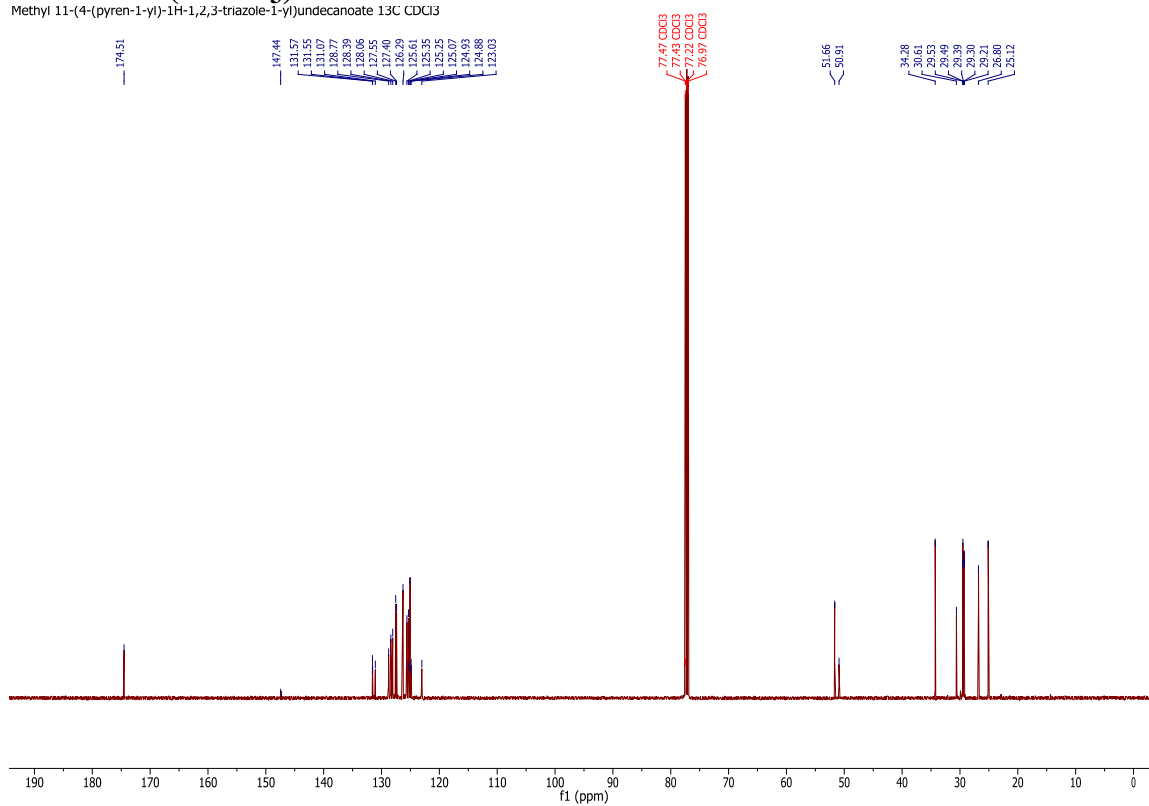
11-(4-(Pyren-1-yl)-1H-1,2,3-triazole-1-yl) undecanoic acid, 1H CDCl3

^{1}H NMR (CDCl$_3$)

N_3—$(CH_2)_{10}$—COOH

11-Azidodecanoic acid 1H CDCl3
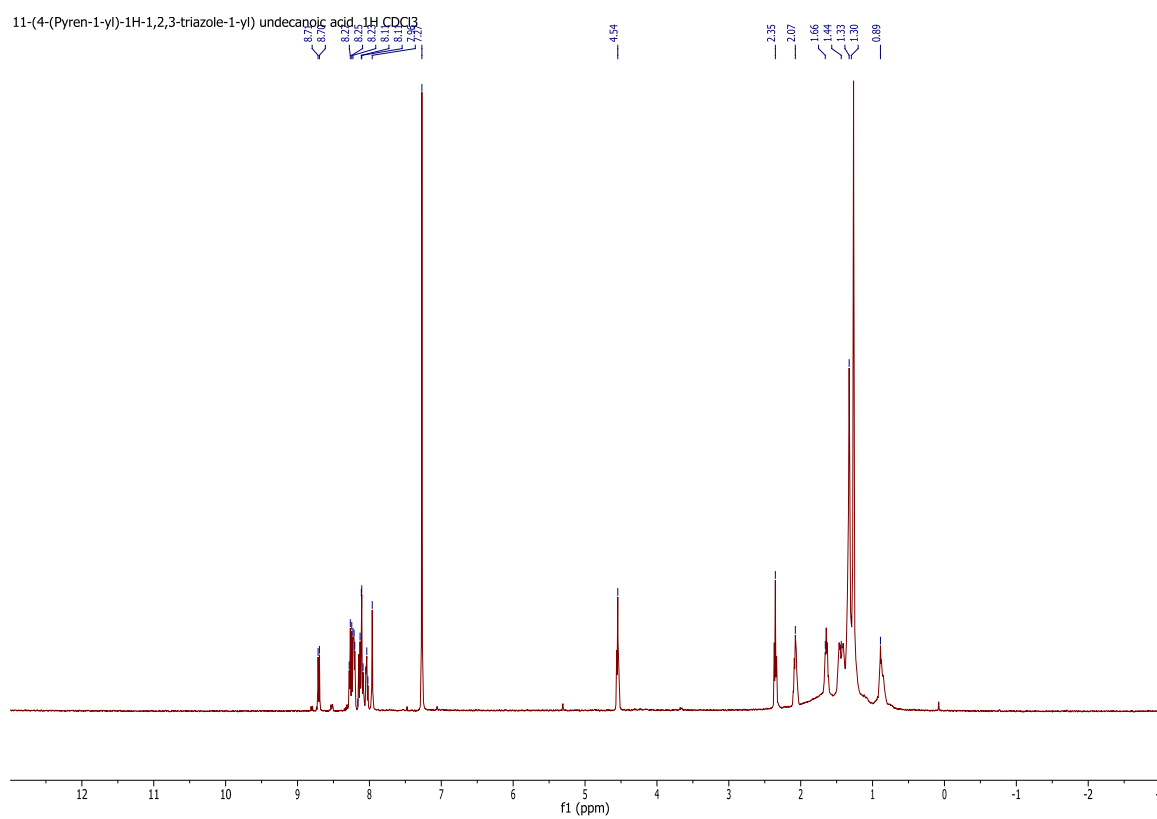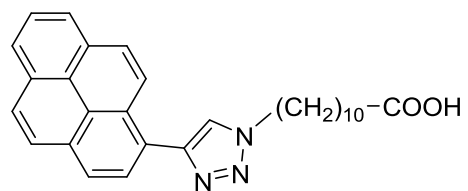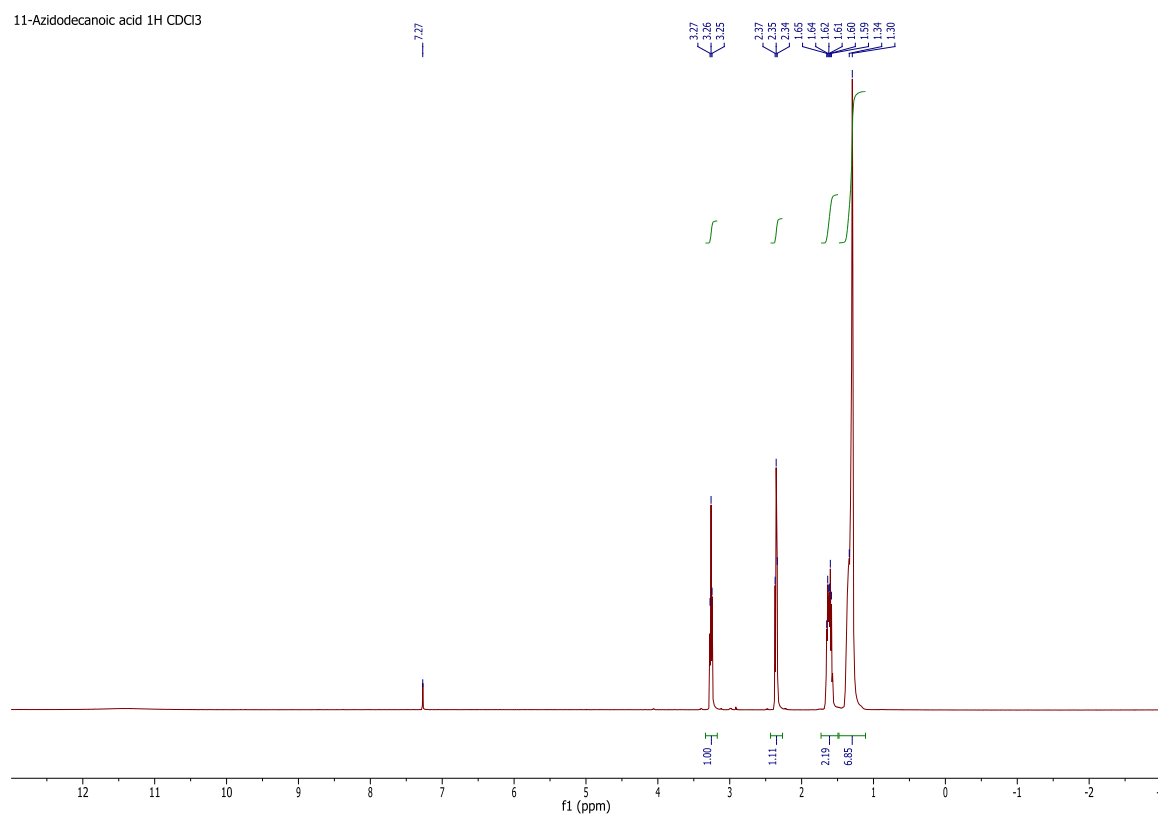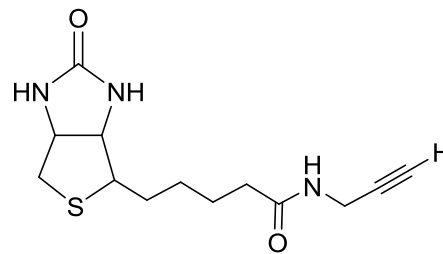
^{1}H NMR (CDCl$_3$)

Alkynated Biotin 1H CDCl3
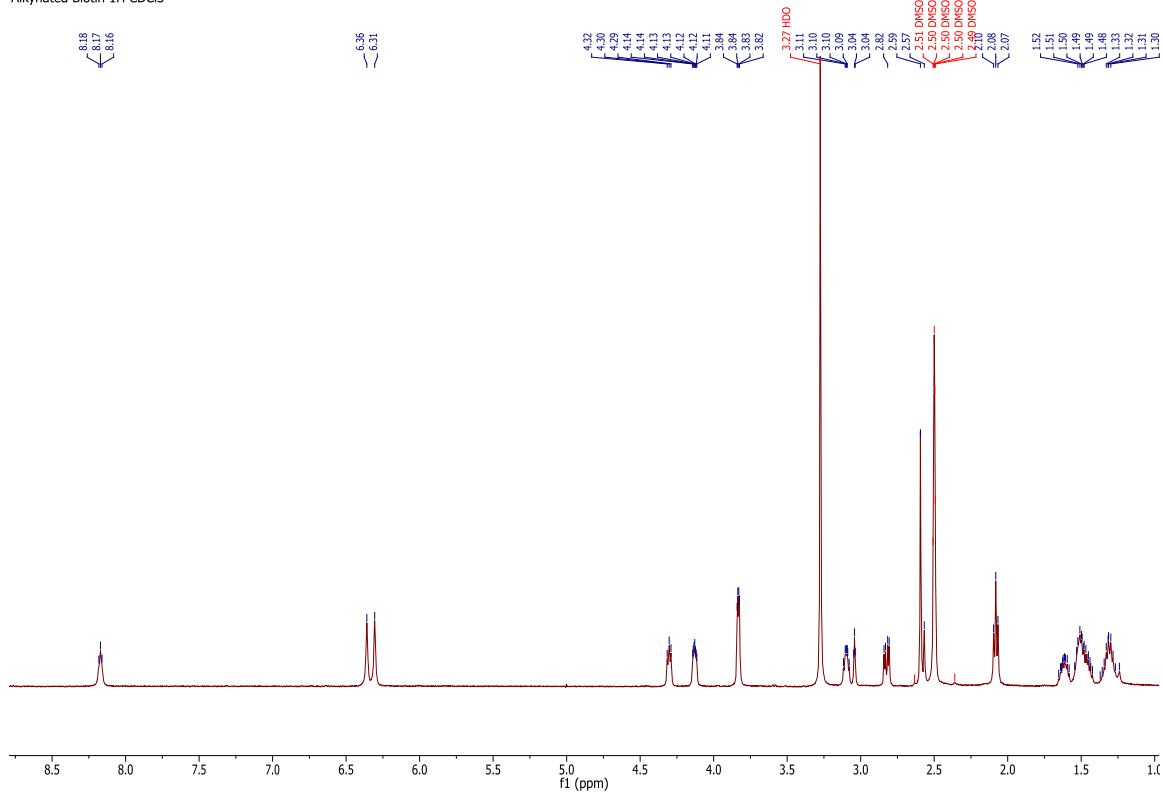
¹H NMR (CDCl₃)
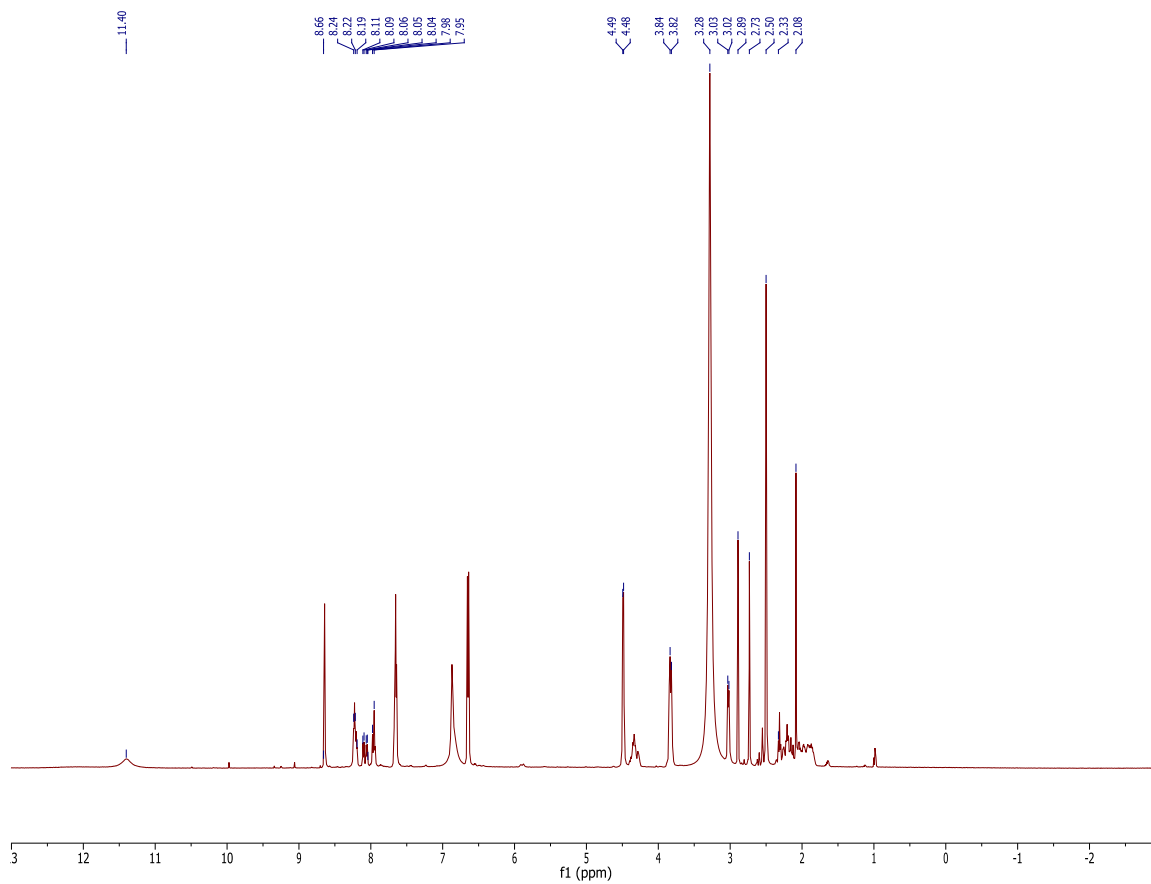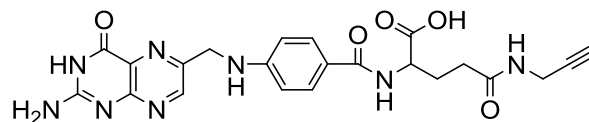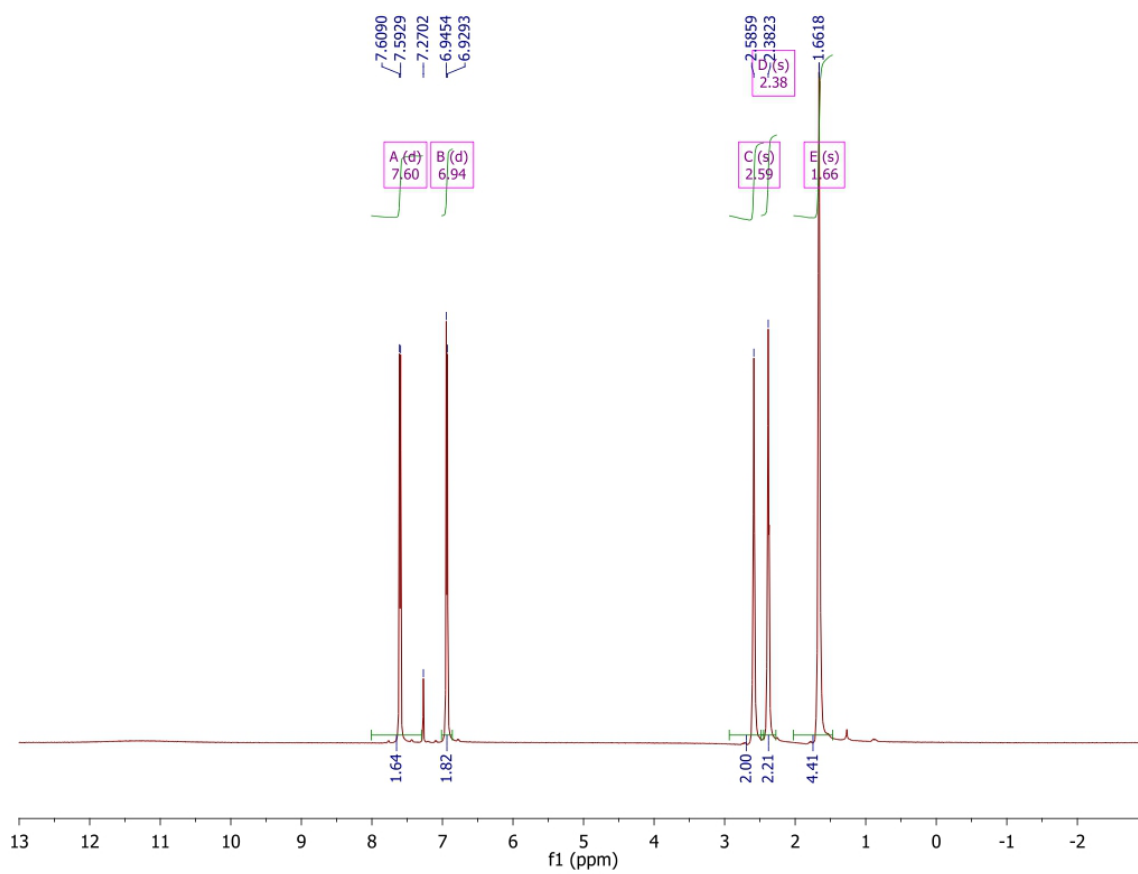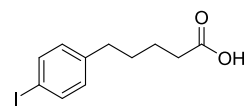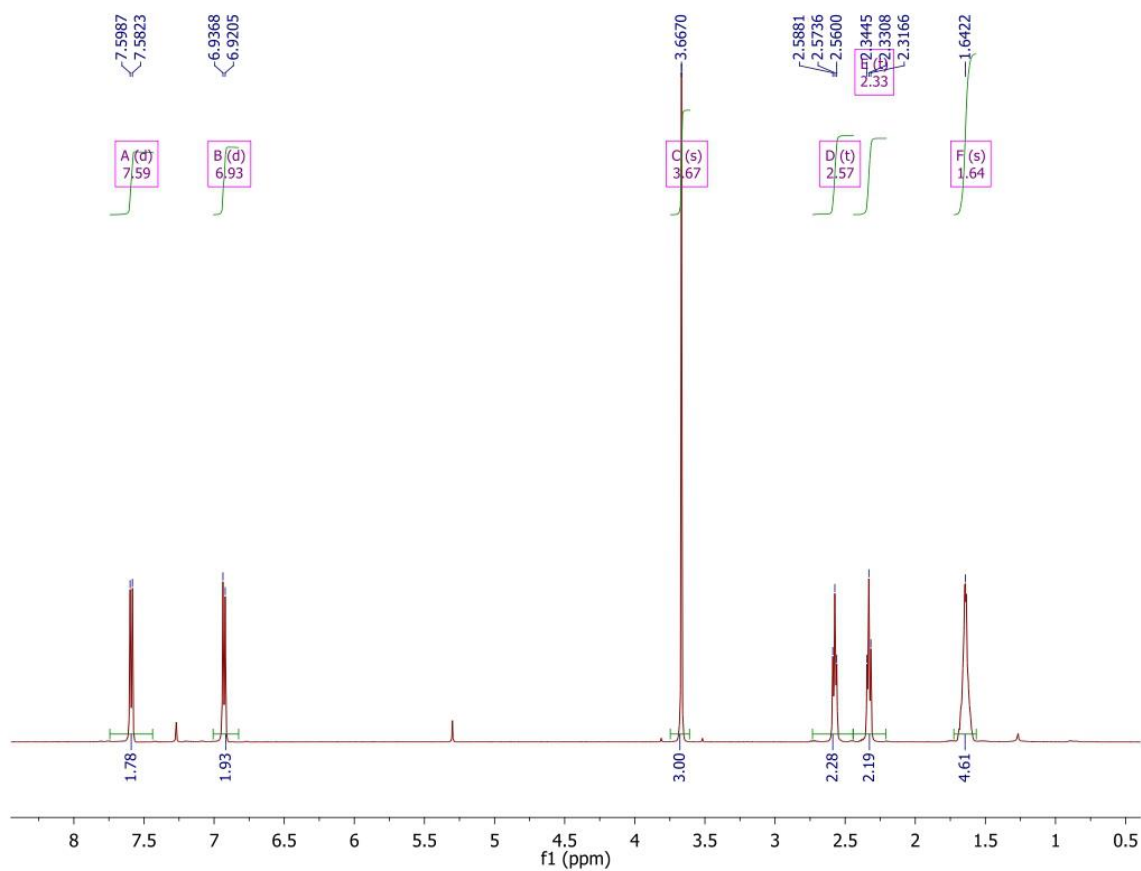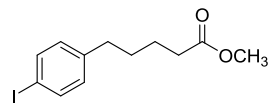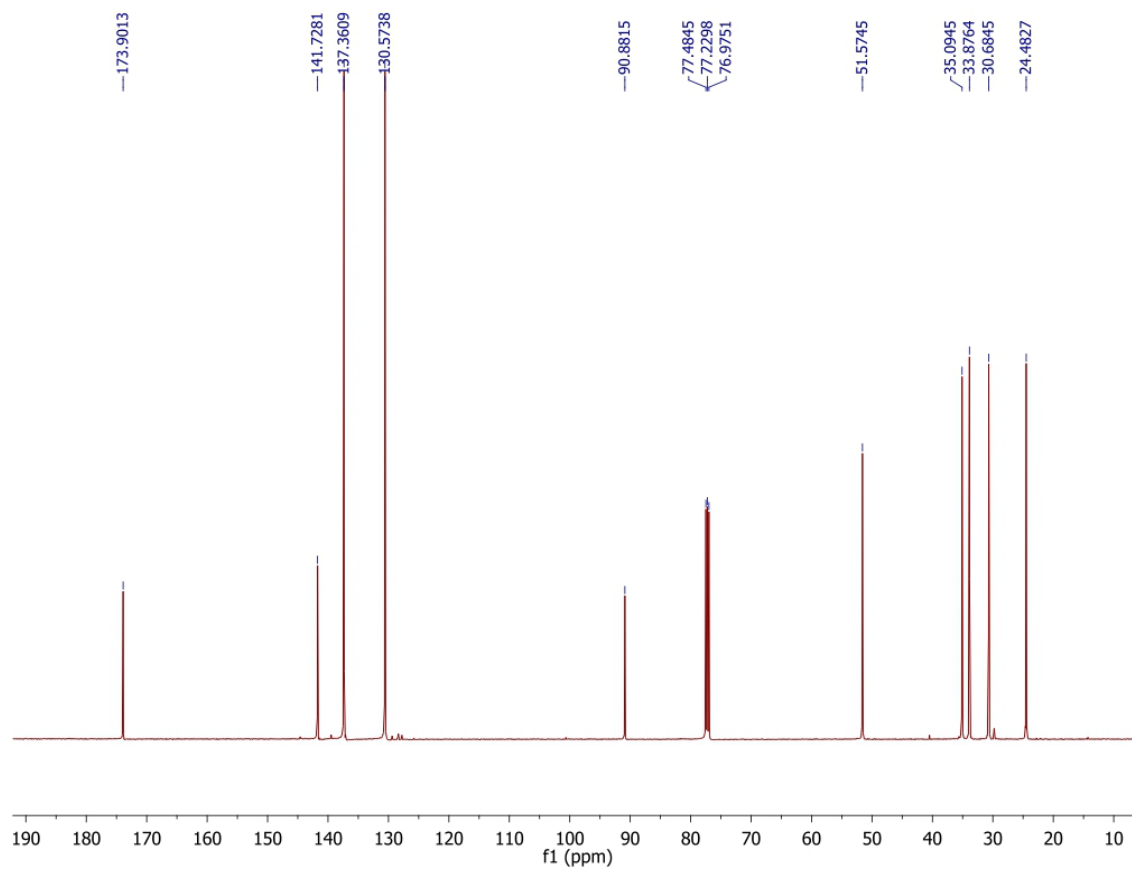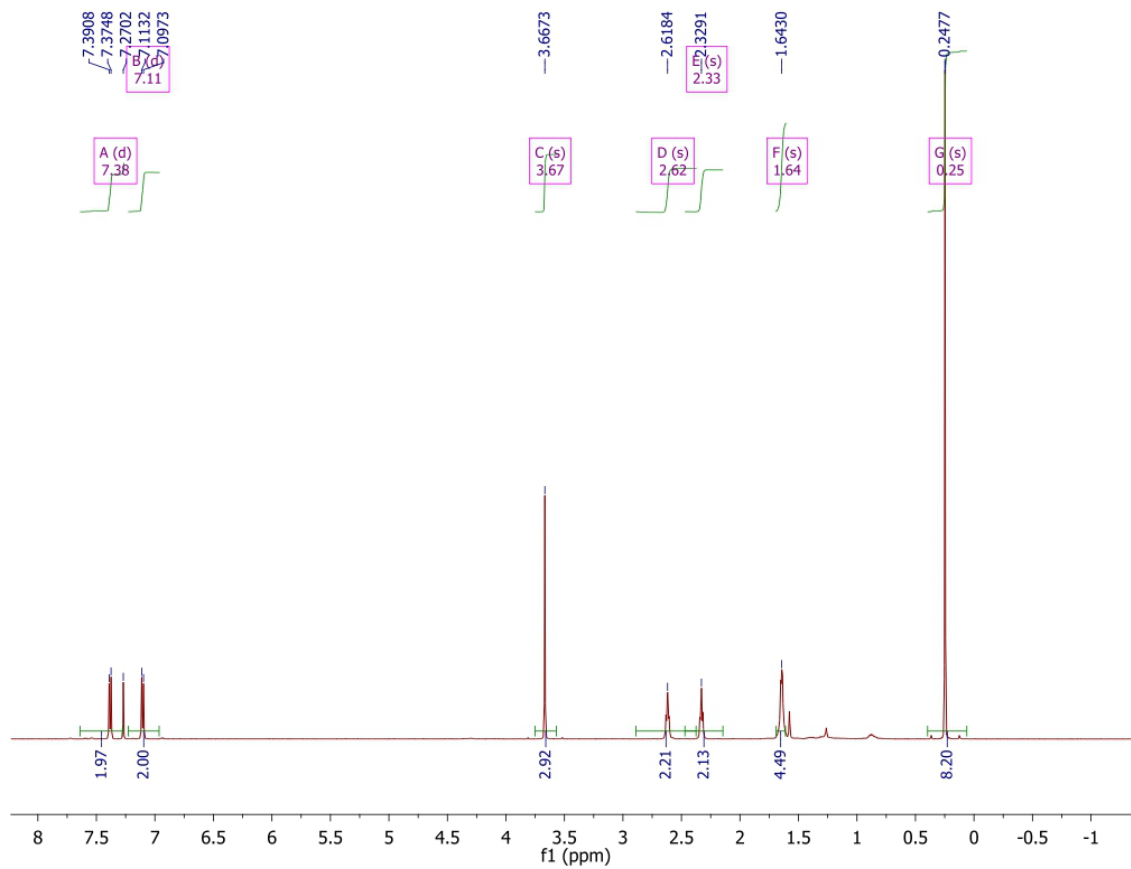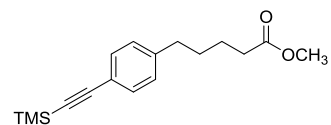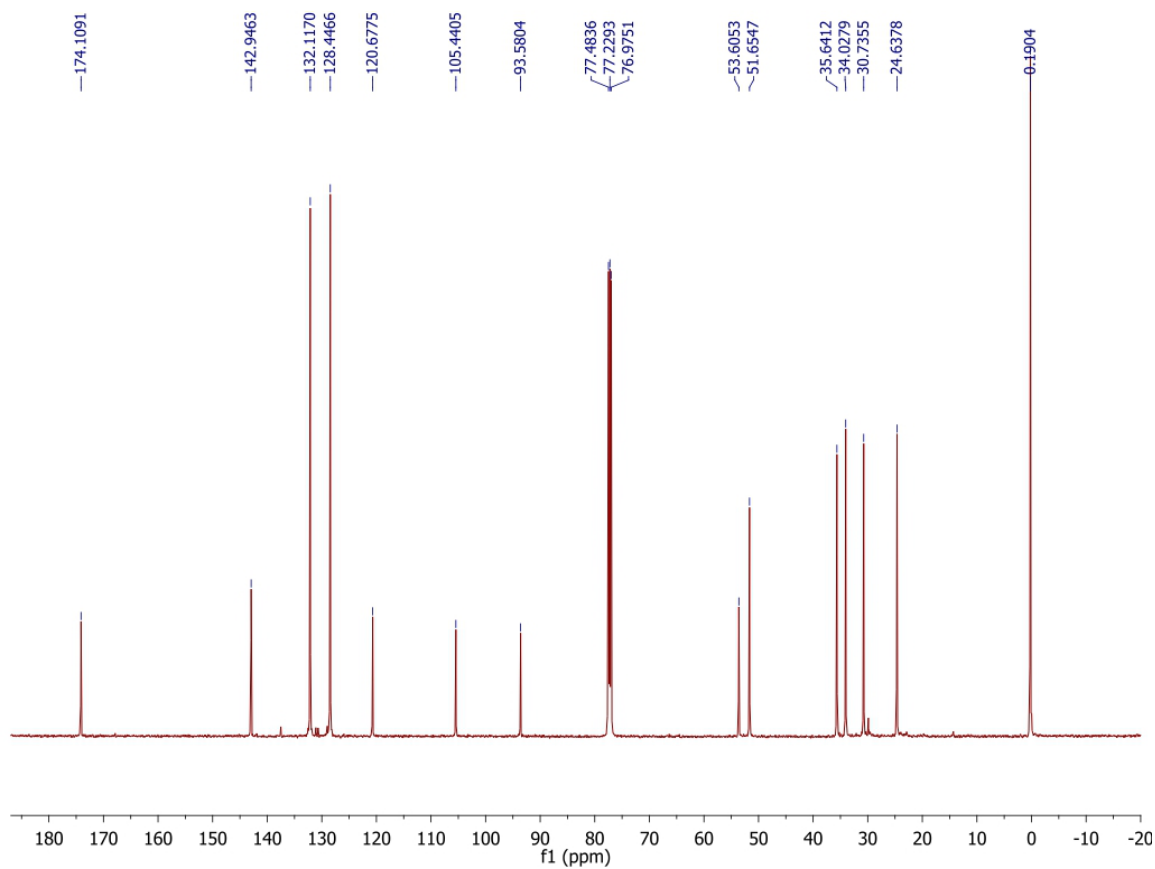
^{1}H NMR (CDCl$_3$)

7.6090
7.5929
7.2702
6.9454
6.9293

2.5859
2.3823
D (s)
2.38

1.6618

A (d)
7.60

B (d)
6.94

C (s)
2.59

E (s)
1.66

1.64

1.82

2.00

2.21

4.41

13 12 11 10 9 8 7 6 5 4 3 2 1 0 -1 -2
f1 (ppm)

^{1}H NMR (CDCl$_3$)

¹³C NMR (CDCl₃)

^{1}H NMR (CDCl$_3$)

A (d) 7.38
B (d) 7.11
C (s) 3.67
D (s) 2.62
E (s) 2.33
F (s) 1.64
G (s) 0.25

7.3908
7.3748
7.2702
7.1132
7.0973
3.6673
2.6184
2.3291
1.6430
0.2477

1.97
2.00
2.92
2.21
2.13
4.49
8.20

f1 (ppm)

^{13}C NMR (CDCl$_3$)

^{1}H NMR (CDCl$_3$)

^{13}C NMR (CDCl$_3$)

¹H NMR (CDCl₃)

¹H NMR (CDCl3)

¹³C NMR (CDCl₃)

¹H NMR (CDCl₃)

7.38
7.37

6.64
6.62

2.99

1.00

1.13

3.82

f1 (ppm)
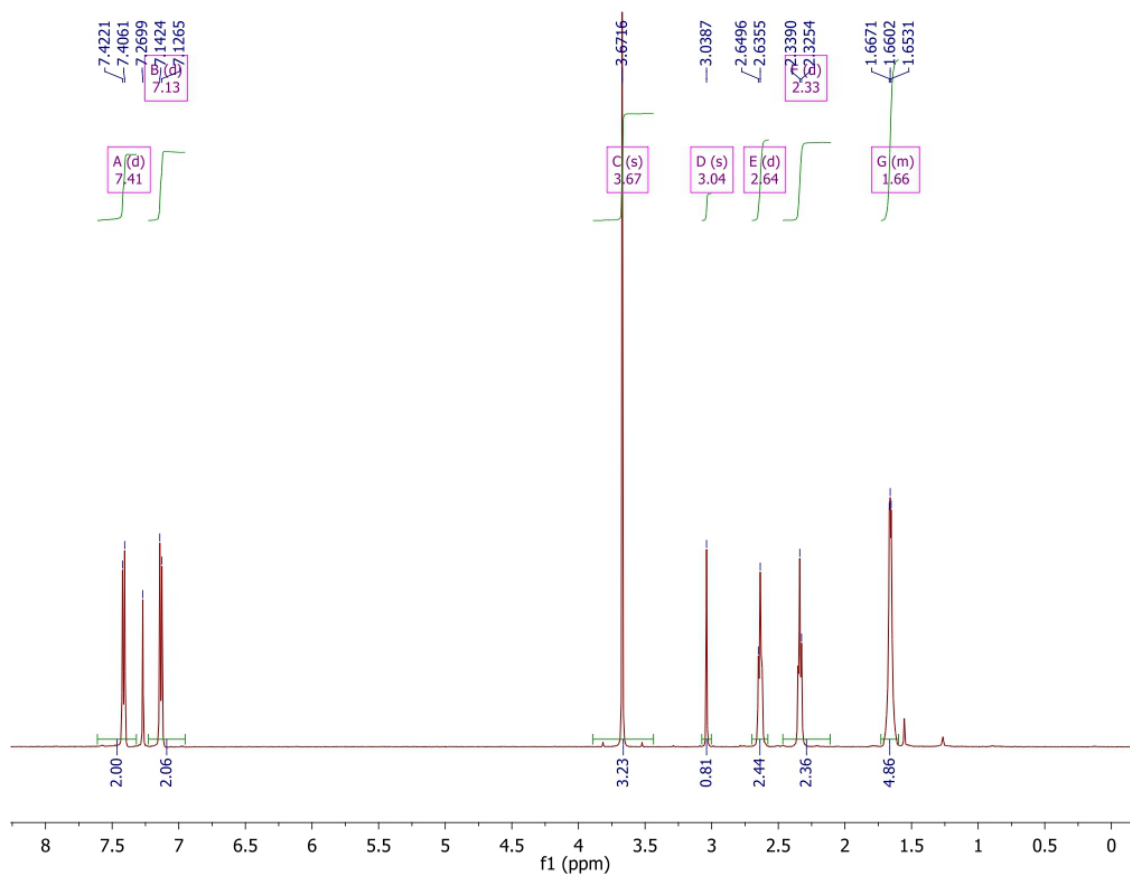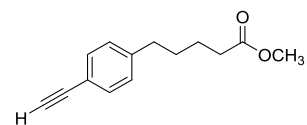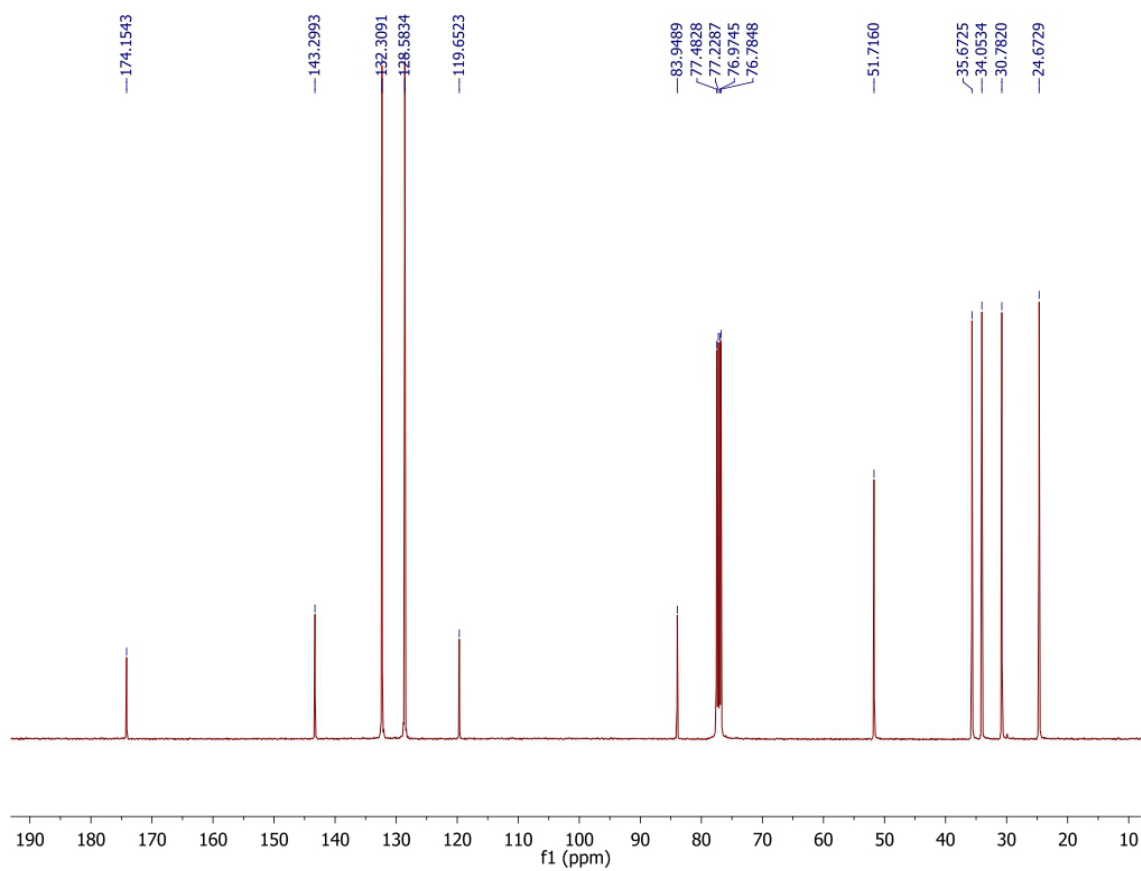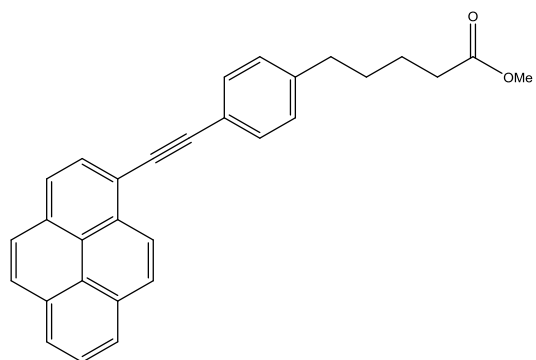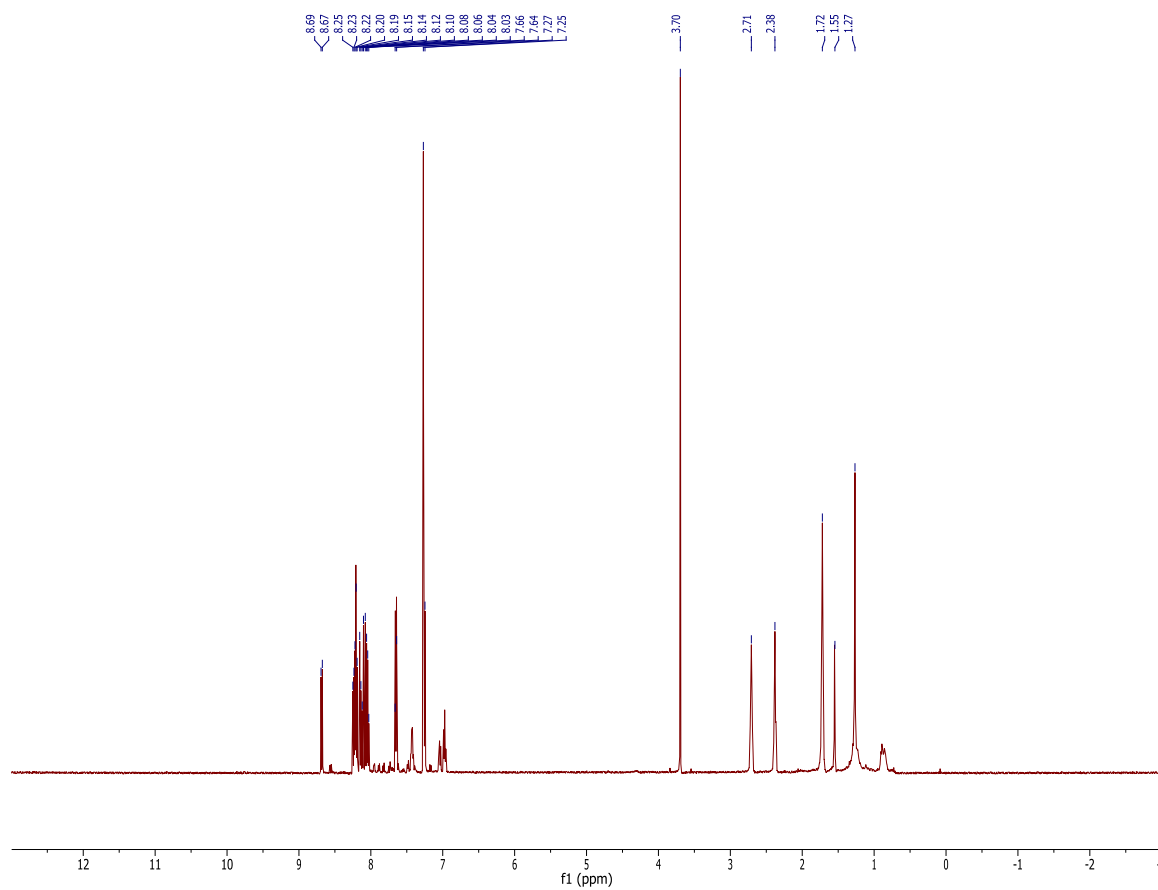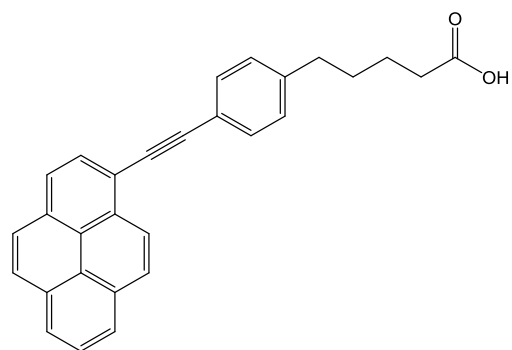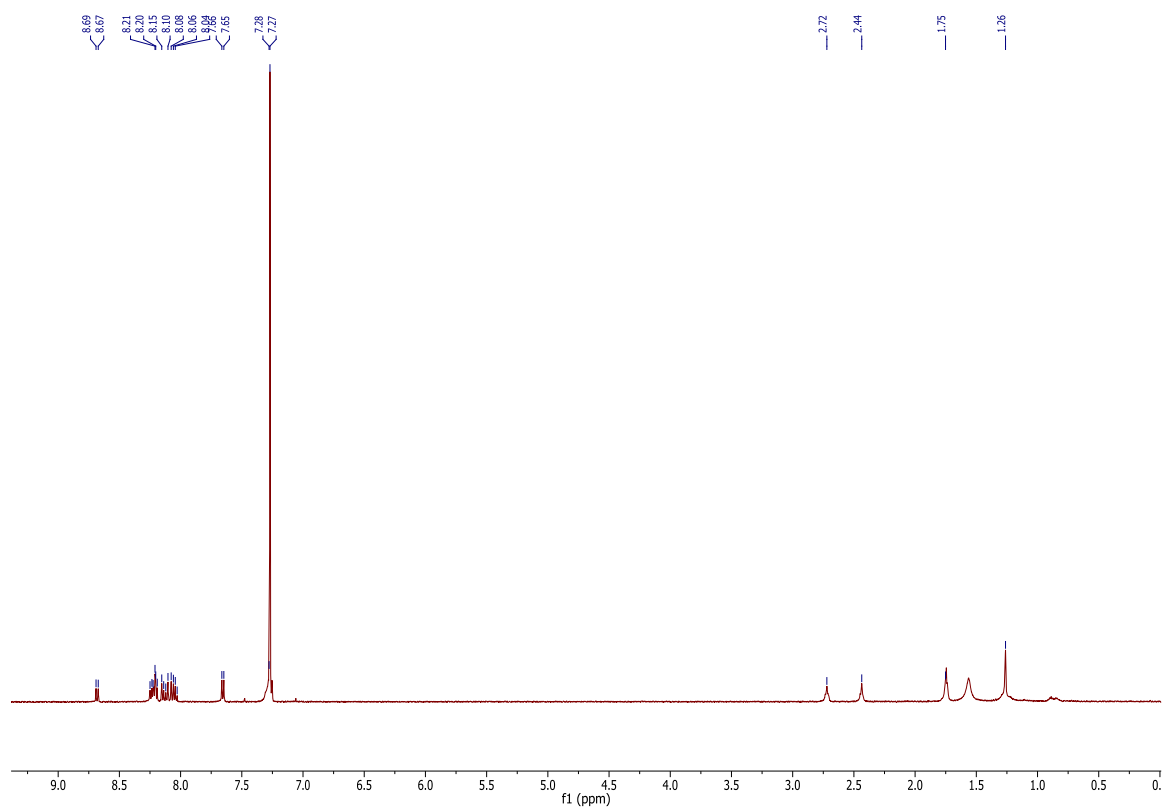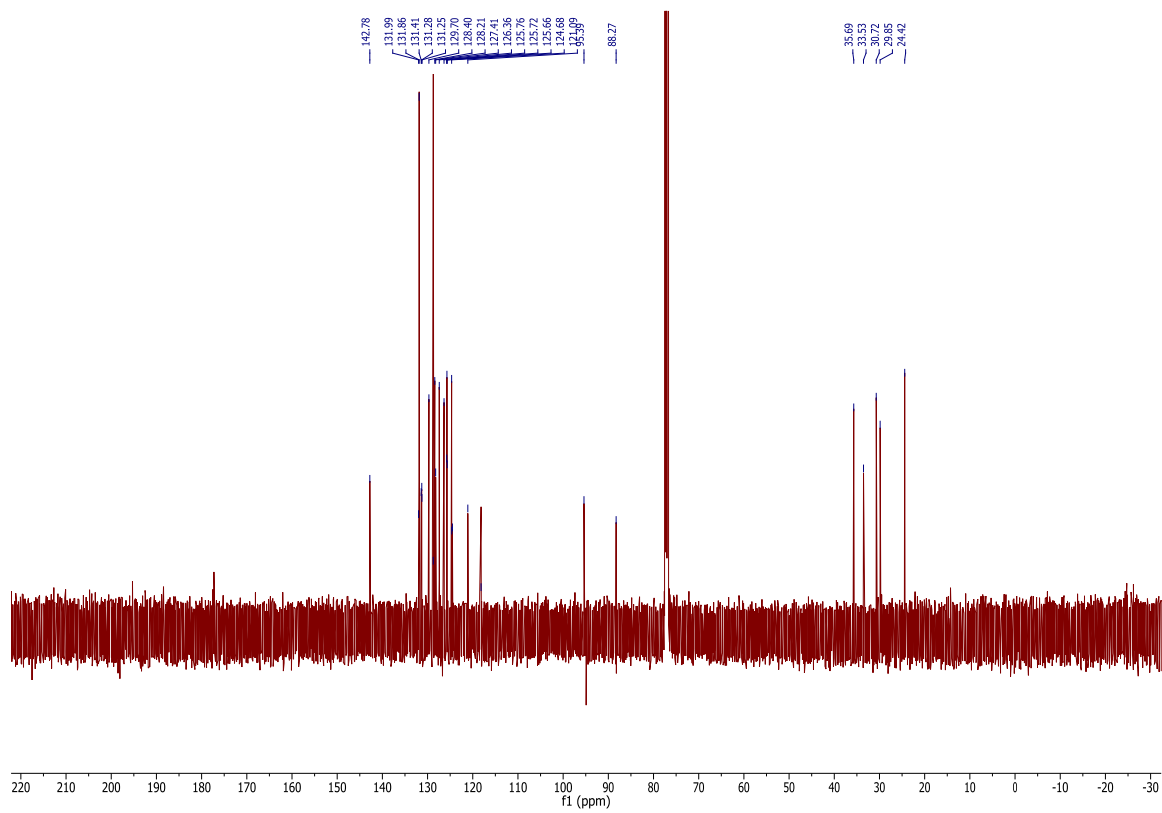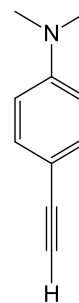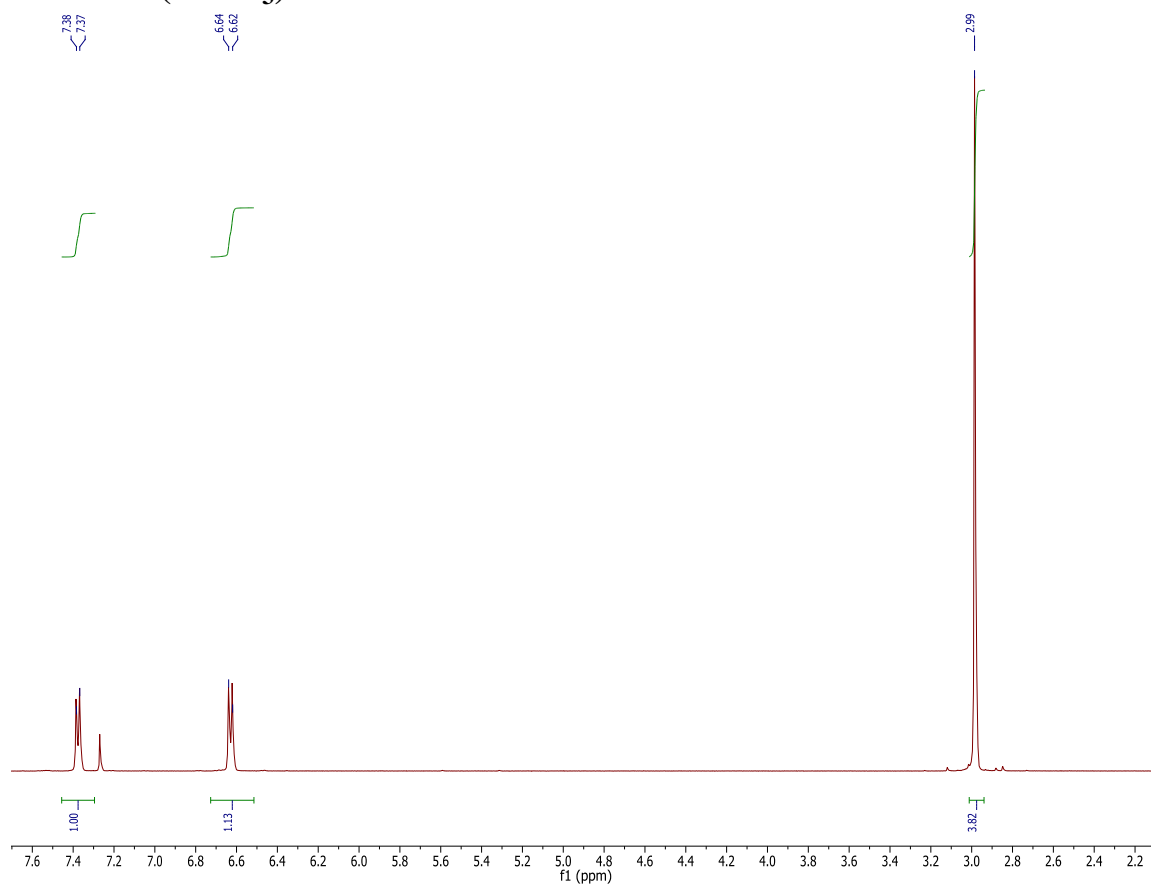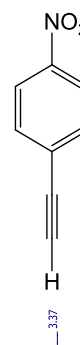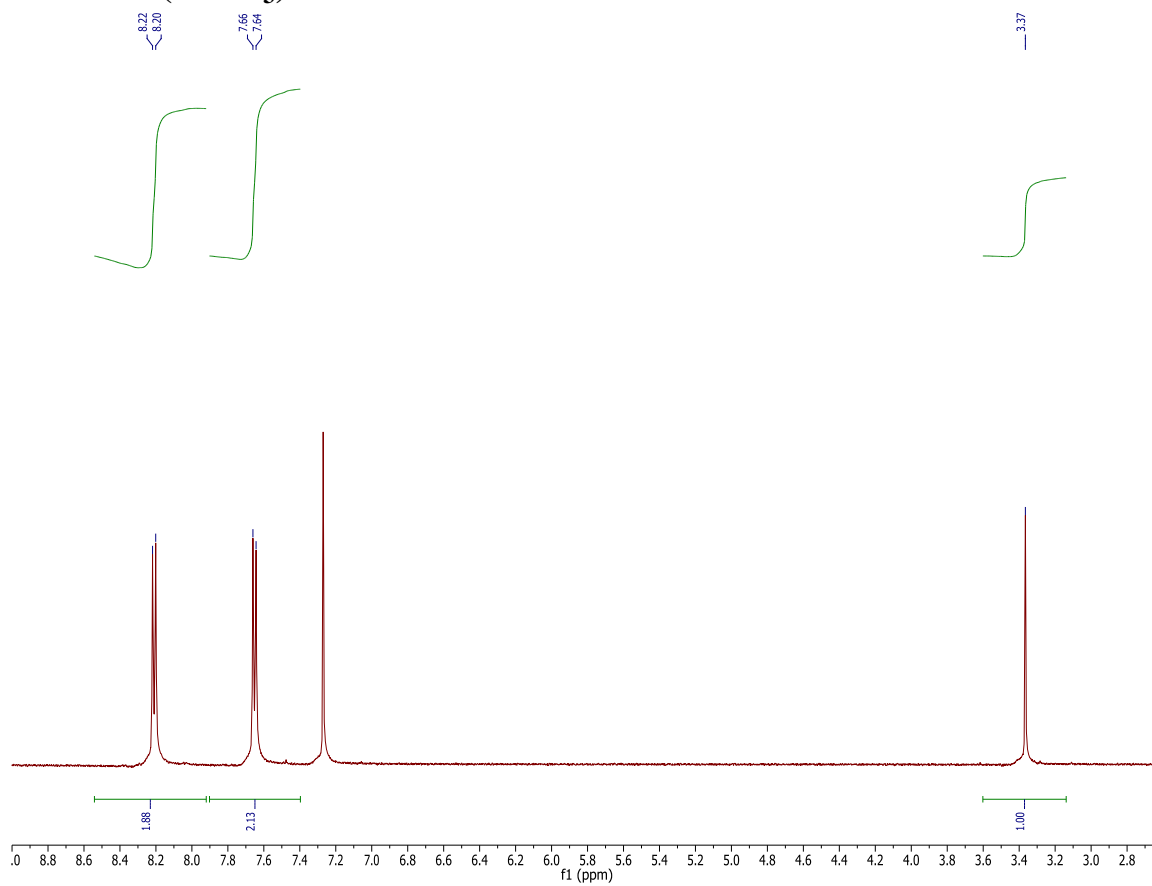
¹H NMR (CDCl₃)
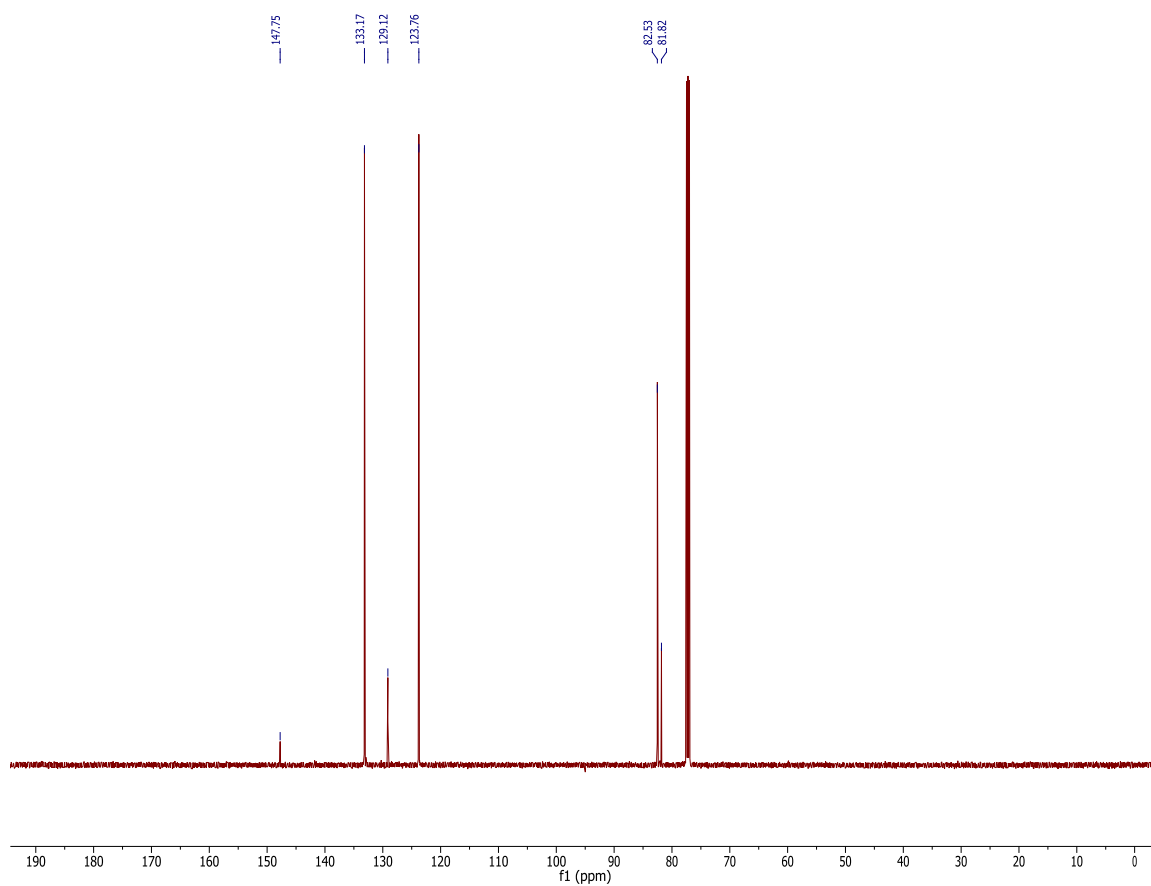
¹³C NMR (CDCl₃)
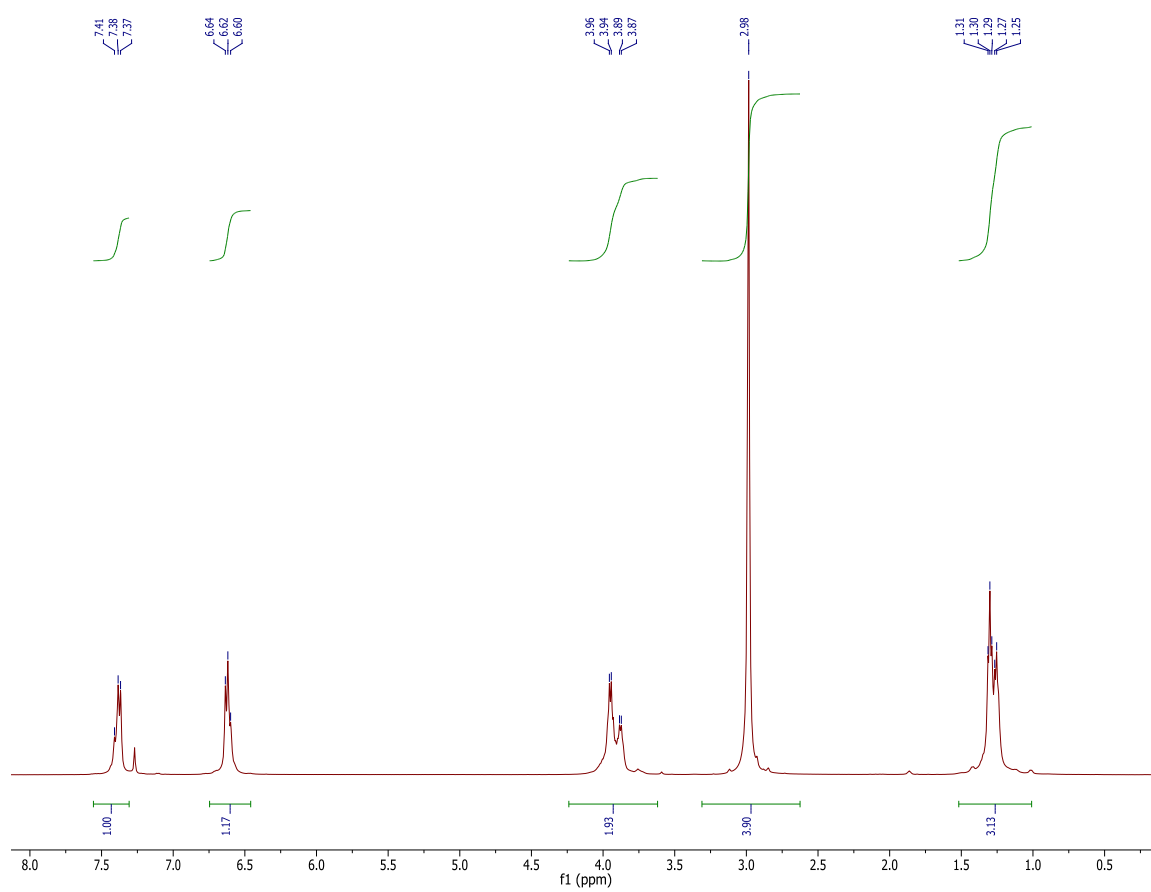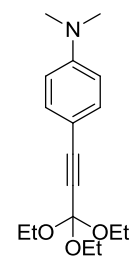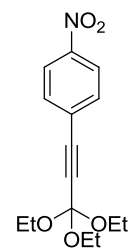
^{1}H NMR (THF-d$_8$)

¹H NMR (THF-d₈)

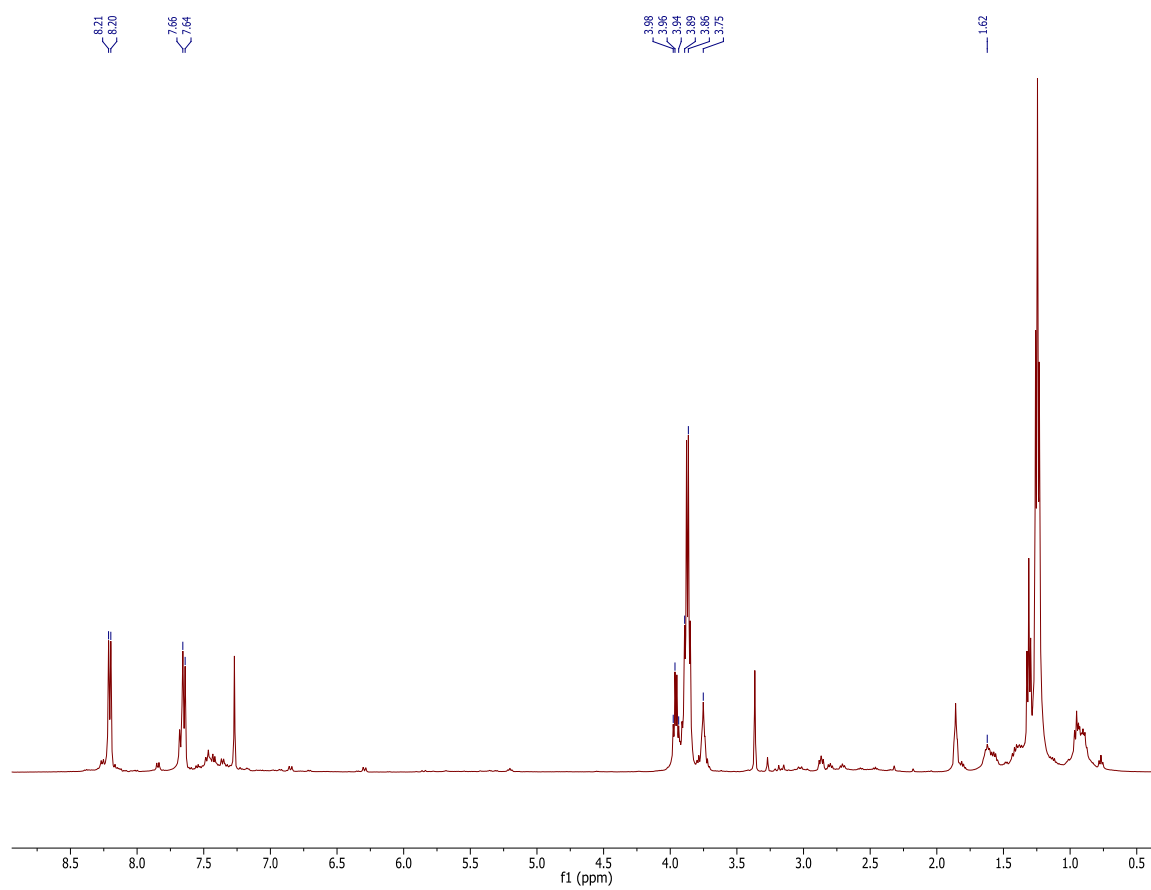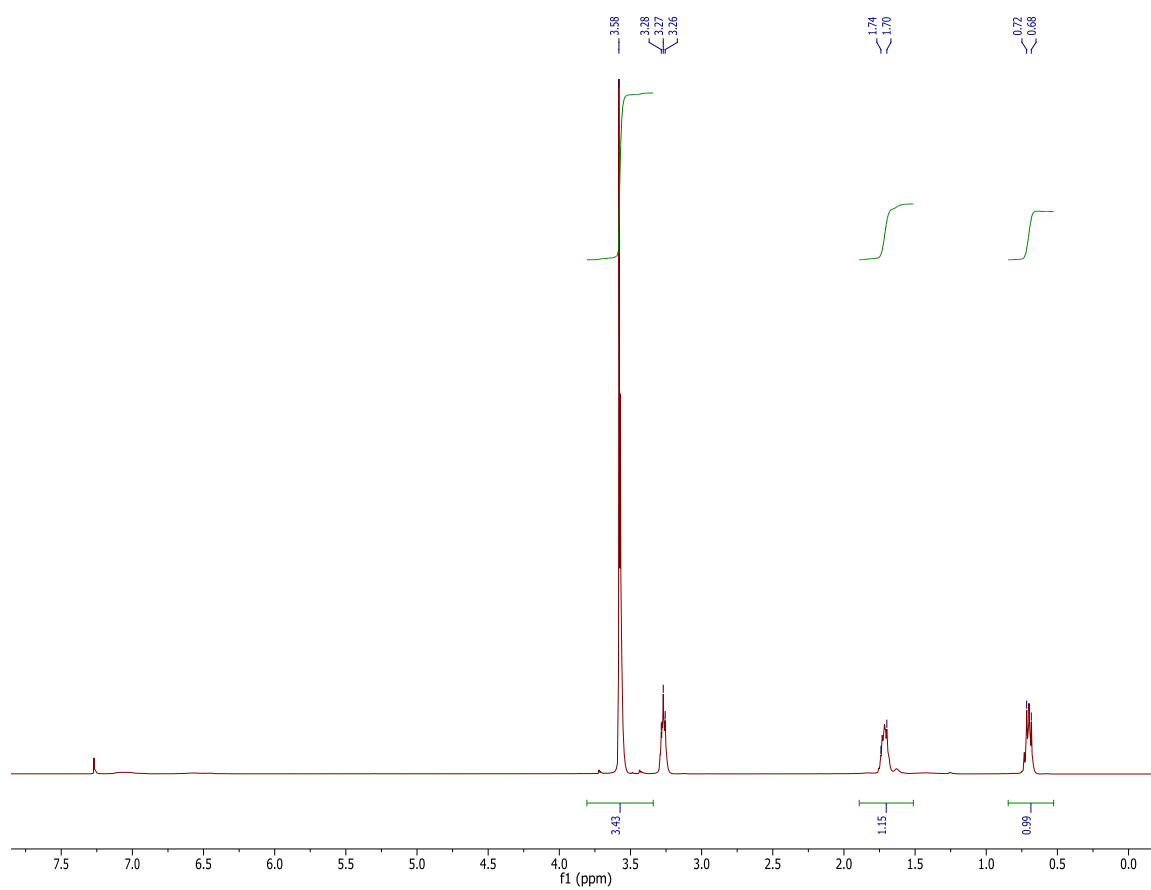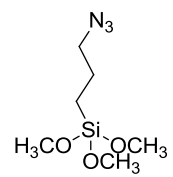**¹H NMR (CDCl3)**

December 2014

Curriculum Vitae   Yan Cao

Rutgers University   Kearny NJ 07032
73 Warren Street, Newark NJ   646-573-9135
yancao@pegasus.rutgers.edu   05/26/84

Education

Sept 2008 – Jan 2015 (anticipated)	Ph.D., Material/Surface Chemistry Rutgers University – Newark; Advisor: Elena Galoppini Thesis Title: Biofunctionalization of Semiconductor Materials for Sensing Device Applications
Sept 2003 – Jun 2007	B.S. Chemistry Lanzhou University; Lanzhou, P.R.China Thesis Title: Cutting Single-Walled Carbon Nanotubes with Acid Mixtures

Publications

1. Cao, Y.; Galoppini, E.; Reyes, I. P.; Duan, Z.; Lu, Y. *Morphology Effects on the Biofunctionalization of Nanostructured ZnO*. Langmuir **2012**, 28 (21), 7947-7951. DOI: 10.10211 /la3006037
2. Cao, Y.; Galoppini, E.; Reyes, I. P.; Duan, Z.; Lu, Y. *Functionalization of Nanostructured ZnO Films by Copper-Free Click reaction*. Langmuir **2013**, 29 (25), 7768-7775. DOI: 10.10211 /la4006949
3. Feng, W.; Rangan, S.; Cao, Y.; Galoppini, E.; Bartynski, R.; Garfunkel, E. *Energy level alignment of polythiophene/ZnO hybrid solar cells.* Journal of Materials Chemistry A **2014**, Accepted Manuscript. DOI: 10. 1039/C4TA00937A
4. Cao, Y.; Tang, H.; Galoppini, E. *Supramolecular Control of Chromophore Aggregation via CB[8]-Pyrene Binding on Nanostructured Metal Oxide Thin Films*. In Preparation
5. Cao, Y.; Chen, Y.; Rangan, S.; Galoppini, E.; Podzorov, V.; Bartynski, R. *Novel Stepwise Functionalization of Rubrene Single Crystal for Sensing Applications*. In Preparation
6. Tang, H.; Kopecky, A.; Cao, Y.; Johansson, P.G.; Meyer, G.; Galoppini, E. *Dye and Ligand Structural Effects on I2-Dye Interaction in Dye-Sensitized Solar Cells*. In Preparation

Contributed Presentations at Conferences

1. **Cao, Y.**; Galoppini, E.; Reyes, I. P.; Lu, Y. "*Morphology Effect of Functionalized ZnO Nanotips for Biosensors Application*" Twenty-Fifth Annual Symposium of the Laboratory for Surface Modification, New Brunswick, NJ, United States. March 2011.

2. **Cao, Y.**; Galoppini, E.; Reyes, I. P.; Lu, Y. "*Morphology Effect of Functionalized ZnO Nanotips for Biosensors Application*" Annual Chemistry Graduate Students Poster Session, Newark, NJ, United States. November 2011.
3. **Cao, Y.**; Galoppini, E.; Reyes, I. P.; Lu, Y. "*Morphology Effect of Functionalized ZnO Nanotips for Biosensors Application*" Bioanalytical Sensors Gordon Conference, Newport, Rhode Island, United States. June 2012.
4. **Cao, Y.**; Galoppini, E.; Reyes, I. P.; Lu, Y. "*Functionalization of Nanostructured ZnO Films by Cupper-free Click Reaction*" Twenty-Seventh Annual Symposium of the Laboratory for Surface Modification, New Brunswick, NJ, United States. March 2013.
5. **Cao, Y.**; Galoppini, E.; Reyes, I. P.; Lu, Y. "*Morphology Effect of Functionalized ZnO Nanotips for Biosensors Application*" Annual Chemistry Graduate Students Poster Session, Newark, NJ, United States. November 2012.
6. **Cao, Y.**; Galoppini, E.; Reyes, I. P.; Lu, Y. "Modification of Organic/Inorganic Semiconductor Surface through Chemical Reaction for Different Application" Chemical Reaction at Surfaces Gordon Conference, Les Diablerets, Switzerland. April 2013.
7. **Cao, Y.**; Galoppini, E.; Reyes, I. P.; Lu, Y. "*Biofunctionalization of Nanostructured Inorganic Surfaces through Chemical Reactions for Biosensing Application*" 23rd Winter I-APS Conference, Sarasota, Florida, United States. January 2014.

Awards

1. Graduate Student Excellent Award, May 2014
2. Dissertation/Excellent Fellowship, awarded by Rutgers University 2013-2014
3. I-APS Conference Travel Award, January 2014
4. GSGA (Graduate Student Government Association) Travel Award, 2011 and 2013
5. Third Order Award of the 15th experiment competition in the College of Chemistry and Chemical Engineering of Lanzhou University, June 2006
6. The Third-Class Excellent Academic Scholarship, awarded by Lanzhou University 2004-2005
7. The Third-Class Excellent Academic Scholarship, awarded by Lanzhou University 2005-2006

Teaching Experience

Graduate assistant, Rutgers University-Newark   *Sep.2012 – June2013*
Teaching assistant, Rutgers University-Newark
    Organic Chemistry Laboratory   *Sep.2011 – May 2012*
    World of Chemistry for Nursing Students   *Jan.2009 – May 2011*
    General Chemistry Laboratory   *Sep.2008 – Dec.2009*
    Grading and proctoring exams for General and Organic Chemistry   *Sep.2008 – May 2012*
Lab Supervision
    a. Instruction a high school student from SEED Program in the lab   *July 2011*
    b. Supervision of a first year graduate student   *Nov. 2012 - Present*